UC Santa Cruz

UC Santa Cruz Electronic Theses and Dissertations

Title

Advancing Adaptive Optics Technology: Laboratory Turbulence Simulation and Optimization of Laser Guide Stars

Permalink

https://escholarship.org/uc/item/0s8530f2

Author

Rampy, Rachel

Publication Date

2013

Peer reviewed|Thesis/dissertation

eScholarship.org Powered by the California Digital Library
University of California

UNIVERSITY OF CALIFORNIA
SANTA CRUZ

ADVANCING ADAPTIVE OPTICS TECHNOLOGY: LABORATORY TURBULENCE SIMULATION AND OPTIMIZATION OF LASER GUIDE STARS

A dissertation submitted in partial satisfaction
of the requirements for the degree of

DOCTOR OF PHILOSOPHY

in

PHYSICS

by

Rachel A. Rampy

March 2013

The Dissertation of Rachel A. Rampy
is approved:

_____
Professor Claire E. Max, Chair

_____
Professor Steven M. Ritz

_____
Donald T. Gavel, PhD

_____
Tyrus Miller
Vice Provost and Dean of Graduate Studies

Copyright © by

Rachel A. Rampy

2013

Table of Contents

List of Tables vi

List of Figures..... vii

Abstract..... xi

Acknowledgements xv

Chapter 1

Advancing Adaptive Optics Technology:

Laboratory Turbulence Simulation and Optimization of Laser Guide Stars

1.1 Introduction.....1

1.2 Adaptive Optics Technology 7

1.3 Simulating atmospheric turbulence.....9

1.4 Creating efficient laser guide stars.....12

Chapter 2

Manufacturing of Phase Plates for Simulating Atmospheric Turbulence

2.1 Introduction to laboratory turbulence simulation 15

2.2 History and methodology.....19

2.3 Analysis of materials and chromaticity.....22

2.4 Phase measurements with the Quadrature Polarization Interferometer .27

2.5 Results 33

2.6 Performance on the ViLLaGEs instrument at Mt. Hamilton and comparison to sky turbulence 39

2.7 Comparison to plates manufactured by other processes 44

2.8 Decomposition of phase into orthogonal polynomials 47

2.9 Discussion 51

Chapter 3

Laser Guide Star Adaptive Optics

3.1 History and motivation 54

3.2 The physics of sodium-light interactions 57

3.3 Optimization of pulse format 66

3.4 Spectral format options: Narrow line, multimode, or broadband? 73

3.5 Potential benefits of uplink correction 78

3.6 Discussion 82

Chapter 4

Modeling Current Laser Guide Stars at the Lick and Keck Observatories

4.1 Introduction 86

4.2 Simulation predictions overestimate return flux data from short pulse Laser Guide Stars 87

4.3 A more detailed model yielded equivalent results 97

4.4 Discussion 104

Chapter 5

Future Directions and Open Problems

5.1 Introduction 108

5.2 The future of phase plate manufacturing at the Laboratory for Adaptive Optics 110

5.3 Towards improved modeling and a better understanding of Laser Guide Stars 114

5.4 Can pulsed lasers produce brighter guide stars than CW? 120

5.5 Discussion 127

List of Tables

Table 2.1: A comparison of different clear aerosols 23

Table 2.2: The values of r_0, RMS, and Peak-to-Valley determine the strength of the turbulence on a given plate 39

Table 3.1: Comparison of the return flux from pulse lengths of 200 ns, 30 μs, and 60 μs, for 10% and 20% duty cycles 71

Table 3.2: Comparison of parameters between the current LGS, the laboratory tested format of the new fiber laser, and the goal format. 83

Table 3.3: The strength and direction of Earth's magnetic field at an altitude of 90 km for the locations of several large observatories 85

List of Figures

Figure 1.1: The basic components of a closed-loop astronomical AO system 8

Figure 2.1: A diagram of the spraying apparatus and spray pattern 21

Figure 2.2: Photographs of the spraying machine 21

Figure 2.3: Images from the Zygo interferometer show the presence of light scattering pigments in the enamel spray 24

Figure 2.4: Transmission spectra for the substrates and acrylic spray 25

Figure 2.5: A paper mask was used to isolate two regions for testing with visible and near-IR Zygo interferometers 26

Figure 2.6: The fringe images and reconstructed phase from visible and near-IR Zygo interferometers 26

Figure 2.7: The layout of the Quadrature Polarization Interferometer (QPI) 28

Figure 2.8: A visual illustration of interferograms from the two cameras being combined to produce a 2D phase map 30

Figure 2.9: Stability tests of QPI 32

Figure 2.10: Plate A 34

Figure 2.11: Plate B 35

Figure 2.12: Computer generated phases 36

Figure 2.13: Plate C 37

Figure 2.14: Plate D 38

Figure 2.15: The optical layout of the ViLLaGEs instrument 40

Figure 2.16: Power spectrum of the turbulence plate in ViLLaGEs 41

Figure 2.17: Example of shallow sky power spectrum 42

Figure 2.18: Example of bowed sky power spectrum 42

Figure 2.19: Example of Kolmogorov sky power spectrum 43

Figure 2.20: Power spectrum and structure function from measurements taken with the QPI on a lithographically etched glass plate 45

Figure 2.21: A mosaic of interferogram images and data taken with QPI of a near index matching plate fabricated by Lexitek 46

Figure 2.22: Mosaics of interferogram images from QPI for plates made at the LAO with hairspray and clear acrylic paint 47

Figure 2.23: Zernike decomposition of simulated phase maps 50

Figure 3.1: The atomic structure of sodium 57

Figure 3.2: Measurements of returned photons from the SOR Fasortronics laser as a function of wavelength, for circular and linear polarization 58

Figure 3.3: Emission patterns for sodium D_2 transitions 60

Figure 3.4: Predicted specific return in the mesosphere for CW 61

Figure 3.5: Predicted specific return in the mesosphere as a function of repump fraction 63

Figure 3.6: 100 μs simulations show time evolution of specific return flux for different levels of irradiance 68

Figure 3.7: Intermediate pulse format shows the presence of optical pumping between pulses 70

Figure 3.8: Diagram to demonstrate a Raleigh blanking scheme 72

Figure 3.9: Specific return in the mesosphere as a function of the light intensity for a single narrow line, a broadband spectrum with 500 MHz FWHM, and 3 narrow lines with 150 MHz spacing 75

Figure 3.10: Return from a LGS that is multimode as a function of mode separation and broadband as a function of bandwidth, for parallel and perpendicular to the magnetic field 76

Figure 3.11: Return as a function of r_0 79

Figure 3.12: Return flux from a top hat shaped irradiance profile compared to a Gaussian 81

Figure 4.1: LGSBloch predictions fit to data from the 50 W Fasortronics laser 89

Figure 4.2: The pulse shape of the dye laser on the Shane telescope 89

Figure 4.3: Data from the dye laser on the Shane telescope and the implied C_{Na} 90

Figure 4.4: Simulation of 5 cycles of the Keck II LGS 93

Figure 4.5: Predicted return flux for the Keck II LGS 94

Figure 4.6: Simulation of 100 cycles of the laser for the Keck I LGS 95

Figure 4.7: Predicted return flux for the Keck I LGS 96

Figure 4.8: Return flux in the mesosphere for the Shane dye laser 98

Figure 4.9: The target spectrum for modulation of the dye laser on the Shane telescope and a photograph of the measured spectrum 99

Figure 4.10: Approximate spectral function 100

Figure 4.11: Irradiance profiles for propagation through turbulence versus a Gaussian of comparable size 102

Figure 4.12: Average histogram of irradiance distributions versus a Gaussian 103

Figure 5.1: Peculiar phase, case 1 112

Figure 5.2: Peculiar phase, case 2 113

Figure 5.3: Changes in the return flux for different collision times 116

Figure 5.4: Launch telescope size changes the distribution of light in the mesosphere 118

Figure 5.5: Histograms of irradiance profiles for a 0.5 m diameter beam 120

Figure 5.6: 500 μs simulation showing initial enhancement in spontaneously emitted photons 121

Figure 5.7: Graph on pulsing at Larmor frequency by Paul Hillman 122

Figure 5.8: Evolution of irradiance levels in the mesosphere as a function of time when pulsing at Larmor frequency 123

Figure 5.9: Return flux in the mesosphere as a function of time for a pulse format with repetition rate equal to the Larmor frequency 124

Figure 5.10: Comparison of return flux at the top of the telescope for the Larmor pulse format and CW, with 10 W average power at Mt. Hamilton, and 20 W average power at Mauna Kea 125

Figure 5.10: Simulations of the Larmor frequency pulsing scheme for slightly different repetition rates 127

Abstract

Advancing Adaptive Optics Technology: Laboratory Turbulence Simulation and Optimization of Laser Guide Stars

by

Rachel A. Rampy

Since Galileo's first telescope some 400 years ago, astronomers have been building ever-larger instruments. Yet only within the last two decades has it become possible to realize the potential angular resolutions of large ground-based telescopes, by using adaptive optics (AO) technology to counter the blurring effects of Earth's atmosphere. And only within the past decade have the development of laser guide stars (LGS) extended AO capabilities to observe science targets nearly anywhere in the sky. Improving turbulence simulation strategies and LGS are the two main topics of my research.

In the first part of this thesis, I report on the development of a technique for manufacturing phase plates for simulating atmospheric turbulence in the laboratory. The process involves strategic application of clear acrylic paint onto a transparent substrate. Results of interferometric characterization of the plates are described and compared to Kolmogorov statistics. The range of r_0 (Fried's parameter) achieved

thus far is 0.2 – 1.2 mm at 650 nm measurement wavelength, with a Kolmogorov power law.

These plates proved valuable at the Laboratory for Adaptive Optics at University of California, Santa Cruz, where they have been used in the Multi-Conjugate Adaptive Optics testbed, during integration and testing of the Gemini Planet Imager, and as part of the calibration system of the on-sky AO testbed named ViLLaGEs (Visible Light Laser Guidestar Experiments). I present a comparison of measurements taken by ViLLaGEs of the power spectrum of a plate and the real sky turbulence. The plate is demonstrated to follow Kolmogorov theory well, while the sky power spectrum does so in a third of the data. This method of fabricating phase plates has been established as an effective and low-cost means of creating simulated turbulence. Due to the demand for such devices, they are now being distributed to other members of the AO community.

The second topic of this thesis pertains to understanding and optimizing the laser beacons used to bring AO correction to parts of the sky that lack a naturally bright light source for measuring atmospheric distortion. Long pulse length laser guide stars (LGS) that use fluorescence from the D_2 transition in mesospheric sodium are valuable both due to their high altitude, and because they permit Rayleigh blanking and fratricide avoidance in multiple LGS systems. Bloch equation simulations of sodium-light interactions in Mathematica show that certain spectral formats and pulse lengths (on the order of 30 μs), with high duty cycles (20–50%),

should be able to achieve photon returns within 10% of what is seen from continuous wave (CW) excitation.

Utilizing this recently developed code (called LGSBloch), I investigated the time dependent characteristics of sodium fluorescence. I then identified the optimal format for the new LGS that will be part of the upgrade to the AO system on the Shane 3 meter telescope at the Lick Observatory. I discuss these results, along with their general applicability to other LGS systems, and provide a brief description of the potential benefits of uplink correction.

Predictions from the LGSBloch simulation package are compared to data from currently operating LGS systems. For a CW LGS, the return flux measurements and theory show reasonable agreement, but for short pulse lasers, such as those at the Lick and Keck Observatories, the code seems to be overestimating the data by a factor of 2 – 3. Several tactics to explicate this discrepancy are explored, such as verifying parameters involved in the measurements and including greater detail in the modeling. Although these efforts were unsuccessful at removing the discrepancy, they illuminated other facets of the problem that deserve further consideration.

Use of the sophisticated LGSBloch model has allowed detailed study of the evolution of the energy level populations and other physical effects (e.g. Larmor precession, atomic recoil, and collisions). This has determined formats that will have maximal coupling efficiency of the laser light to the sodium atoms in order to achieve the highest possible return signal per Watt of output power. These quantitative findings allow the astronomical AO community to make rational, physics-based

choices of which high-power (and unavoidably high-cost) lasers to procure for implementation in future LGS systems.

Acknowledgements

Portions of this dissertation have been published previously in conference proceedings and journals. The majority of Chapter 2 appeared as R. Rampy, D. Gavel, D. Dillon, and S. Thomas, "New method of fabricating phase screens for simulated atmospheric turbulence," Proc. SPIE 7736, 77362Y (2010), and also R. Rampy, D. Gavel, D. Dillon, and S. Thomas, "Production of phase screens for simulated atmospheric turbulence," Applied Optics, Vol. 51, Issue 36, pp. 8769-8778 (2012). The majority of Chapter 3, and parts of Chapter 4, appeared as R. Rampy, D. Gavel, S. Rochester, and R. Holzlohner, "Investigations on long pulse sodium laser guide stars," Proc. SPIE 8447, 170 (2012).

This research was funded in part by The Association of Universities for Research in Astronomy through the Gemini Planet Imager program. Support for this work was also provided by the Bachmann Fellowship, made possible by a gift from Don and Sally Allen, and the University of California, Santa Cruz, Chancellor's Dissertation Year Fellowship.

Lick Observatory staff have made contributions to the research in this thesis. Particularly, Elinor Gates, Bryant Grigsby, Kostas Chloros, Brian Dupraw, David Hilyard, and Jim Ward. Also, Leslie Ward and Karen Peña of the CfAO have been extremely helpful on many fronts.

My success as a graduate student would not have been possible without the mentorship of Don Gavel and Claire Max. Many others have also provided invaluable professional and personal discussion, including Steve Ritz, Andrew

Norton, Katie Morzinski, Daren Dillon, Reni Kupke, Luke Johnson, Sandrine Thomas, and Mark Ammons. My comrades in the physics department have helped to make my time in Santa Cruz the best of my life, most notably Megan, Laura, Richard, Nicole, and Alice, but also many others. I've been blessed to have the support of other teachers, friends and family. Julie, thank you for all your wise words, and teaching me to watch, choose, and let go. Mark, thank you for reminding me to keep breathing. Eustacia, thank you for a long and wonderful friendship, and endless encouragement. Mary, getting to know you and your family has brought me incredible joy. Suzy, you've been a great sister and I couldn't imagine life without you. Mom and Dad, thank you for the early introduction to science and the wonders of nature. Lastly, a big thanks to Colleen Kron for her editorial skills in making this dissertation coherent and readable, and for providing friendship and support along the way.

Chapter 1

Advancing Adaptive Optics Technology:

Laboratory Turbulence Simulation and Optimization of Laser Guide Stars

1.1 Introduction

The human affinity for exploration has led to the development of instruments capable of extending our senses, thereby enabling us to gather detailed information about the processes taking place beyond the confines of our planet. The development of adaptive optics (AO) is revolutionizing the field of astronomy, as it has begun to permit astronomers to peer through Earth's turbulent atmosphere while maintaining diffraction limited imaging resolution.

Local temperature variations in Earth's atmosphere produce changes in the refractive index of air, resulting in wavefront distortion manifested as the blurring of images in optical systems and a loss of intensity in propagating laser beams. Because of this, astronomy has long been plagued by the limits of resolution that can be obtained with ground-based telescopes. One solution has been to place telescopes in space, but unfortunately these are expensive to deploy and maintain.

The concept behind AO was introduced to the scientific community in 1953, when the Mount Wilson and Palomar astronomer Horace W. Babock suggested: “If we had the means of continually measuring the deviation of rays from all parts of the mirror, and of amplifying and feeding back this information so as to correct locally the figure of the mirror in response to the schlieren pattern, we could expect to compensate both for the seeing and for any inherent imperfection of the optical figure” (Babcock 1953). The term "seeing" refers to a measure of the strength of atmospheric turbulence present at the observing location. Due to the complexity of such an endeavor, several decades passed before the US military began investing in AO development, and not until the early 1990s were systems first made available for use by the astronomical community (Beckers 1993). The strength of this emergent ability over previous turbulence countering techniques has led to important advances in our understanding of the universe, and the continued evolution of AO is crucial to future scientific breakthroughs.

AO technology has become increasingly intricate and is branching into many directions in order to address specific science questions. Its success has made it unthinkable to consider building a large ground-based telescope without including these capabilities. Many areas of astrophysical research are benefiting from the enhanced spatial resolution, including studies of the sun and other solar system objects, such as asteroids, planets and moons (Goode et al. 2010, Marchis et al. 2006b, de Pater et al. 2010). At greater distances, the combination of AO and high contrast imaging techniques are enabling investigations of planetary system formation

through direct imaging of circumstellar disks and extrasolar planets (Lagrange et al. 2010, Marois et al. 2008). In addition, extragalactic research is flourishing due to merging of AO with integral field spectroscopy, which allows estimates of masses of black holes in nearby galaxies, the study of active galactic nuclei (AGN) and mergers, and glimpses of the high redshift universe (Nowak et al. 2010, Genzel et al. 2011).

By overcoming several key technological challenges, the usefulness of AO can be extended further. The path to enabling a greater range of science can be summarized into three principal characteristics: (1) expanding sky coverage and corrected field of view, (2) high Strehl* near-infrared (IR) performance to produce a stable, high-contrast point spread function (PSF), and (3) correction at optical wavelengths to achieve increased angular resolution. The improvements to be expected by progress in each category will depend on the specific science case. Additionally, reducing thermal backgrounds and increasing AO system throughput as much as possible will lead to across the board performance enhancements.

Inclusion of laser guide stars (LGS) within the last decade has boosted scientific yield by vastly increasing sky coverage and allowing AO observations of targets at nearly any location in the sky. This ability has had a key role in expanding our understanding of the dynamics around our Galaxy's central black hole (Ghez et al. 2005), where would-be natural guide stars (NGS) are too heavily obscured by dust. To date, near-IR observations of stellar orbits near the black hole have achieved

* Strehl is a measure of the optical quality of an imaging system. It is defined as the ratio of the observed peak intensity from a point source to the theoretical maximum of a perfect system operating at the diffraction limit.

astrometric precisions of < 200 μas and radial velocity precision of 20 km/s. However, to begin to measure general relativistic effects (e.g. near the closest approach of the stars S0-2 and S0-102), an astrometric precision of < 100 μas is required (Weinberg et al. 2005). The future implementation of near-IR (rather than visible light) tip-tilt (TT) wavefront sensing on the Keck 1 telescope will improve the potential of reaching this goal. Beyond this upgrade, adding multiple LGS beacons to reduce the focal anisoplanatism (for better high-order correction over the field of view) will benefit this science case the most.

In just the last few years, over a thousand planetary systems have been discovered around other stars (Holman et al. 2012). A striking conclusion from these discoveries is that almost none of them resemble our own system, which leads to the question "why not?" While radial-velocity searches and NASA's Kepler transit search have been prolific sources for identifying new solar systems, AO at the diffraction-limit of large telescopes provides one of the only ways of characterizing these planets in their own light. Direct imaging with AO can also be used to detect and characterize debris disks in young systems. Beyond understanding planetary system formation, a main goal of such studies is to find planets with oxygen and liquid water. A potentially habitable planet will be most readily identified around a low-mass star cooler than the Sun, because this type of star is less likely to swamp the planet's light with its own. Such a discovery will require precise knowledge of the instrument PSF, and a LGS with near-IR TT sensing (cool dwarf stars are too faint at visible wavelengths) to satisfy the contrast requirements.

To date, most major AO accomplishments have been made at observing wavelengths in the infrared (IR) range. However, future science goals will become achievable when AO capabilities exist at visible wavelengths. For example, these shorter wavelengths have the promise of being able to deliver the spatial resolution required to resolve stellar populations in nearby galaxies, circumnuclear starbursting in AGN, and faint hosts around bright quasi-stellar objects (QSOs, a type of quasar) at redshifts beyond 1. This will be helpful for testing predictions of AGN development (Ammons et al. 2009), and understanding the formation and subsequent evolution of structure in our universe. For such distances ($z > 1$), galaxies have shrunk to angular sizes of approximately 1 arcsecond, making non-AO based observations almost useless at uncovering morphologies and internal kinematics, due to the size of the atmospheric seeing halo relative to the size of the typical source.

At the epoch of greatest star formation and AGN activity (around $z \sim 2.5$), traditional optical lines of Hα, OIII and OII are nicely shifted into the K, H and J bands, respectively. LGS AO observations at the Keck Observatory with OSIRIS (an integral field spectrograph on Keck 1) have only recently began using spatially resolved IR spectroscopy to dissect some of the brightest galaxies at this epoch (Melbourne et al. 2011). But with increased sensitivity and improved signal-to-noise, a wealth of science topics can be addressed. These include the relationship between AGN and their host galaxies: radio galaxies and quasars have very strong emission lines and complex kinematics. In more "normal" galaxies, the redshift range from 1.5 to 2.5 is a key era for the birth of their first stars and the formation of the major

architectural components of the galaxy, namely the bulge and disk. Measuring the morphology of star formation, the kinematics of proto-disks, the internal velocity dispersions and metallicity gradients (e.g. from the NII/Hα ratio), will allow us to witness the birth of galaxies like the Milky Way.

The attainment of imaging and spectroscopy at the diffraction limit becomes increasingly problematic as the science wavelength grows shorter, because increased accuracy and higher temporal bandwidths are required for AO correction. Brighter guide stars are needed, and for reasonable sky coverage they must be artificial stars (provided by lasers). Unless breakthroughs are made in wavefront sensing efficiency, the required laser power quickly becomes very expensive or simply unobtainable for many pertinent science cases. As more types of lasers become available, and as their cost remains a substantial investment for observatories, identifying the methods to optimize their performance is a crucial endeavor.

In this thesis, I present research on two areas where AO technology has been in need of more versatile tools and greater depth of understanding. The first project developed a method to create turbulence simulation plates for testing and calibrating AO systems that is simple, low cost, and capable of producing a large range of turbulence strengths. The second component involves numerical investigations into sodium-light interactions to optimize LGS brightness, including comparisons with data from current systems, predicted returns for a new laser, and a discussion of the ideal format for use in future systems.

The next section provides a brief overview of how AO functions and its uses, followed by two sections dedicated to introducing my specific areas of research, describing what was accomplished, and outlining the remainder of this thesis.

1.2 Adaptive Optics Technology

AO systems require three main components: (1) a wavefront sensor (WFS) to detect the distortions in the incoming light, (2) a computer to receive and process this input, and (3) a deformable mirror (DM), which is controlled by the computer, to correct the distortions. Figure 1.1 shows a simplified schematic of a closed-loop AO system for astronomical telescopes. Closed-loop refers to the architecture where wavefront measurements are taken after the light has reflected off the DM, as opposed to open-loop where the aberrated light is sensed directly. The system must update the mirror's shape at least several hundred times per second to keep up with the changing atmosphere (Hardy 1998).

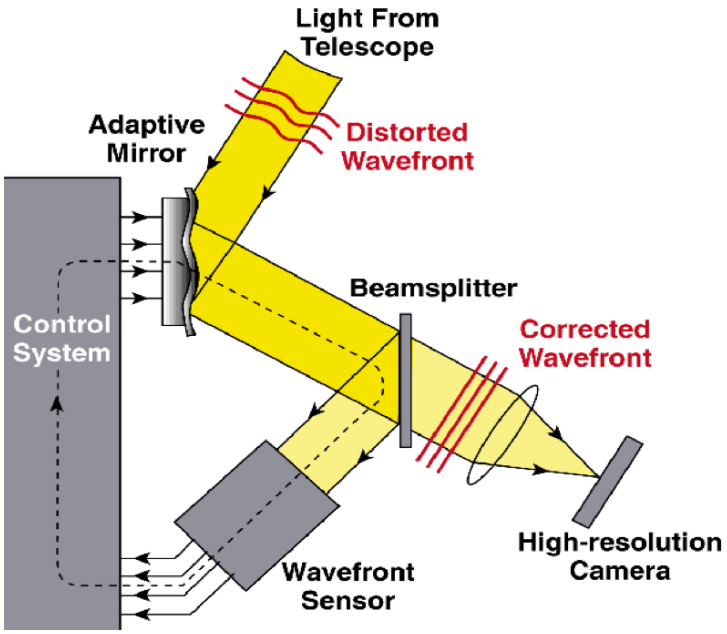

Figure 1.1: This diagram shows the basic components of a closed-loop astronomical AO system. Figure courtesy Claire E. Max, Center for Adaptive Optics, University of California–Santa Cruz.

The necessity of a bright reference beacon for measuring the distortion of the incoming light imposes a significant limitation on the use of AO. In astronomy, the requirement is to have a guide star within a few arcseconds of the science target that is ~15th magnitude or brighter. However, on average only ~10% of the night sky contains such a source. Sky coverage is particularly low at high galactic latitudes, hindering extragalactic research from using AO efficiently. To mitigate this problem, high-power lasers can be used to create artificial guide stars in Earth's upper atmosphere, a technique that is beginning to extend AO capabilities to all locations in the sky. These lasers are tuned to a wavelength of 589 nanometers (nm), in order to energize the layer of sodium atoms that are naturally present in the mesosphere at an altitude of about 90 kilometers (km). These sodium atoms then re-emit the laser light

in a process called fluorescence, producing a glowing artificial star. This same atomic transition is used to create the yellow/orange streetlights present in many cities. LGS AO is currently a young field, with much effort still invested in technology development. However, it has already produced substantial results and is the basis for ~180 refereed science publications thus far.

AO technology has also been successfully applied to other, non-astrophysical, applications of high-resolution imaging. For looking into the living human eye, it is used in conjunction with scanning laser ophthalmoscopy and optical coherence tomography, and has produced the first images of retinal microvasculature and associated blood flow, retinal pigment epithelium cells, and single cone photoreceptors (Zhang et al. 2006). Other types of biological imaging have also benefited from AO (Azucena et al. 2010). Additionally, it has proven useful in the stabilization of the position and direction of laser beams between modules in free space optical communication systems, for mountaintop-to-mountaintop (Biswas et al. 2001) and ground-to-space (Wilson et al. 2007) information exchange.

1.3 Simulating atmospheric turbulence in the laboratory

The ability to simulate representative wavefront distortion in the laboratory is a crucial part of testing and developing AO technology. Astronomical systems designed to compensate for atmospheric turbulence need their capabilities proven and understood before being installed on a telescope. A number of solutions have been proposed and utilized (discussed in Chapter 2), but a simple, accurate, and inexpensive device has been lacking.

During my first two years of graduate research, I developed a technique for creating transmissive phase plates as a solution to turbulence simulation needs. The approach has its origins in an earlier technique that used hairspray on glass plates (Thomas 2004). The current method involves the application of clear acrylic paint onto a transparent substrate. This technique provides plates that are more stable over time and gives better control over turbulence statistical properties. In the process of development, I designed (in collaboration with Daren Dillon) a machine to automate the fabrication process. This invention has been disclosed through UC's Intellectual Property (IP) office, and a design patent has been requested.

Interferometric characterization of the plates show that their properties can be made to agree quite well with those of real atmospheric turbulence, as it is currently understood according to Kolmogorov statistics (Kolmogorov 1941). A large range of turbulence strengths, characterized by the Fried's parameter r_0 (Fried 1965), has been demonstrated. The physical size of r_0 imprinted on the plates varies between 0.2 – 1.2 mm, with a Kolmogorov spatial frequency power law. These phase plates have been used in the Multi-Conjugate Adaptive Optics testbed in the Lick Observatory Laboratory for Adaptive Optics (Ammons et al. 2009), in the prototype AO system called the Visible Light Laser Guidestar Experiments (ViLLaGEs, Grigsby et al. 2008), and in the Gemini Planet Imager telescope simulator (Macintosh et al. 2008).

To validate the plates and gain understanding of real atmospheric turbulence, I collected open-loop WFS data from on sky ViLLaGEs runs, taken with starlight through the real atmosphere, and compared these to data with the AO system fed with

a point-source fiber through a rotating phase plate. These were then both analyzed against what would be expected according to Kolmogorov theory. In general, the two (on-sky vs. turbulence simulation plate) had very similar characteristics, and good agreement was found between the statistics of the plate measured by ViLLaGEs and what was determined for it using the equipment in the laboratory. However, the power spectra of the sky data only closely followed a Kolmogorov power law spectrum about one third of the time. This showed that while we can create nearly "perfect" Kolmogorov phase plates, the real sky atmosphere is not always so theoretically pristine. As is discussed later on, we attribute this to other factors faced at observatory sites, such as dome seeing and upper altitude (e.g. Jetstream) turbulence occurring on much different spatial-temporal scales.

There is a definite need for this technology in the greater AO community for the development and calibration of AO instruments. We have provided a means of distributing these devices at low cost to collaborators outside the University, via a mechanism set up by the University of California's Intellectual Property office. Lick Observatory optics shop technical staff have been trained in the plate manufacturing techniques to ensure this technology will continue to be available in the future.

A detailed description of the plate fabrication method and characterization techniques is provided in Chapter 2. The analysis of ViLLaGEs data is also presented there. Planned future developments of this project are discussed in the first part of Chapter 5, along with currently outstanding questions and issues.

1.4 Creating efficient laser guide stars

Artificial guide star beacons created with lasers have enabled astronomers to lock AO systems on to any field in the sky, greatly expanding "sky coverage" over those systems that require nearby bright natural stars, and thereby extending the impact of AO on astronomical science. Large telescopes require a high altitude beacon for adequate atmospheric probing and therefore most large observatories have converged on using a guide star generated in the mesosphere at ~90 km altitude. These systems require a particular wavelength laser that is resonant with atomic Sodium's D_2 transition (λ=589 nm), at fairly high average power levels, of 10-20 Watts (W). These lasers are very expensive, both because the wavelength is difficult to produce using current technology and because there is no particular commercial driver. Thus there is considerable payoff in maximizing coupling efficiency to the sodium atoms, in order to achieve the highest possible return signal per Watt of laser output power.

For years people have taken a pragmatic view on creating bright sodium beacons, with the focus being achieving high average output power, because the available laser formats were few and far between. More recently, the importance of format has become clear as continuous wave (CW) lasers have shown 10 times higher photon return per Watt launched power than short pulse systems (Denman et al. 2006). As new types of lasers at the wavelength of 589 nm appear on the scene, choosing among them is a high-stakes (meaning high-cost) issue for large observatories. Computer simulations of sodium-light interactions are providing

quantitative and unique insights into the atomic physics processes taking place in response to a wide variety of laser formats, and will allow the astronomical AO community to make rational, physics-based choices of which lasers to procure for their LGS systems.

I used numerical models based on atomic density matrix calculations to understand the way in which laser light interacts with atomic sodium at the low densities present in the upper atmosphere. A brief history of LGS technology, along with details of these simulations and how they differ from previous work in this area, are presented in Chapter 3. The software package used is available for free download at http://budker.berkeley.edu/ADM/.

The Laboratory for Adaptive Optics (LAO) has the opportunity to work with a prototype guide star fiber laser built by Lawrence Livermore National Laboratory (LLNL). This system provides a moderately tunable wavelength near the sodium D_2 line, either in continuous wave (CW) mode or programmable in various pulse and spectral formats. Plans are to eventually install this laser on the Shane Telescope at Mt. Hamilton as part of an upgraded AO system. Guided by the results of studies presented in this thesis, LAO researchers will endeavor to adjust the pulse and spectral format for optimal coupling to and signal return from the mesospheric sodium atoms. The suggested ideal format and predicted return flux are given at the end of Chapter 3, along with some discussion of the potential benefits of uplink correcting the LGS.

Chapter 4 discusses the work of myself and others to validate the modeling code by ensuring that the results predicted by the model are consistent with experimental measurements from current LGS systems. Holzlohner et al. (2010) demonstrated that the code is capable of reproducing the measured return from the CW 50 Watt Fasortronics laser at the Starfire Optical Range (SOR) with acceptable (but higher than average) values for poorly constrained parameters, such as the mesospheric sodium abundance. I verified these findings, and then went on to model the short pulse laser systems at the Lick and Keck Observatories. I identified a discrepancy, in that the simulations overestimated the measured return flux at the top of the telescope by a factor of 2 – 3. Holzlohner et al. (2012) found the same degree of inconsistency when modeling the short pulse LGS on the Gemini Multi-Conjugate Adaptive Optics System (GeMS). Efforts to determine the cause of the problem have thus far focused on incorporating a greater level of detail in the modeling, which has only reduced the disagreement by a small amount.

The second half of Chapter 5 addresses other possibilities that should be investigated to improve the agreement between theory and experiment for LGS. Future experiments capable of shedding light on the current unknowns are also suggested, along with some discussion of a recently proposed idea that may be able to further enhance guide star brightness.

Chapter 2

Manufacturing of Phase Plates for Simulating Atmospheric Turbulence

2.1 Introduction to laboratory turbulence simulation

Adaptive Optics (AO) was established to compensate for the blurring effects of turbulent air in Earth's atmosphere on astronomical images. Hence, understanding the effects of turbulence on the propagation of electromagnetic fields and how they manifest in imaging systems is critical. Research into the properties of turbulent media and energy exchange in the atmosphere led to the development of Kolmogorov (Kolmogorov 1941) and frozen flow theories (Taylor 1938). Respectively, these theories enable a means of assessing spatial-temporal properties of the phenomenon, and allow reasonable modeling using plates with stationary phase aberrations that can be rotated or translated to replicate wind velocity.

The Fried parameter (Fried 1965), or coherence length, $r_0(\lambda)$, is a useful metric for characterizing the strength of a turbulent medium to affect the propagation of light waves with a given wavelength, λ, through it. The Fried parameter corresponds to the diameter of an aperture over which the RMS wavefront aberration due to the turbulence is less than 1 radian. The spatial power spectrum for Kolmogorov turbulence, given in radians of phase (at λ) squared per inverse meter

(i.e. spatial frequency, cycles per meter) can be written in terms of r_0 (given in meters) as

$$P(k) = 0.027 r_0^{-5/3} k^{-11/3}, \tag{2.1}$$

where k represents spatial frequency (units of inverse meters). The strict power law is valid between two spatial scales, called the inner and outer scale, at which the energy transfer assumptions and homogeneity assumptions, respectively, of Kolmogorov break down. The spectral analysis of real phase measurements is done approximately by squaring the Fourier Transform of the phase map and taking a radial average (i.e. the average of all points at a given distance from the center of the distribution) of the resulting two-dimensional power spectrum.

Phase fluctuations can also by described by the structure function D_Φ, defined as the expected value of the square of phase difference, in radians, between two points at separation r. That is

$$D_\Phi(r) = < [\Phi(x) - \Phi(x+r)]^2 >, \tag{2.2}$$

where $\Phi(x)$ is the value of the phase at location x, and $\Phi(x+r)$ is the value of the phase at a distance r from location x, and $< \cdots >$ indicates the statistical expected value. Formally, the phase structure function is the inverse Fourier Transform of the phase power spectrum (Noll 1976). For Kolmogorov turbulence specifically, the structure function takes the form

$$D_\Phi(r) = 6.88 \left(\frac{r}{r_0}\right)^{5/3}. \tag{2.3}$$

When plotted on log-log scales the graphs of the power versus frequency are expected to be linear, with a slope of -11/3, and the structure function versus separation r to have a 5/3 slope, for turbulence that follows Kolmogorov theory. Fitting phase measurement data to these functions provide two methods for determining r_0.

For testing and calibrating a complex adaptive optics (AO) system, it is useful to have an artificial turbulence generator with known, realistic, and repeatable characteristics. Many current schemes for creating representative atmospheric aberrations are costly and place cumbersome requirements on the optical system. One key technical challenge is producing turbulence with r_0 values as small as a few hundred micrometers at visible wavelengths. In a telescope simulation system, a larger r_0 requires a correspondingly large pupil diameter, and larger relay optics, to match the ratio of primary mirror diameter to the typical value of r_0 for the telescope and location being modeled. Several methods of generating turbulence that have been investigated and reported in the literature include near index matching (Rhoadarmer et al. 2001), hot air chambers (Keskin et al. 2006), liquid filled chambers (Davis et al. 1998), spatial light modulators (Phillips et al. 2005), ion-exchange phase screens (Butler et al. 2004), and surface etching (Hippler et al. 2006).

In this chapter, I present a method of creating turbulent phase plates that was developed in the Laboratory for Adaptive Optics (LAO) at the University of California, Santa Cruz. The manufacturing of these plates involves the strategic

application of clear acrylic paint onto a transparent substrate, such as glass or plastic. This process is capable of producing plates with values of r_0 in the range 300 – 800 μm, measured at a wavelength of 650 nm (or equivalently, about 225 – 605 μm measured at a wavelength of 500 nm), and has proven to be useful for injecting turbulence into optical systems operating at both infrared (IR) and visible wavelengths. As part of the validation process, measurements of a plate were compared to real atmospheric turbulence data taken by the same instrument (ViLLaGEs). It was observed that the plate follows Kolmogorov theory closely, based on temporal power spectra, but the sky only does so approximately a third of the time.

The following section contains an outline of this technique and how it was developed, followed by a description the properties of the materials used and analysis of chromaticity of the resulting plates in Section 2.3. Section 2.4 discusses the instrument used to characterize the plates at the LAO. Section 2.5 presents results from this instrument for plates with varying turbulence strengths, and a comparison with computer generated Kolmogorov phases. The outcome of incorporating these plates in an on-sky AO testbed is presented in section 2.6, with a comparison to real atmospheric turbulence measured with the same instrument, and an analysis of how often the sky follows Kolmogorov statistics. Section 2.7 gives a comparison to phase plates made by other processes, and Section 2.8 investigates decomposition of phase measurements into orthogonal polynomials. The overall effectiveness of this method

is discussed in Section 2.9, including issues of repeatability and the range of achievable parameters.

2.2 History and methodology

The current technique is a derivative of the work of Thomas (2004). The initial method involved spraying hairspray onto glass plates, where variations in the thickness of the applied material create optical path differences similar to that of the atmosphere. During investigations of this method at the LAO, it was soon apparent that a non water-soluble spray would be preferable, to avoid absorbing moisture from the environment and collecting dust. Experimentation began with Krylon® clear acrylic paint. After I fabricated several phase plates by hand, Daren Dillon and I designed an automated system to help with controlling variables involved in the technique.

This automated method involves moving the spray can on an x-y stage over the plate, using two Velmex Inc. slides mounted upside-down. Attached to the lower slide is a harness that holds the aerosol can and a solenoid to turn it on and off. The assembly is enclosed in a plexiglass box with a ventilation system, consisting of two air filters and a fan, to help circulate air and remove particulates and paint fumes. The entire setup is housed in a fume hood for further elimination of hazardous paint fumes from the work environment. Figure 2.1 contains a diagram of the apparatus, and Figure 2.2 shows photos of the interior and exterior.

Layers of paint are applied to a stationary plate in a raster scan pattern, as shown on the right in Figure 2.1. The machine allows precise control of variables

such as how quickly the can moves, the distance between back and forth passes, and how far the can is above the plate. These first two parameters are necessary for depositing a thickness of paint that will not contain bubbles after drying (this often happens when the paint is applied too thickly) and achieving uniform coverage (without ridges or gaps). The distance between plate and can change the resulting r_0, but not linearly. Because other parameters can be varied more reliably to do this we generally leave the plate at a fixed height of about 14 cm below the can. Our main method of varying the statistics is through the number of layers and the amount of time elapsed between applications. For the current setup, a single layer results in a plate with r_0 about 0.5-0.6 mm. If a second layer is added less than 2 hours after the first application, this r_0 can be increased. Re-spraying after 24 hours will result in a smaller r_0. The level of airflow around the plate while the paint is drying has also shown to impact the final product. Too much wind, such as from leaving the fan on in the box, can result in bubbles being trapped in the paint or the formation of directional high order structure.

By taking advantage of the full dynamic range of the linear motors, we have successfully used this machine to produce phase plates with diameters up to 20 cm. The standard size substrates we offer are 7.6 cm (3 inch) and 14 cm (5.5 inch) diameter disks.

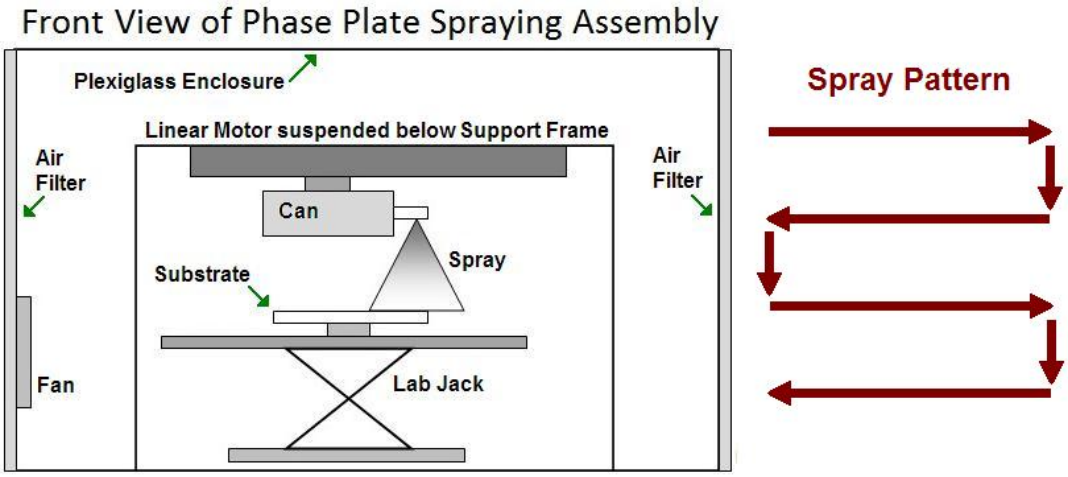

Figure 2.1: A diagram of the spraying apparatus is shown on the left, and the arrows on the right indicate the path followed by the can while coating the substrate.

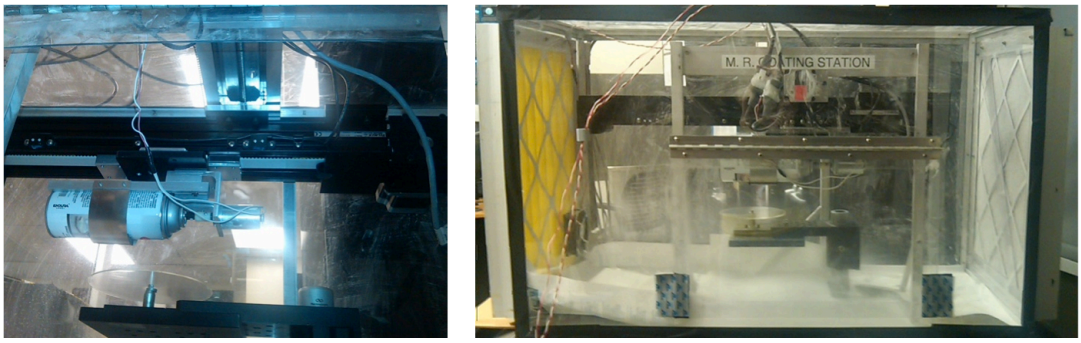

Figure 2.2: The left photograph shows the aerosol can suspended from the two motorized slides. The plate being sprayed is also visible beneath the can, near the bottom left. On the right is the entire setup, as viewed from outside the plexiglass enclosure.

In most AO testing applications using phase plates, the intention is to model the effects of dynamic turbulence, i.e. wind. This can be achieved by translating a rectangular plate through the test beam path, or by rotating a circular disk for continuous turbulence. It is important to note that rotation produces an artificial twist of the phase flowing by the aperture, but this is not an issue for many applications. For a lightweight and durable disk we chose to use 3 mm thick, λ/10 optical quality, plastic plates manufactured by Edmund Optics. These substrates are made of Thermoset ADC (CR-39®), where the thermosetting process generates very little

birefringence; the plastic has an Abbe Value of 59, which is close to that of glass (which is 60) and has an index of refraction equal to 1.5[†]. Acrylic, used in the spray, has a refractive index of 1.49 at 588 nm and an Abbe number of 55.3. These characteristics enable the phase plates, while not perfectly achromatic, to have properties close to that of a clear glass such as BK7. This material is also receptive to the process of laser cutting, which allows the flexibility to create turbulence plates whose dimensions have been tailored to meet the specific needs of the user.

2.3 Analysis of materials and chromaticity

This section presents the process used in selecting optimal materials for this type of turbulence plate, and describes how the chromaticity of the resulting plates was assessed. There are several varieties of transparent spray paint, so it was necessary to investigate the potential of different types for this application. The chromatic transmission of acrylic paint and the plastic and glass substrates is examined. The section concludes with an investigation of the chromaticity of phase aberrations on the finished product, using Zygo interferometers operating at IR and visible wavelengths.

Seven different kinds of clear spray paints were investigated. Table 2.1 lists the type and brand of spray, the amount of scintillation (i.e. intensity variation) it produced on a heavily coated glass plate, in addition to various other pros and cons associated with each type. Intensity variations were measured by a relay consisting of

[†] PPG Industries, www.ppg.com/optical/opticalproducts/opticalmaterials/Pages/CR-39.aspx

two lenses and a Basler CCD camera. The plate scale with this arrangement was 162 pixels per millimeter. The scintillation with nothing in the system was 2%, and the uncoated plastic and glass substrates were both found to have 5% variation in intensity.

Type of Spray	% Intensity Variation	Pros	Cons
Krylon Acrylic	9	Completely transparent	Low viscosity, difficult too apply an even coating
Krylon Acrylic UV	11		
8321 Lacquer	14	None	Yellow tint
Minwax Lacquer	10		
Ace Polyeurothane	8	None	Yellow tint
Krylon Polyeurothane	10		
Ace Enamel	48	Higher viscosity, easy to apply an even coating	Contains pigment which causes large intensity variations

Table 2.1: A comparison of different aerosols showed the Krylon brand Acrylic spray to be the optimal choice because it is completely transparent, and does not cause significant intensity variations.

The lacquer and polyeurothane had similar viscosity to the acrylic sprays, but showed a slight yellow tint after several layers were applied. The enamel spray was very easy to work with because of its higher viscosity. However, multiple layers showed a slight increase in opacity. The scintillation measurements, and images taken with a Zygo interferometer, confirmed the presence of light scattering pigments in the spray. Figure 2.3 shows these results from the Zygo, where the left image is of an uncoated plastic disk and the right is a disk heavily coated with the enamel. Each image covers 3 mm by 1.5 mm of the plate. The irregularities visible in the right image indicate the presence of light scattering particles. The RMS wavefront deviation caused by an uncoated plate was measured and found to be a negligible background.

The acrylic is the optimal choice since it is completely transparent, even after the application of several thick layers, and induces only about 10% scintillation, which is less than seen in the normal atmosphere (Hardy 1998).

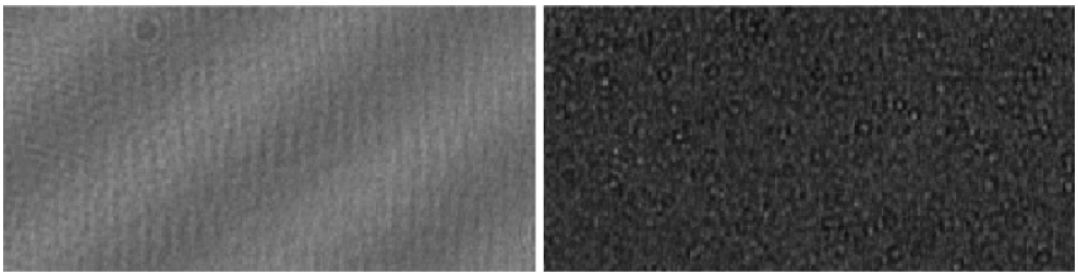

Figure 2.3: Images from the Zygo interferometer show the presence of light scattering pigments in the enamel spray. The left image is an uncoated plastic disk, and on the right is a disk coated with the Ace enamel, at the same magnification. The "ripples" seen on the uncoated disk are interference patterns due to the disk surface not being perfectly perpendicular to the beam.

The transmission of the substrates and acrylic spray were measured between 200 and 2000 nm, as shown in Figure 2.4. The plastic has a significant decrease in transmission around certain near infrared wavelengths. It is not expected that this will interfere with overall functionality on a testbed or as a simulator in an on-sky AO system, since the light source intensity can generally be adjusted in these situations and testing is usually done at wavelengths shorter than 1600 nm. Although the absorption features in the plastic indicate chromatic behavior this will only change the piston of the phase because it is a flat surface with uniform thickness. The acrylic, where the turbulence is imprinted, does not show any significant absorption features and thus is expected to have little chromaticity.

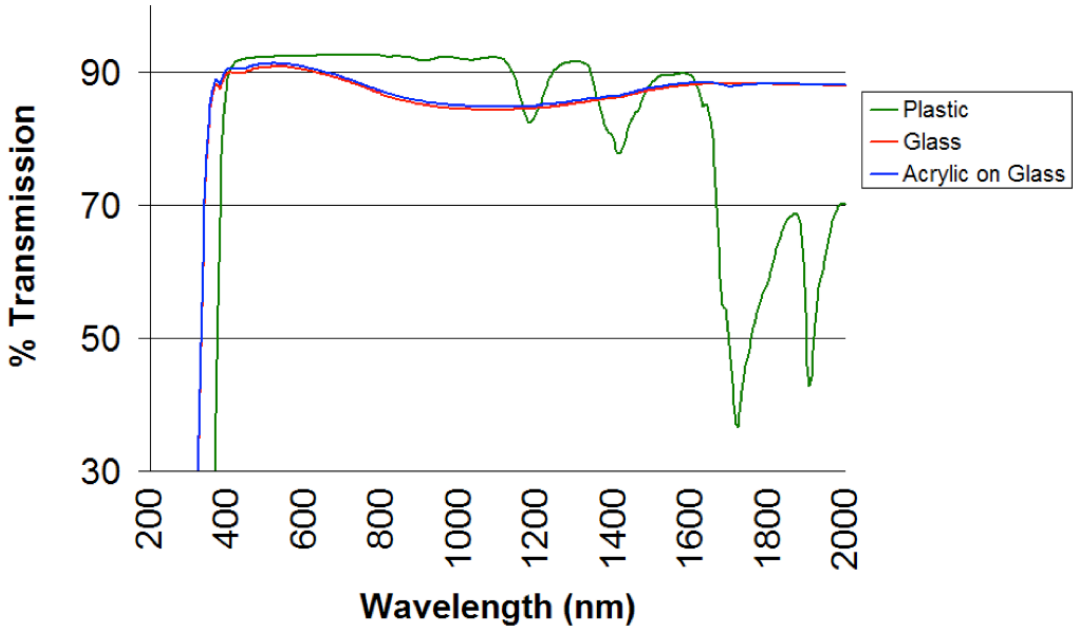

Figure 2.4: Transmission spectra for the two substrates, plastic (green) and glass (red), and for the acrylic spray on glass (blue). The presence of the spray on glass causes no significant decrease in transmission, and the slight increase (blue line is slightly above the red) is likely due to lensing by the uneven surface of the acrylic.

To quantify the chromaticity in the acrylic on plastic plates, images were taken with Zygo interferometers operating at visible (633 nm) and near-IR (1550 nm) wavelengths. This analysis was conducted courtesy of Kent Wallace and his team at the Jet Propulsion Laboratory (JPL) in Pasadena, California. On the plate tested, two regions were defined with a paper mask, as shown in Figure 2.5. Three measurements were taken of each region at both wavelengths. Figure 2.6 shows fringe patterns and reconstructed phases of the two areas, with the phase maps looking practically identical in the visible and IR. The average of measurements of Peak-to-Valley of the reconstructed phases show a 7% difference between the two wavelengths, but the average RMS values are less than 0.2% different.

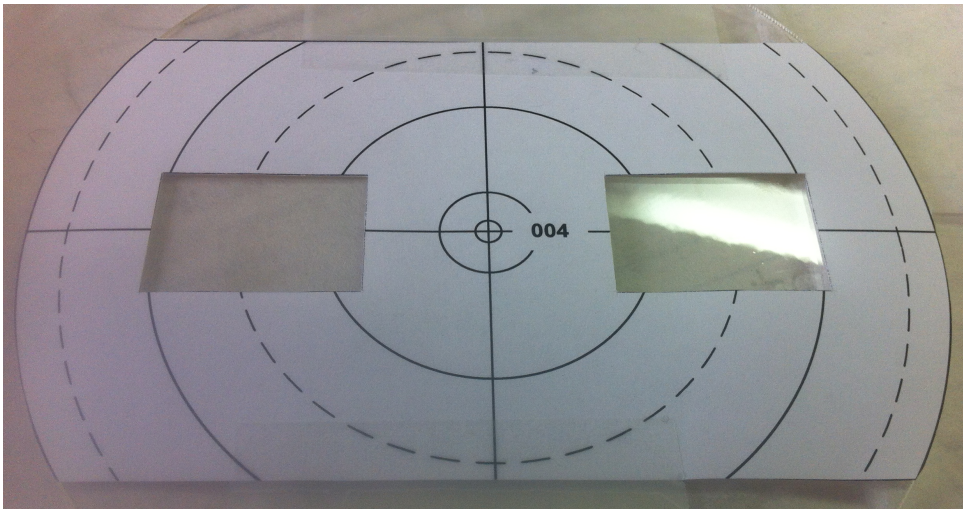

Figure 2.5: A paper mask was used to isolate two regions on an acrylic paint on plastic phase plate for testing with visible and near-IR Zygo interferometers (Credit: Kent Wallace).

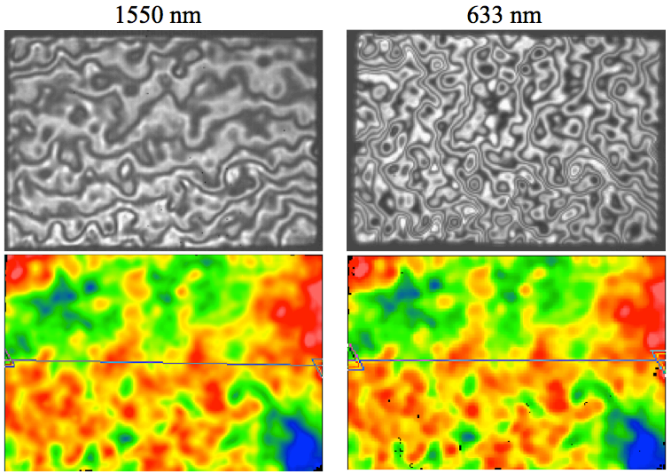

Figure 2.6: The fringe images (top) and reconstructed phase (bottom) of the region on the left side of the plate show close resemblance at the different wavelengths. The Peak-to-Valley and RMS measurements indicate the plate has very little chromaticity (Credit: Kent Wallace).

The limited dynamic range of phase that the interferometer is able to measure may be partly responsible for the higher variation in the Peak-to-Valley measurements. The black dots visible in the bottom right image in Figure 2.6 are evidence of where the instrument has saturated. The overall conclusion of this

analysis is that these phase plates are nearly achromatic. Similarly, the refractive index variations in the atmosphere show only a very small dispersion between visible and mid-IR wavelengths (~3×10^{-6} difference in refractive indices for the wavelengths in Figure 2.6, Cox 2001).

2.4 Phase measurements with the Quadrature Polarization Interferometer

Measurements of the wavefront distortion induced by the plates are performed with a Quadrature Polarization Interferometer (QPI), which operates with a 650 nm laser. This is a Mach-Zehnder interferometer that measures the phase of an optic in single pass transmission (Baker et al. 2004). The configuration results in a plate scale on the two cameras of 67 pixels per millimeter at the location of the plate, giving a resolution of about 15 μm. Maps of the phase are analyzed by taking the spatial power spectrum and structure function and comparing them to predictions of Kolmogorov theory, as discussed in the introduction section.

Figure 2.7 shows a layout of the instrument with the major components and location of the phase plate labeled. Not shown is a collimating lens and polarizer between the laser and first beam splitter, and image relay lenses in front of the cameras.

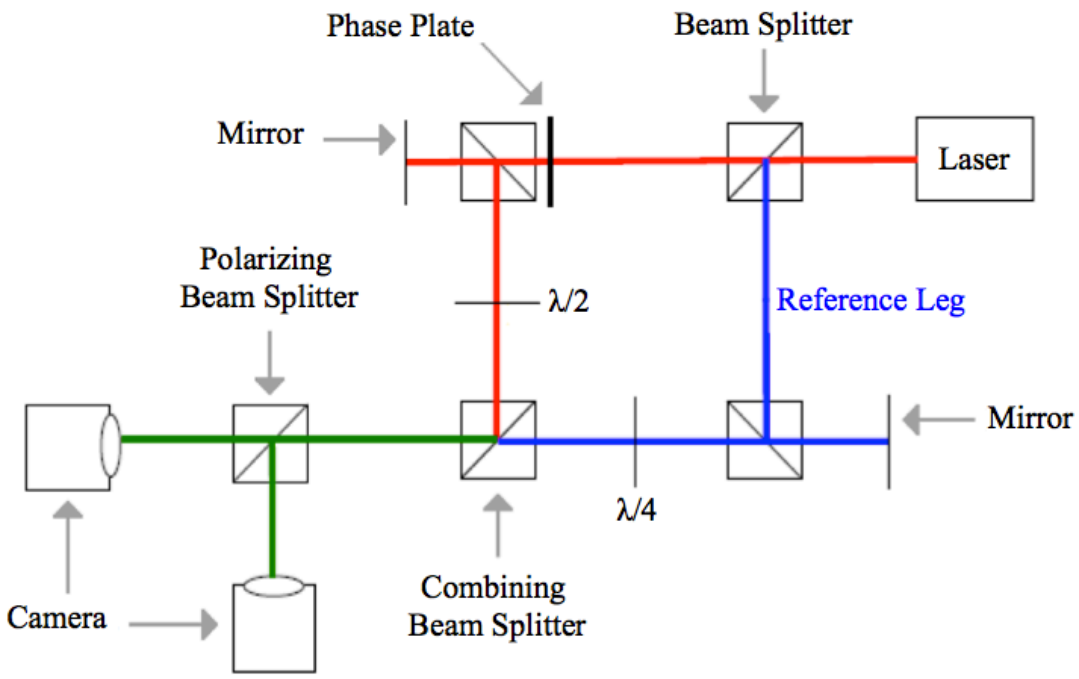

Figure 2.7: This diagram shows the layout of the Quadrature Polarization Interferometer (QPI). The turbulent phase plate is placed near the second beam splitter in the science leg of the interferometer (red), at a plane conjugate to the cameras. The blue path is the reference leg of the interferometer, and green is the combination of the two beams.

The quarter wave plate in the reference leg (blue) converts the linearly polarized laser light into circular polarization. In the test beam, the sine and cosine phase information from the turbulence plate is encoded on the 45° and 135° components of the electric field vector. A half wave plate, located before the combining beam splitter cube, rotates the coordinate system 45° so that the encoding is on 0° and 90° components. The subsequent polarization beam splitter separates the light so that the cosine of the phase of the combined beams is sent to one camera and the sine goes to the other. The data gathering computer does a bias subtraction and inverse tangent to get the 4-quadrant phase map of the optic. Subsequent processing unwraps this phase.

The electric field vector of the circular polarized reference beam has the form

$$\vec{\boldsymbol{E}}_{\boldsymbol{ref}} = \hat{\boldsymbol{x}} A\cos(\omega t) + \hat{\boldsymbol{y}} A\sin(\omega t) \tag{2.4}$$

where $\hat{\boldsymbol{x}}$ and $\hat{\boldsymbol{y}}$ are defined to be unit vectors in the plane of the optical bench and orthogonal to it, respectively, $\omega = 2\pi c/\lambda$ is the temporal frequency of the light, A_0 is the amplitude of the plane wave and $A = A_0/\sqrt{2}$. Note that for circular polarization the above expression is independent of coordinate system.

The form of the test beam after passing through the phase plate and half wave plate is

$$\vec{\boldsymbol{E}}_{\boldsymbol{test}} = \hat{\boldsymbol{x}} A\cos(\omega t + \emptyset) + \hat{\boldsymbol{y}} A\sin(\omega t + \emptyset) \tag{2.5}$$

where $\emptyset = \emptyset(x, y)$ is the phase aberration of the wavefront. At the combining beam splitter, the waves are added coherently, such that

$$\vec{\boldsymbol{E}}_{\boldsymbol{total}} = \hat{\boldsymbol{x}} A\left[\cos(\omega t + \emptyset) + \cos(\omega t)\right] + \hat{\boldsymbol{y}} A\left[\sin(\omega t + \emptyset) + \sin(\omega t)\right]. \tag{2.6}$$

The polarizing beam splitter then separates the wave into its components, and the cameras detect the power according to a square law given by

$$I = |E_x|^2 = A^2[\cos^2(\omega t + \emptyset) + \cos^2(\omega t) + \cos(2\omega t + \emptyset) + \cos\emptyset] \tag{2.7}$$

$$Q = \left|E_y\right|^2 = A^2[\cos^2(\omega t + \emptyset) + \sin^2(\omega t) + \sin(2\omega t + \emptyset) - \sin\emptyset]. \tag{2.8}$$

Here I and Q denote the signals that enter the two cameras. Because the detectors integrate over many cycles of the light wave, what they record is the time-averaged signals

$$\bar{I} = A^2(1 + \cos\emptyset) \tag{2.9}$$

$$\bar{Q} = A^2(1 - \sin\emptyset). \tag{2.10}$$

To measure the bias the test arm of the interferometer is blocked, then for the reference beam only, $\bar{I} = \bar{Q} = A^2/2$. This method is sensitive to the assumption that the intensity in the two arms is balanced, so they are determined prior to taking measurements and small adjustments to exposure times are used to minimize any discrepancy. Once the amplitude is determined, the phase modulo 2π is

$$\emptyset(x,y) = -\tan^{-1}\left[\frac{\bar{Q}(x,y) - A^2(x,y)}{\bar{I}(x,y) - A^2(x,y)}\right]. \tag{2.11}$$

The function used to preform the arctangent in software preserves the phasor quadrant information so the output spans a full range $-\pi$ to $+\pi$. Unwrapping the phase is done with an IDL routine that: (1) calculates the gradient of the phase, $\nabla\emptyset$, which converts 2π jumps into spikes, (2) adds or subtracts 2π to the spikes to keep all phase jumps in the range $[-\pi, +\pi]$, and (3) reconstructs $\emptyset$ given $\nabla\emptyset$ with a Poisson equation solver which makes use of the Fourier Transform. Figure 2.8 visually illustrates the combination of interference images that have a phase difference of 90° to form the 2D phase map.

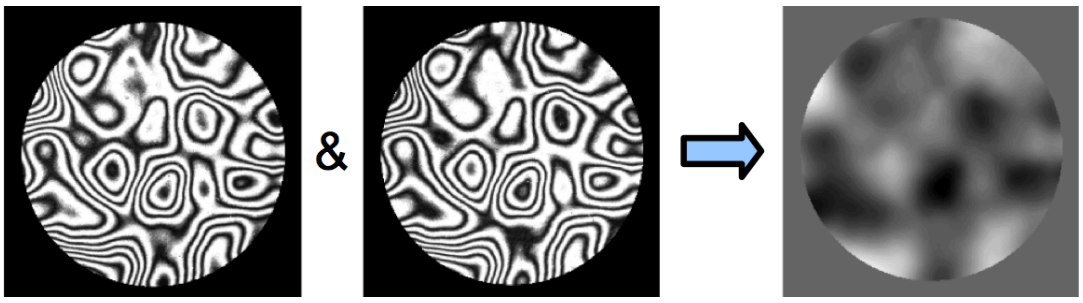

Figure 2.8: A visual illustration of interferograms from the two cameras being combined to produce a 2D phase map.

The QPI is located in the LAO on a Newport optical bench with state of the art vibration isolation. However, some wobble and drift in the fringes on short time

scales is apparent. I performed stability tests to assess the influence of these volatilities on phase measurements and plate analysis.

In Figure 2.9, the top row of images shows a reconstructed phase on the left, next to a difference image of this and a phase measurement taken 5 minutes later in the center. The difference between the initial phase and one taken after 20 minutes of elapsed time is on the far right. The increase in the minimum and maximum values, displayed below the difference images, indicate that indeed the phase measurements are changing as a function of time. To evaluate the effect on the power spectrum and structure function, the bottom three plots show these graphs for the three phase measurements. The center graph is a magnification of a section of the power spectrum, so the miniscule variation of the lines can be seen. The absence of substantial variability in these plots indicates the drift in QPI does not significantly impact our evaluation of the statistics of the phase plates.

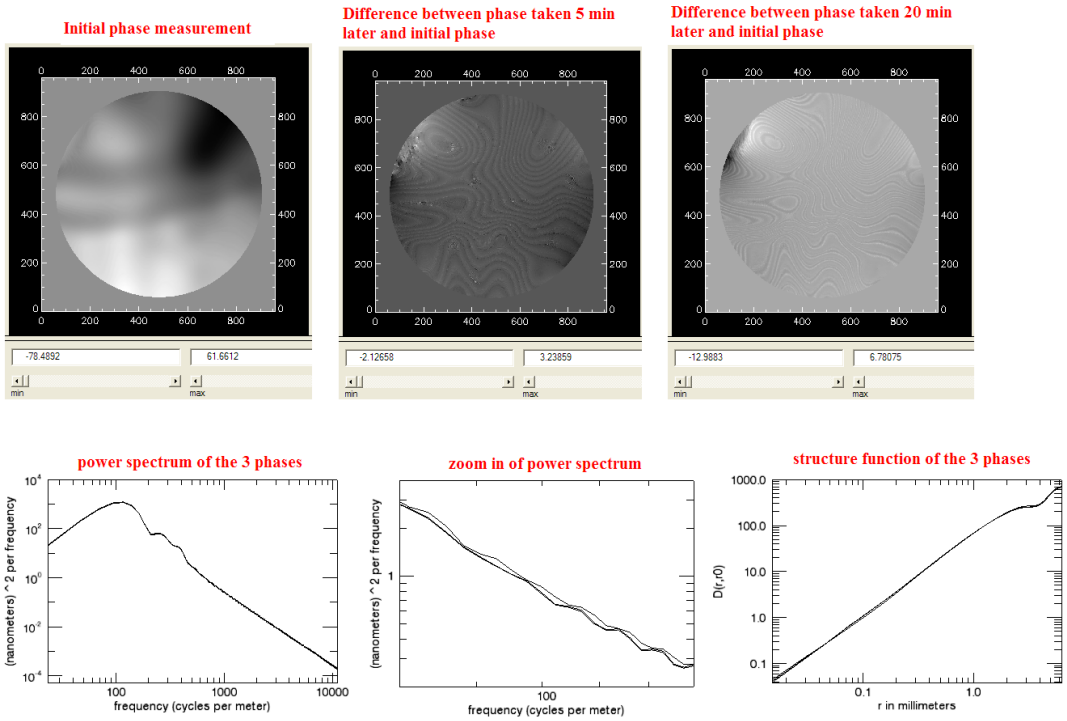

Figure 2.9: Stability tests of QPI show changes in the 2D phase maps on short timescales (top row of images). However, the tiny variability in the power spectrum and structure function plots (bottom row) indicate this does not significantly impact our evaluation of the phase plates.

The background noise in the instrument has also been measured. One example of a background power spectrum is shown along with the plate data in the left graph in Figure 2.14. The shape, strength, and location of peaks, have been observed to change slightly over time, but the levels are orders of magnitude below the plate data (except occasionally at the high frequency end), even for the weakest turbulence plates (such as Plate D). This indicates that, in general, there is minimal contribution of background noise to our assessment of the phase plates.

2.5 Results

The objective of this work is to produce turbulence plates with values of r_0 in the range 300 – 800 μm, measured at a wavelength of 650 nm (or equivalently, about 225 – 605 μm measured at a wavelength of 500 nm). This was set by the need to simulate 8 – 10 m class telescopes using test beam sizes of only a few centimeters. Through trial and error, methods to realize these parameters uniformly across a plate have been developed. Here I present four plates, two exemplifying this range of r_0, and two that show the minimum and maximum r_0's created thus far, which are 200 and 1200 μm, measured with 650 nm light. These are compared to phase maps generated by an atmosphere simulation code (Johansson et al. 1994).

The plots in this section (Figures 2.10 through 2.14) have the predictions of Kolmogorov theory shown as red dashed lines, and the phase data are thin black lines. The places where the data roll off near the edges of the graphs is an indication of the outer scale imprinted on the plate, which varies from 1 – 4 mm. The inner scale cannot be determined due to the noise floor of the measurements. In the power spectrum, a larger r_0 would correspond to shifting the dotted line downwards, while in the structure function the opposite is true.

Plates A and B (Figures 2.10 and 2.11) exhibit how Kolmogorov-like turbulence profiles have been achieved within the desired range. They are 14 cm and 7.6 cm diameter disks, respectively, and each had 8 locations tested with QPI. The regions analyzed are circular with 1.4 cm diameter. Three example images of reconstructed phase are shown for each plate below the graphs. These are useful in

visually verifying the uniformity of the 2D turbulence structures at different locations on the plate.

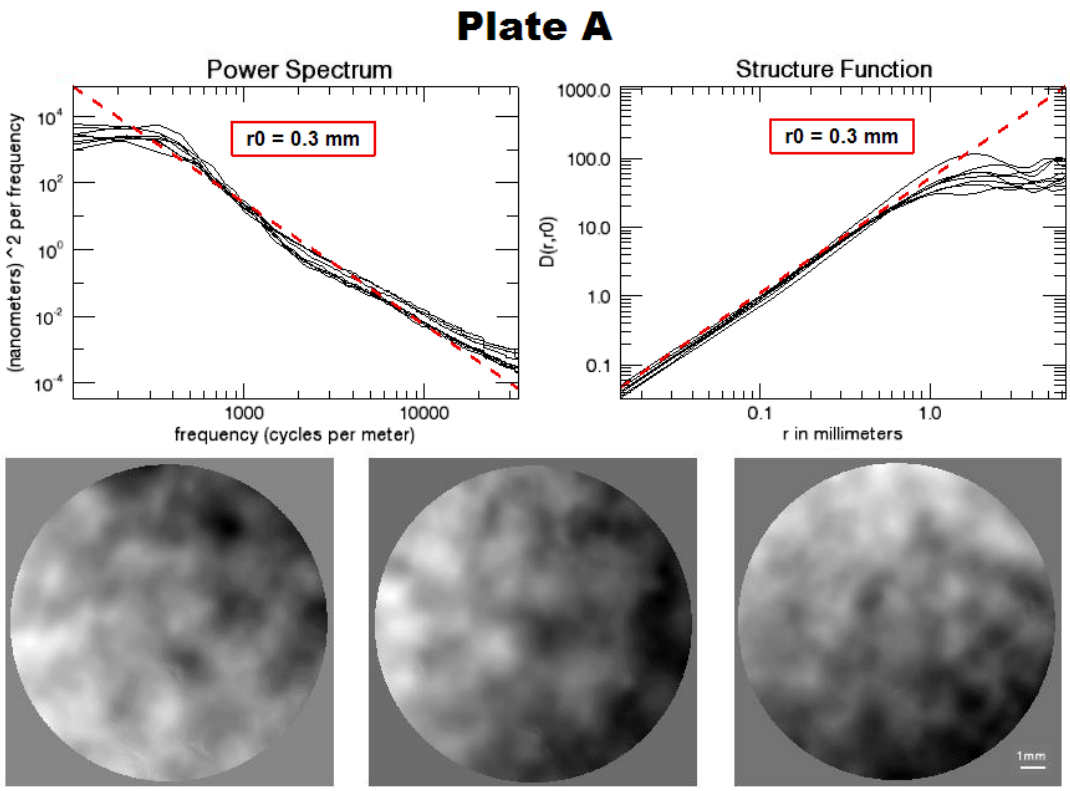

Figure 2.10: The structure function and radially averaged power spectrum for 8 locations on a 14 cm diameter disk. The dashed red lines represents Kolmogorov theory for r_0 = 0.3 mm, at 650 nm wavelength. The bottom images show reconstructed phase from the QPI for 3 of the regions tested. These are each 1.4 cm across, and verify the uniformity of the turbulence across the plate.

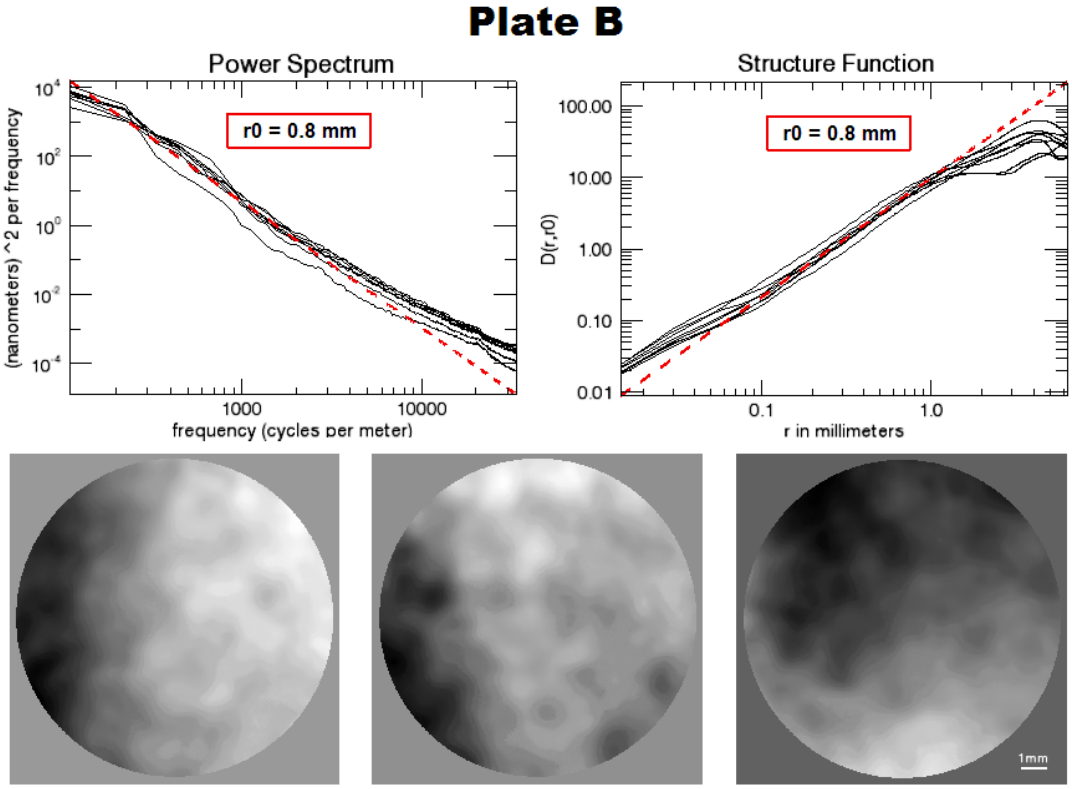

Figure 2.11: The structure function and radially averaged power spectrum resulting from measurement of 8 locations on a 7.6 cm diameter disk, where the red lines represents Kolmogorov theory for r_0 = 0.8 mm, at 650 nm wavelength. The bottom images show reconstructed phase from QPI for 3 of the locations tested. These are an indicator of the uniformity of the turbulence.

For comparison, and to ensure validity and proper calibration of the power spectrum and structure function programs, an identical analysis was carried out on computer generated phase screens. Figure 2.12 shows the structure function and power spectrum for 8 versions of phase created from different "seed" values in the simulation program, and 3 phase images. The median value of r_0 was used (0.5 mm), and the spatial scale and pixel size was set to be the same as the QPI measurements. The different iterations show some variability, as is also seen in the manufactured plates, and fit the theoretical slopes and target r_0 very well.

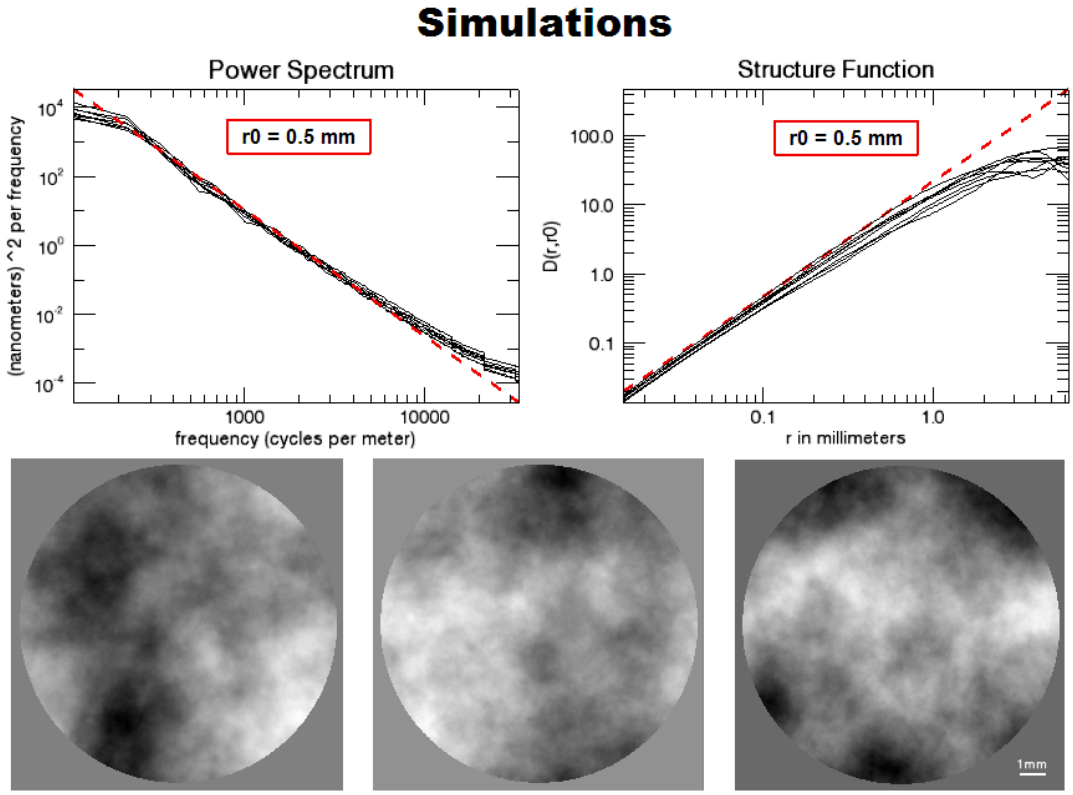

Figure 2.12: Eight versions of computer generated phases were evaluated, three of the 2D phase maps are shown. The similarity between these and the physical plates indicates our analysis is valid.

The effort of extending our method to creating plates with smaller and larger values of r_0 has met some success, although generally these plates have less well defined statistics and are more prone to cosmetic issues, like unevenness. It has also been much more difficult to produce these more extreme values repeatedly. Plates C and D (Figures 2.13 and 2.14) are examples of the minimum and maximum r_0's achieved thus far. These follow Kolmogorov statistics somewhat less well, and exhibit greater variability from one location to another. This method has also been somewhat successful at producing low order only and high order only turbulence

profiles. These may be useful for testing a woofer-tweeter AO system configuration, such as that used in Gemini Planet Imager AO system (Macintosh et al. 2006).

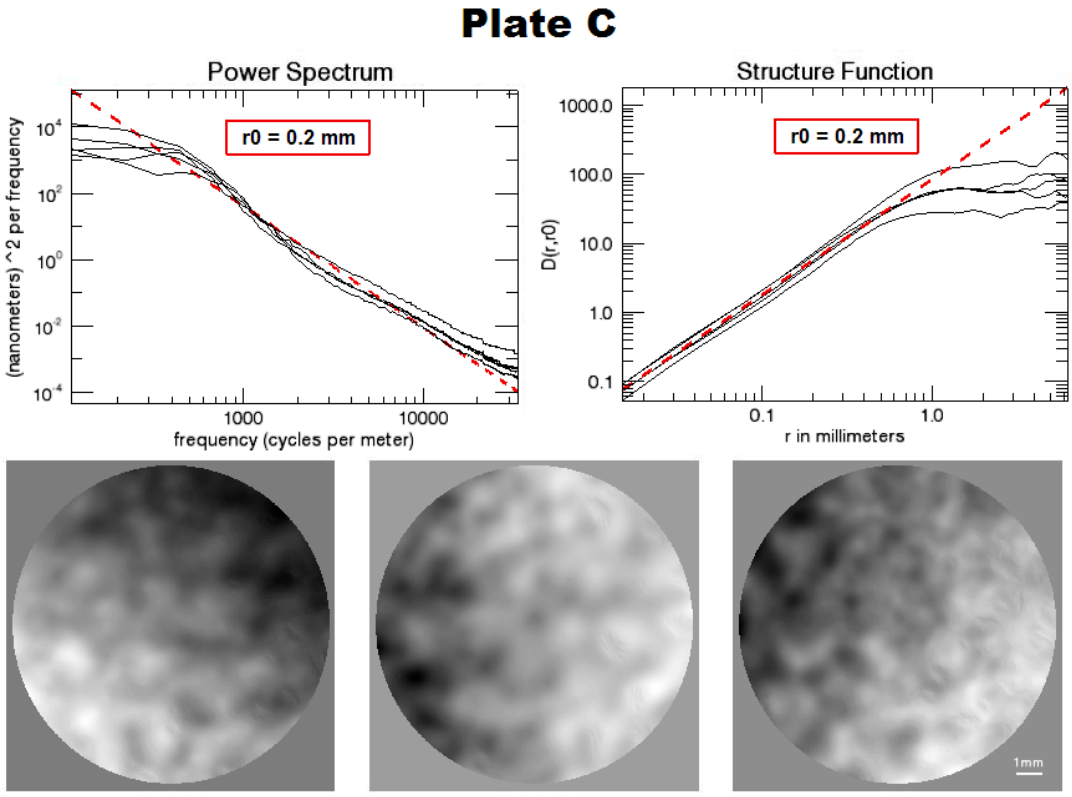

Figure 2.13: The structure function and radially averaged power spectrum for 5 locations on a 14 cm diameter disk. The dashed red lines represents Kolmogorov theory for r_0 = 0.2 mm, at 650 nm wavelength. The bottom images show reconstructed phase from the QPI for 3 of the regions tested.

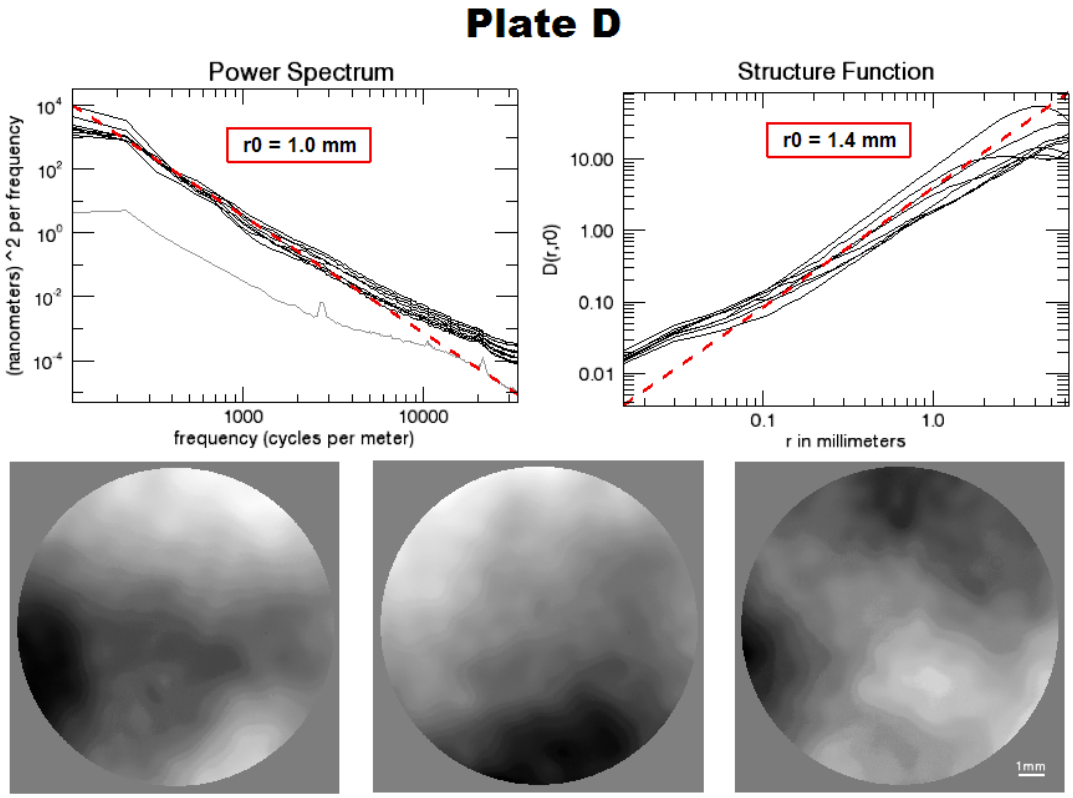

Figure 2.14: The structure function and radially averaged power spectrum for 8 locations on a 14 cm diameter disk. The dashed red lines represents Kolmogorov theory for $r_0 \sim 1.2$ mm, at 650 nm wavelength. The bottom images show reconstructed phase from the QPI for 3 of the regions tested. The gray line toward the bottom of the power spectrum represents the noise present in the QPI. A small remnant of the vibration near 2×10^4 cycles/m is evident in the data here, and also in Plate B.

It is interesting to note that the larger r_0 plates tend to show greater excess power at the high frequency end of the spectrum. A slight surplus is expected as a remnant of taking the Fourier Transform over a finite aperture, and is seen in both real and computer generated phase data. The additional excess in the large r_0 phases is likely due to noise in the QPI measurements. A measurement of this noise is shown against the power spectrum of Plate D in Figure 2.14. Slight residuals of the vibration near 2×10^4 cycles/m are seen in the data here and in Plate B (Figure 2.11).

In Table 2.2 the values of r_0, RMS, and Peak-to-Valley of the phase, for the four plates and simulations are tabulated with one standard deviation of the samples, all measured at a wavelength of 650 nm. These numbers show the expected trends of increased RMS and Peak-to-Valley for plates with smaller r_0's, i.e. stronger turbulence. The values for the 8 iterations of computer generated phases show good agreement with the manufactured plates.

	r_0 (μm)	RMS (μm)	Peak-to-Valley (μm)
Plate A	0.3	0.54 ± 0.09	3.42 ± 0.67
Plate B	0.8	0.44 ± 0.07	2.59 ± 0.50
Simulations	0.5	0.48 ± 0.08	2.81 ± 0.44
Plate C	0.2	0.72 ± 0.17	4.67 ± 1.16
Plate D	~1.2	0.30 ± 0.10	1.74 ± 0.45

Table 2.2: The values of r_0, RMS, and Peak-to-Valley determine the strength of the turbulence on a given plate. The RMS and Peak-to-Valley are given with ± one standard deviation. The computer generated phases (Simulations) agree well with what is found for the manufactured plates.

2.6 Performance on the ViLLaGEs instrument at Mt. Hamilton and comparison to sky turbulence

The Visible Light Laser Guidestar Experiments (ViLLaGEs) is a Micro-Electro Mechanical Systems (MEMS) based visible-wavelength adaptive optics testbed on the Nickel 1-meter telescope at Lick Observatory. Its purpose is to compare the effectiveness of open and closed loop control methods with a MEMS device (Grigsby et al. 2008). The experiment motivated layout of this instrument allows simultaneous evaluation of corrected and uncorrected (not incident on the deformable mirror) paths, as shown in Figure 2.15. The instrument is also capable of switching to an internal fiber light source and turbulence plate for testing and calibration purposes. This feature was used to compare the temporal power spectrum

of a phase plate with actual sky turbulence. In addition, a brief analysis to determine how well the sky follows Kolmogorov statistics was carried out.

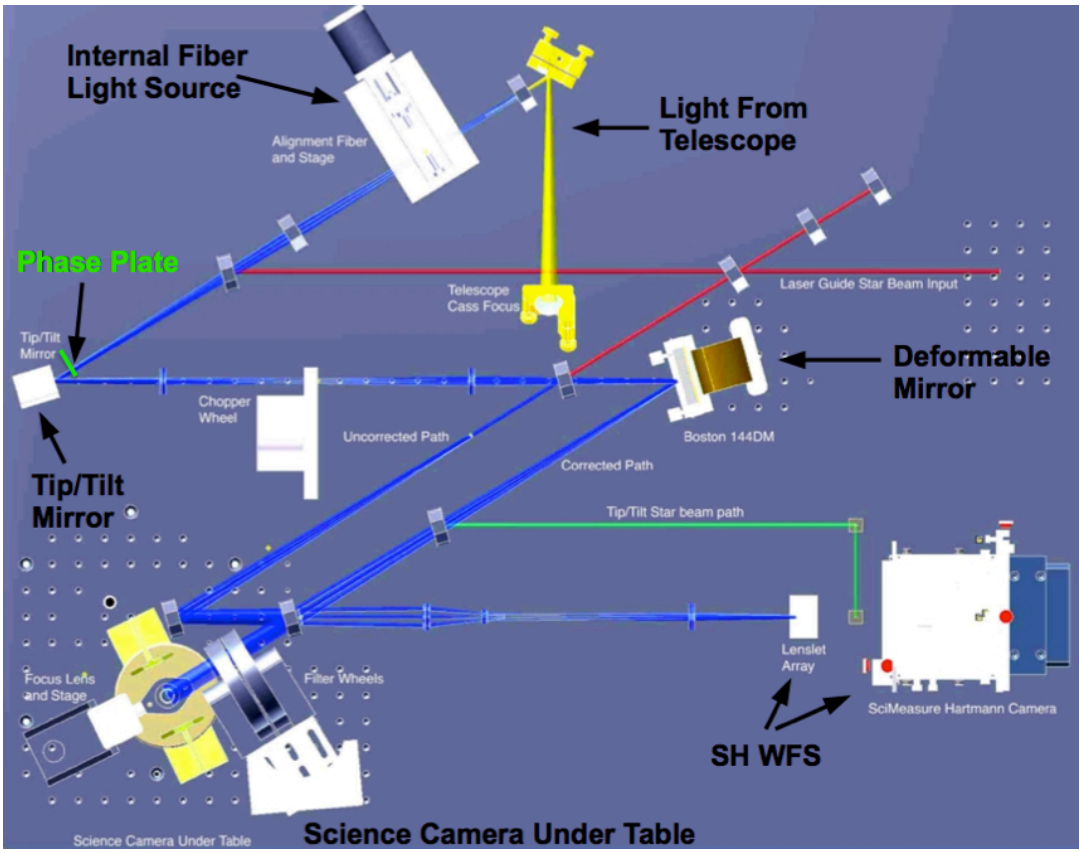

Figure 2.15: The optical layout of the ViLLaGEs instrument showing the two separate paths the light travels, with only one incident on the deformable mirror. The phase plate (shown on the left in bright green) was placed just ahead of the tip/tilt mirror.

Data taken with ViLLaGEs between June and November of 2010 were inspected. Figure 2.16 shows a temporal power spectrum of the phase plate, the general shape of which was constant between measurements taken several months apart and fits the desired statistics well. Note that the phase plate on the ViLLaGes optical bench is mounted on a rotating stage to mimic wind-blown frozen-flow turbulence, thereby converting the spatial variations on the plate to temporal variations as recorded by the system. To analyze the power spectrum of the sky, 40

sets of data from 7 different nights spanning a 4-month period were examined. It was found that the power spectra fell into three categories: (1) shallow (i.e. a lack of power at low frequencies and an excess at the high end), (2) bowed out (an excess of power at mid frequencies), or (3) followed Kolmogorov theory well. Examples of each of these are shown in Figures 2.17 – 2.19, respectively. Each type occurred in approximately equal numbers, meaning the sky data were following Kolmogorov power law statistics in only about a third of the data sets.

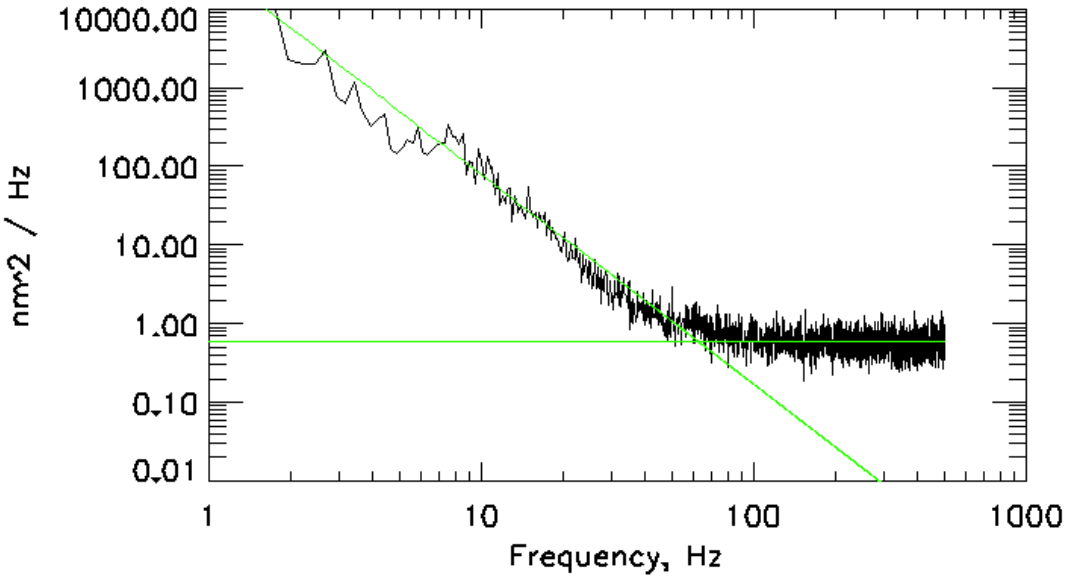

Figure 2.16: Power spectrum of the turbulence plate in the ViLLaGEs instrument. The black line shows measurements from the open-loop path, and the horizontal line is the phase measurement noise floor. The tilted line represents Kolmogorov theory, which the data match very well.

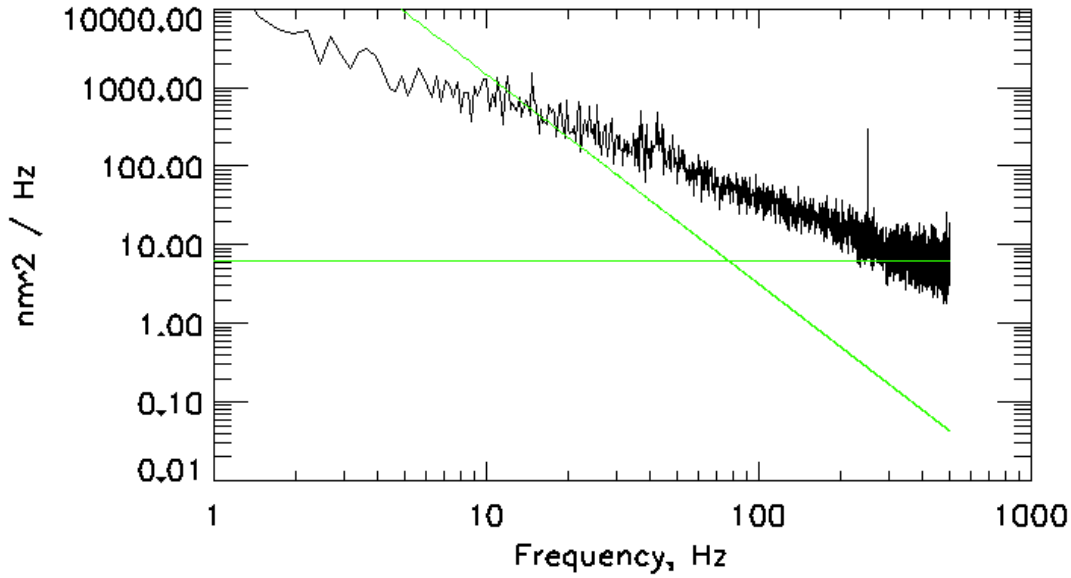

Figure 2.17: Example of shallow sky power spectrum. The black line shows measurements from the open-loop path, the horizontal line is the phase measurement noise floor, and the tilted line represents Kolmogorov theory. This type occurred in one third of the 40 data sets examined.

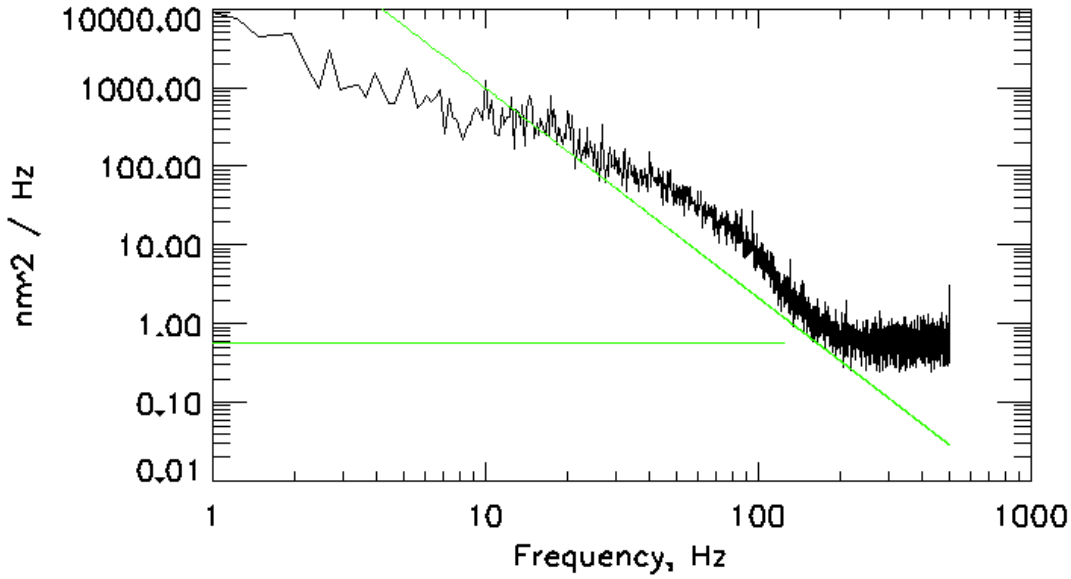

Figure 2.18: Example of bowed sky power spectrum. The black line shows measurements from the open-loop path, the horizontal line is the phase measurement noise floor, and the tilted line represents Kolmogorov theory. This type occurred in one third of the 40 data sets examined.

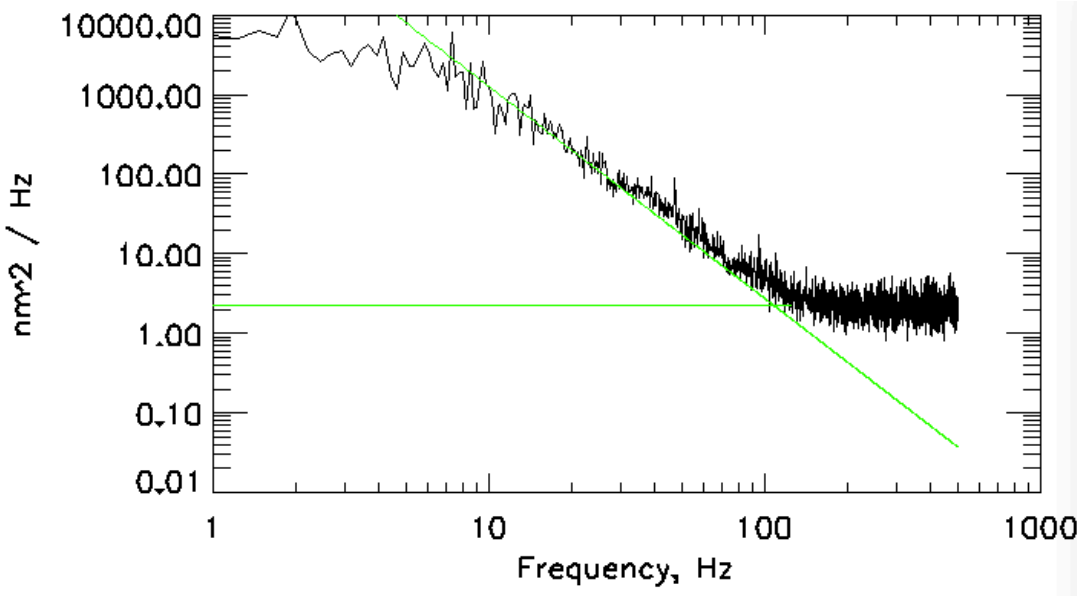

Figure 2.19: Example of sky power spectrum that follows Kolmogorov statistics well. The black line shows measurements from the open-loop path, the horizontal line is the phase measurement noise floor, and the tilted line represents Kolmogorov theory. This was only observed in about one third of the 40 data sets examined.

The seeing parameter of interest, r_0, was also compared between the plate and on-sky data. Based on 15 data sets from 6 nights between June and September of 2010, the average for the turbulence plate was 9.9 cm, after being scaled to the 1 m diameter aperture of the Nickel telescope. The average for the sky, based on the 12 data sets that exhibited Kolmogorov turbulence, was 8.7 cm. Since r_0 is a wavelength dependent parameter, these values are stated for a wavelength of 650 nm. The phase measurements were taken with the ViLLaGEs open-loop Hartmann sensor, where the spot size is 1.6 arcseconds and the plate scale 1.73 arcseconds/pixel. The plate scale was determined by translating a white light source across the pupil (Morzinski et al. 2010). Independent measurements of the turbulence plate using the QPI in the laboratory determined that the expected r_0 of the plate should be 12.5 cm, when

scaled to the telescope aperture. Earlier measurements of the seeing at Mt. Hamilton showed a median r_0 of the sky near 10 cm (Max 2010). This discrepancy between the expected value and the actual measurements can be understood by considering the variability in parameters such as spot size, the plate scale of the Hartmann sensor, and the peak wavelength of the starlight. For example, decreasing the value of the plate scale by only 10% would increase the calculated r_0 by ~13%. Morzinski et al. (2010) found that the spot size can range from a diffraction-limited 0.6 arcseconds to 1.9 arcseconds in the Hartmann sensor (a broad-band CCD). The reasonable agreement between the r_0 for the plate and sky indicates that the plate successfully met its design requirements, which was to have an r_0 on the order of what the median value is for this site.

2.7 Comparison to plates manufactured by other processes

Plates fabricated by the method I developed have been compared to several created with more commercial processes. A few years before I started this project, several lithographically etched glass phase plates were specialty fabricated at Lawrence Livermore National Laboratory (LLNL) for use in LAO testbeds. I analyzed these using the methods described in this chapter. I also evaluated a turbulence plate fabricated by the company Lexitek, which uses a near-index matching dual material approach, provided to us for study courtesy of LLNL.

The etched glass plates were imprinted with Kolmogorov phase maps generated by the simulation program discussed in section 2.5. Figure 2.20 shows the structure function and power spectrum plots obtained from measurements taken with

QPI for one of these plates. Both graphs indicate an excess of high frequencies, and do not fit the prescribed slopes well. Additionally, a consequence of the step-like features resulting from lithography is high intensity variations that interfere with the ability of a Shack-Hartmann WFS to measure the phase distortion it produces. The experimental procedure of creating this type of turbulence screen involved a considerable financial investment, but produced only semi-useful results.

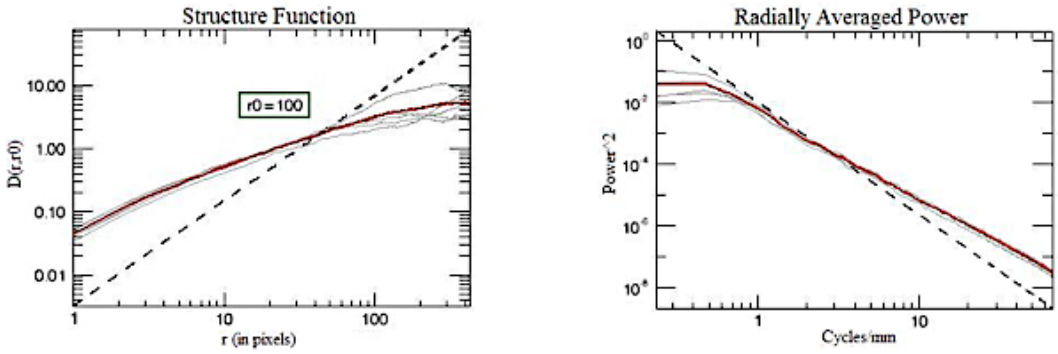

Figure 2.20: Power spectrum and structure function from measurements taken with the QPI on a lithographically etched glass plate. The red line is the average of the individual measurements (plotted in grey). Both show significant excess high frequency, and do not closely follow Kolmogorov statistics.

The principle behind near index matching technology is that when two materials with slightly different indices of refraction, n_1 and n_2, are brought together at an uneven or contoured interface with profile $h(x)$, the resulting optical path difference (OPD) imprinted on an incident plane wave will be

$$OPD(x) = h(x)[n_1(\lambda) - n_2(\lambda)] = h(x)\Delta n(\lambda), \qquad (2.12)$$

provided the exterior surfaces of both materials are planar. Thus, for materials with $\Delta n \sim 0.02$ a profile height of $\sim 50\lambda$ is necessary to produce an OPD of 1λ. Lexitek chose to construct plates by combining machine etched acrylic with castable optical cement. The device I tested with QPI was approximately 8 cm in diameter and had a

thickness of about 1 cm. Figure 2.21 contains the power spectrum and structure function plots obtained with five measurements of the phase, along with a mosaic of the interferogram images that span the diameter of the plate. The r_0 is given as 1.31 cm, so this value was used in the plot fits. Both graphs show the data to have somewhat shallower slopes than predicted by theory, but significantly less so than for the plate in Figure 2.20.

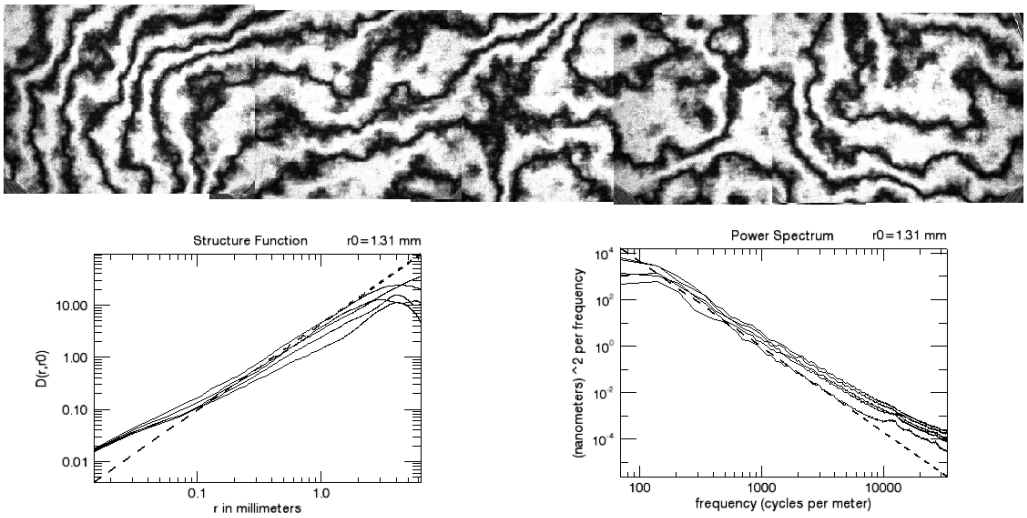

Figure 2.21: A mosaic of interferogram images and data taken with QPI of a near index matching plate fabricated by Lexitek. It has similar characteristics as Plate D, discussed in Section 2.5, but the production process is expensive and limited in the achievable range of r_0.

Based on the above appraisal, near index matching is confirmed as a viable means of creating turbulent phase plates with representative Kolmogorov turbulence, albeit at a much higher cost and with different constraints than the method presented in this thesis.

As a final comparison, Figure 2.22 shows interference image mosaics of plates manufactured at the LAO. The top strip is for a plate coated with hairspray, and the lower is the clear paint. These show the structure and uniformity of the phase

variations across the plates. When compared with the mosaic in Figure 2.21, the different textures associated with the materials and manufacturing process are evident. However, for all three cases the statistics are in fairly good agreement with Kolmogorov theory.

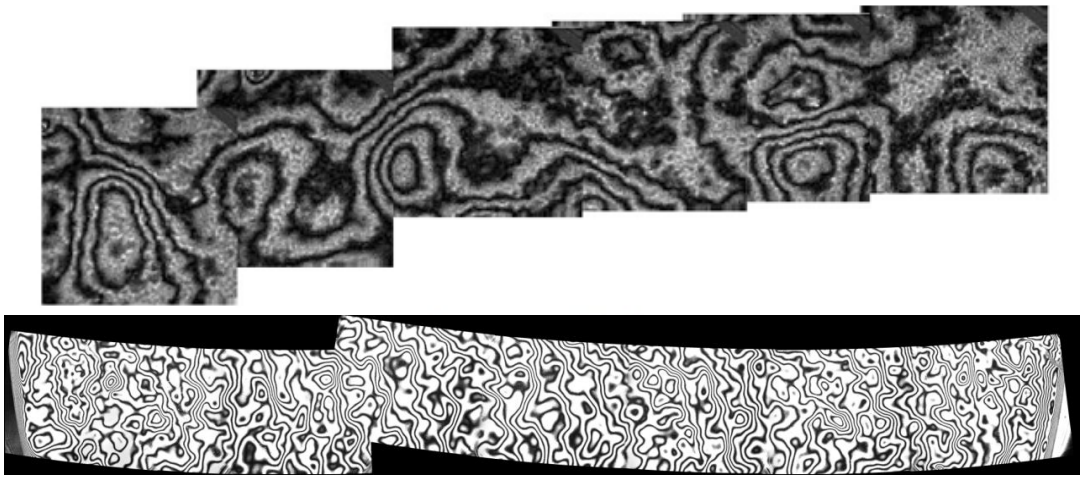

Figure 2.22: Mosaics of interferogram images from QPI for plates made at the LAO with hairspray (top) and clear acrylic paint (bottom). Although the texture of the structures are different for the two materials, phase variations produced by both have statistical properties that follow Kolmogorov theory well.

2.8 Decomposition of phase into orthogonal polynomials

Using the machinery of linear algebra, a function can be decomposed (or separated) into the components of a set of orthonormal basis function. This is also the case for wavefront phase aberrations induced by atmospheric turbulence. A convenient choice for astronomy is Zernike polynomials, which are defined over the unit circle (Born et al. 1997). Opticians often use these because they describe some of the aberrations commonly found in the human eye. For example, Z_2^0, the Zernike polynomial of order 2 and degree 0, gives a measure of the strength of focus. The

mathematical expression for a Zernike polynomial of order n and degree m (Porter et al. 2006) is

$$Z_n^m = \begin{cases} N_n^m R_n^{|m|}(\rho)\cos(m\theta); & for\ m \geq 0 \\ -N_n^m R_n^{|m|}(\rho)\sin(m\theta); & for\ m < 0. \end{cases} \quad (2.13)$$

Here ρ is the normalized pupil radial coordinate, θ is the angular pupil coordinate, $R_n^{|m|}(\rho)$ is defined as

$$R_n^{|m|}(\rho) = \sum_{s=0}^{(n-|m|)/2} \frac{(-1)^s (n-s)!}{s!\,[(n+|m|-s)/2]!\,[(n-|m|-s)/2]!} \rho^{n-2s} \quad (2.14)$$

and the normalization factor N_n^m is given by

$$N_n^m = \sqrt{\frac{2(n+1)}{1+\delta_{m0}}}\,. \quad (2.15)$$

The Kronecker delta function, δ_{m0}, is 0 for all $m \neq 0$ and 1 otherwise. The polynomials can also be indexed using a single number index j, which is related to the order n and degree m by

$$j = \frac{n(n+2)+m}{2} \quad (2.16)$$

Thus, if $\emptyset(r, \theta)$ is some arbitrary function, its expansion over a circle of radius R is given by

$$\emptyset(\rho R, \theta) = \sum_j a_j Z_j(\rho, \theta)\,, \quad (2.17)$$

where the a_j are the coefficients.

With Zernike polynomials (and expansions in general), the amount of spatial information in each term increases with larger j. Thus, in order to replicate a function

with fine spatial details, a large number of Zernike polynomials are needed. To truly reproduce a realistic aberrated phase profile would require an infinite number of Zernikes. However, because the coefficients of the higher order terms tend to zero, a fairly small number of terms can be used to give a reasonable approximation.

A Zernike representation of the Kolmogorov spectrum of turbulence can be obtained by evaluating the variance of the expansion coefficients (Noll et al. 1976). I wrote an IDL program to calculate these for decomposition of the phases measured with QPI and the simulations they are compared to in Section 2.5. Figure 2.23 shows results of this analysis on 1 (left plot) and 50 (right plot) iterations of simulated phase, compared to coefficient variances expected by Kolmogorov theory (solid lines). For all cases piston, tip and tilt (the first 3 indices) have been removed. The first obvious result is that decomposition of only one phase map does not yield any significant information about how well the statistics follow Kolmogorov theory. I found that it required averaging over about 20 iterations of the simulations for convergence to begin to appear.

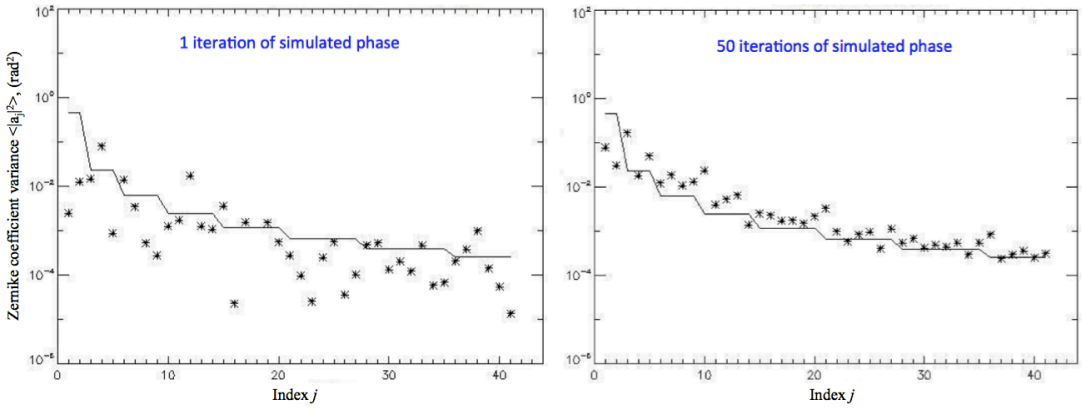

Figure 2.23: Zernike decomposition of simulated phase maps, with the size and spatial scale of QPI images, only show convergence to what is expected by Kolmogorov theory when a large number of iterations are included. This makes it an inconclusive test for the phase plates, whose finite size limits the number of unique measurements obtainable.

Zernike polynomials are an extremely useful tool in understanding the nature and composition of an arbitrary wavefront defined on a circle. However, for the case of assessing the properties of the turbulence plates discussed in this work, they have proved inconclusive. The finite size of the disks makes it possible to only gather a small number of unique phase measurements. Although this can be near 20 for the larger sizes of plates, the process of taking measurements with QPI is slow and very precise movements of the disk position are not currently possible (this is done by hand). The value of Zernike analysis was explored in the case of plates were 8 – 12 measurements had been acquired, but no clear conclusions could be drawn due to the high variability of the data points (as seen in the left plot of Figure 2.23). An alternate method, involving subtracting off successive polynomials and measuring the remaining wavefront error was also investigated, but this suffered from a similar issue. Overall, the conclusion is that the power spectrum and structure function are

the most appropriate analysis tools for determining how closely the manufactured plates adhere to Kolmogorov theory.

2.9 Discussion

The processes I developed have resulted in the creation of numerous successful plates with a variety of strengths, but some issues remain a hindrance to fully expedited manufacturing. As mentioned previously, achieving good quality plates with differing strengths of turbulence involves controlling certain variables. Mainly, the distance between the plate and the can, the speed of the can, the number of layers applied and time between applications. The amount of airflow present during drying is also important, and should be minimized for best quality. Through repeat trials with the same parameters it is apparent that other, currently uncontrollable, factors also affect the outcome. Most notably seems to be the fullness of the spray can, but it is very possible that conditions such as humidity and barometric pressure are also of significance.

One of the most challenging obstacles has been dust particles becoming entrapped in the spray before it dries. Maintaining a clean environment around and inside the spraying apparatus has proved beneficial, but moving it to a clean room will be the best solution. Additionally, plans are underway to replace the spray can with an airbrush system to allow precise control of the amount of paint being deposited. This will require recalibration and characterization of the spray parameters but will result in improved mastery of the process.

Certain aspects of the current process sporadically give rise to varying results, but the relative simplicity, speed, and low cost of the materials, means that undergoing several trials to produce the desired plate is completely reasonable. Applying a single coat of paint takes only a few minutes, and the time before a plate is ready for testing varies from hours to days, depending on the number of layers applied and the dry time between them. In the event of excessive contamination or other problems the acrylic can be removed from the substrate very effectively with the strategic use of hot water, allowing it to be reused.

In this chapter, I described an innovative method of producing fixed aberration phase plates that produce wavefront distortions with characteristics similar to atmospheric turbulence. I demonstrated several means of adjusting the statistical properties imprinted on the plates by varying parameters involved in the manufacturing process, and achieved values of r_0 ranging from ~ 200 – 1200 μm measured at 650 nm (or 150 – 905 μm measured at 500 nm). Both the substrates and spray are durable, lightweight materials. Dust can be removed from a finished plate with compressed air, but fingerprints cannot be easily cleaned off the acrylic so careful handling is necessary. Also, what appear to be tiny cracks may develop in the paint where it comes into repeat contact with abrasion (such as being taken in/out of a mounting apparatus). The longevity of the turbulence characteristics of the acrylic is good, evidenced through repeat measurements of plates created in 2008. This method has produced valuable devices for calibration and testing of AO systems, but there

still remains room for additional characterization and improvement of the process, which will be discussed further in Chapter 5.

Chapter 3

Laser Guide Star Adaptive Optics

3.1 History and motivation

Many future large ground-based telescopes will require single or multiple laser guide stars (LGS) in nearly all science operations. Use of LGS along with AO allows significant improvement of resolution through correcting image distortion induced by atmospheric turbulence at nearly any location in the sky. This is necessary for AO observations of astronomical targets that lack bright nearby natural guide stars (NGS).

The US military first proposed using laser beacons to create artificial sources to overcome this problem in a classified program, but a few years later the concept was independently suggested by Foy & Labeyrie (1985) for astronomy. The methods considered were: (1) Rayleigh backscatter in the dense regions of atmosphere up to ~30 km, and (2) resonance fluorescence of mesospheric sodium atoms which are concentrated in a ~10 km thick layer, centered at an altitude of ~90 km. The first successful tests of a Rayleigh LGS were performed at the Starfire Optical Range (SOR) 1.5-m telescope (Fugate 1992). The first astronomical LGS AO systems were installed at the Lick (Max et al. 1997) and Calar Alto (Eckart et al. 2000) observatories in the mid 1990s. Shortly thereafter, the technology was mature enough

to be installed at 8–10 m class telescopes, including Keck II (Wizinowich et al. 2006), the VLT (Bonaccini Calia et al. 2006), Gemini North (Boccas et al. 2006), and Subaru (Hayano et al. 2010).

Sodium LGS operating at a wavelength of 589 nm are preferable to Rayleigh guide stars due to their high altitude (allowing a larger fraction of the turbulence to be measured), fluorescence at visible wavelengths, and a large fluorescence cross section-abundance product compared to the other constituents of the upper atmosphere (Happer et al. 1994). Because powerful diffraction-limited laser beams at 589 nm are expensive to produce, careful attention must be paid to optimizing the laser format (spectrum, polarization, spot size) in order to maximize the return signal. Numerical models allow us to investigate the various physical mechanisms occurring in the laser-sodium system that affect the number of photons returned to the telescope. Results presented here were obtained using a density-matrix calculation with coupled velocity groups, and included the important physical effects of Larmor precession due to the geomagnetic field, radiation pressure (recoil), saturation, velocity-changing and spin-randomizing collisions (Holzlöhner et al. 2010a). The LGSBloch package runs in Mathematica, and is based on the Atomic Density Matrix package written by S. Rochester[‡].

Motivation for this specific research is provided by the near future upgrade of the AO system on the 3 meter Shane Telescope at Lick Observatory. The Shane

[‡] Available at http://budker.berkeley.edu/ADM

hosted the first experiments in Na LGS AO, with observations starting in 1996, and provides for regular astronomical science observing to this day. The upgraded new system will incorporate many of the recent advancements in AO technology and lessons learned from laboratory and on-sky experiments in order to provide higher Strehl, improved sensitivity, and greater wavelength coverage for astronomers (Kupke et al. 2012). This second generation system uses a 32×32 actuator Micro-Electro Mechanical Systems (MEMS) deformable mirror, with a higher sensitivity wavefront sensor (WFS), and new fiber laser that was developed at Lawrence Livermore National Laboratory (LLNL). This laser has several advantages over the dye laser currently in use. Not only is the fiber technology more compact and energy efficient, but this laser allows adjustments to the pulse and spectral format, for optimal coupling to the mesospheric sodium atoms. The initial goal of my investigation has been to ascertain the ideal values of these parameters, and to estimate the return signal this new laser will produce.

In the next section, I present details of the sodium physics relevant to the numerical model, followed by descriptions of work towards finding the optimum pulse and spectral formats in Sections 3.3 and 3.4, respectively. Section 3.5 addresses the potential benefits of uplink correction of the laser beacon, and gives the projected return flux for the new LGS at Lick Observatory. Section 3.6 presents the suggested optimal format for the LLNL fiber laser, and discusses how the results of this research can be useful for optimizing LGS at other observatories.

3.2 The physics of sodium-light interactions

Sodium LGS take advantage of the $3^2S_{1/2} - 3^2P_{3/2}$ dipole transition in atomic sodium, known as the D_2 line. The ground state consists of two hyperfine multiplets, with 8 magnetic substates combined. The hyperfine states are separated by 1.77 GHz, splitting the D_2 line into the D_2a and D_2b transition groups. These two groups correspond, respectively, to the $F = 1$ and $F = 2$ ground states, where F is the total atomic angular momentum quantum number. The four excited state multiplets ($F = 0$, …,3) are separated by only 16, 34, and 60 MHz, and contain a total of 16 substates. Figure 3.1 shows the atomic structure of sodium starting from the Bohr model (on the left) and ending with the hyperfine states and energy separations on the far right.

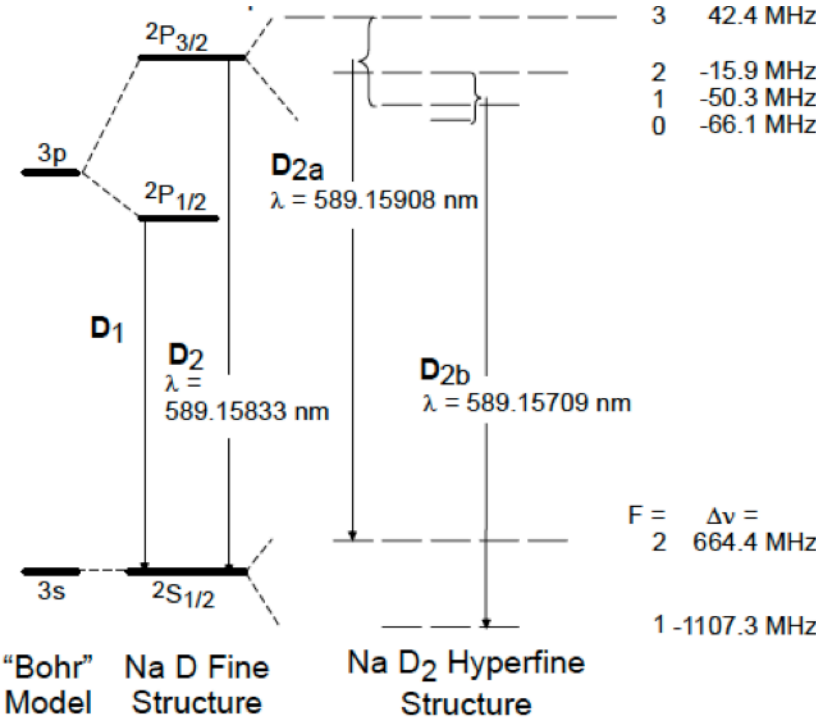

Figure 3.1: The atomic structure of sodium, starting from the Bohr model of the atom on the left, and ending on the right with the hyperfine states of the D_2 line. The 1.77

GHz separation of the ground states requires that LGS address both transition groups for optimal coupling to the light field.

At mesospheric temperatures of about 190 K, the motions of the atoms result in the D_2a and D_2b lines being Doppler broadened to ~1 GHz each, giving rise to the characteristic two-peaked profile shown in Figure 3.2. This photon return data from the 50 Watt Fasortronics laser at the Starfire Optical Range (SOR) in New Mexico also shows the considerable increase in return with a circular polarized beam (blue), as compared to linear polarization (red). Here the return is a factor of ~ 2 higher, but this ratio depends on the angle between the LGS propagation direction and Earth's magnetic field.

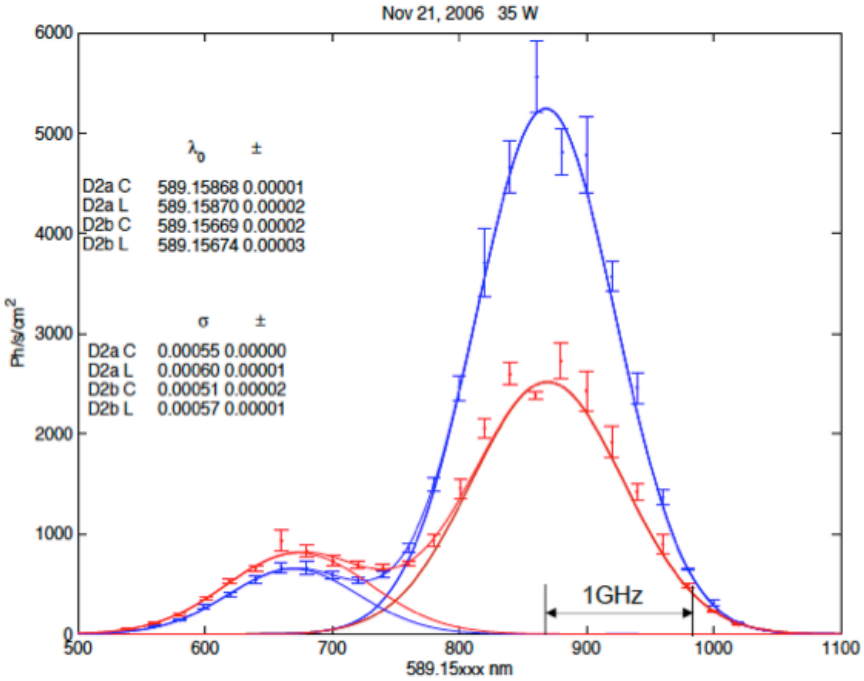

Figure 3.2: Measurements of the number of returned photons from the SOR Fasortronics laser as a function of wavelength, for both circular (blue) and linear (red) polarized beams. The two peaks are caused by the 1.77 GHz separation of the ground states. The relative motion of the atoms in the light beam gives each the ~ 1 GHz linewidth.

The enhanced return flux with circular polarized light is the result of the phenomenon of optical pumping. When an atom encounters a circularly polarized photon of the correct wavelength to cause a transition to the excited state, the value of the magnetic quantum number, m, must change by ± 1 depending on the handedness of the light, as required by conservation of angular momentum. After several cycles of excitation and spontaneous emission (the excited state lifetime is ~ 16 ns), a majority of the atoms in the velocity group corresponding to the peak of the D_2a line will be stuck cycling between the $F = 2, m = \pm 2$ ground state and the $F' = 3, m = \pm 3$ excited state. The benefits are that this is the strongest transition of the entire D_2 group, atoms are forbidden by selection rules from decaying to the $F = 1$ ground state, and the florescence is directed preferentially along the light beam (dipole transition).

Figure 3.3 shows the emission patterns for atoms spontaneously emitting linearly and circularly polarized photons, after excitation by a vertically oriented laser beam. In general, when an excited atom transitions back to the ground state, its magnetic quantum number, m, can change by 0 or ± 1 with equal probability. If m changes by ± 1 the emitted photon will be right or left handed circular, and if there is no change then it is linear polarized. However, atoms in the $F' = 3$ excited state with extremal values of m have only one possible transition available (the $F = 2$ ground state) during which they must have $\Delta m = \pm 1$. The peanut shaped nature of this emission increases the likelihood that the fluoresced photon will return to the telescope.

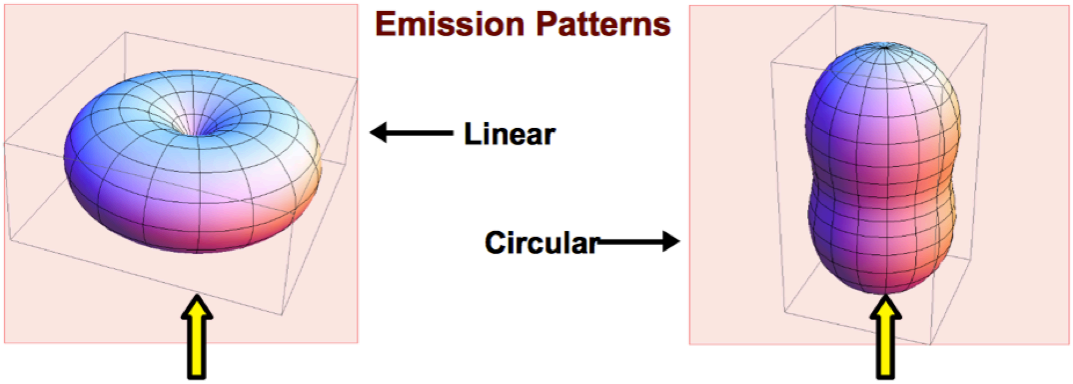

Figure 3.3: Emission patterns for sodium D_2 transitions, in which the emitted photon is linear polarized (left) and circular polarized (right). The yellow arrows indicate the direction of laser propagation. The circularly polarized light is much more likely to be directed back toward the telescope, resulting in a brighter LGS.

Based on theoretical and experimental considerations, maximizing the number of photons emitted back towards the telescope involves use of a circularly polarized beam centered on the D_2a line, with ~10% of the light tuned to the D_2b transition (Milonni et al. 1998, Holzlöhner et al. 2010a). Without this "repumping," in thermal equilibrium 3/8 of the atoms would not interact with the light field, and those atoms that later decay into the $F = 1$ ground state would be lost. This optical pumping with repumping strategy allows the most atoms to become trapped in the aforementioned desirable two-state system.

Figure 3.4 shows this predicted increase in emitted photons for a single frequency CW LGS as a function of irradiance level for propagation parallel and perpendicular to the magnetic field (angle given on the plot as θ), located at Mt. Hamilton (solid) and Paranal, Chili (dashed), with and without repumping (q is the percentage of the total power tuned to D_2b). The highest return is seen for propagation parallel to the magnetic field with 12% repumping (green line), and the

lowest is when the laser is perpendicular to the magnetic field and there is no repumping (orange line). The stronger field at the more polar latitude reduces the size of the magnetic resonance bump, especially in the perpendicular case. Return from a linearly polarized CW LGS would closely follow the lower two curves on this graph, because the strong Larmor precession from the orthogonal magnetic field nearly completely suppresses optical pumping, even with repumping. Lastly, the small change in the results for the two different locations indicate that these general findings are likely applicable at any observing location.

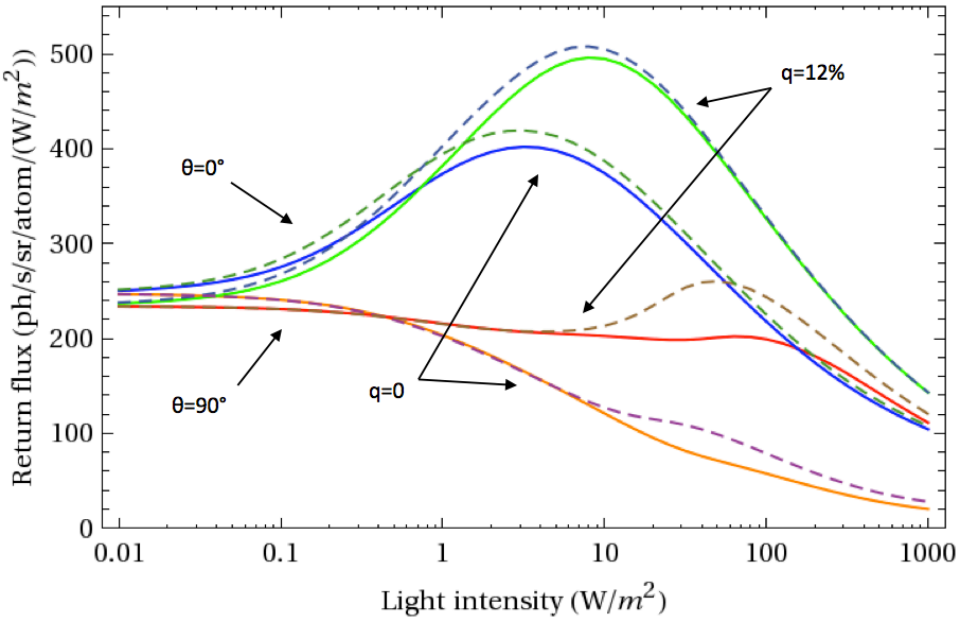

Figure 3.4: Predicted specific return in the mesosphere for a CW, single frequency, circular polarized beam at Mt. Hamilton (solid) and Paranal, Chili (dashed), as a function of irradiance level, both with and without repumping, propagating parallel and perpendicular to the geomagnetic field. This plot shows the strong impact of Earth's magnetic field, and indicates repumping will be beneficial in essentially all cases.

The decline in return at higher irradiance levels is due to saturation, which results in stimulated emission. This happens when a sodium atom in the excited state encounters a laser photon, which causes it to transition back to the ground state by

emitting along the laser propagation direction[§] (i.e. off into space). Because of this, some levels of irradiance can more efficiently couple to the sodium layer, resulting in the peak near ~10 W/m^2 (for repumping, with $q = 12\%$). These peak efficiency levels are the middle ground between having high enough light intensity to trap as many atoms as possible into cycling on the 2-state optical pumping transition, without causing a substantial fraction to undergo stimulated emission.

To verify that ~10% was indeed the optimum portion of laser light to use for repumping, as suggested by Holzlohner et al. (2010), I created the plot in Figure 3.5. This shows return in the mesosphere as a function of repump fraction for irradiance levels of 0.1 W/m^2 (blue), 23.2 W/m^2 (green), 46.4 W/m^2 (gold), and 92.9 W/m^2 (purple). For all but the lowest level (blue line), there is indeed a broad peak centered at 12% repumping. This represents the optimal power allocation for exciting atoms from the D_2b state, while still addressing the stronger D_2a transition group. The parameters used here were for a narrow line, circular polarized, CW LGS pointing to zenith at Mt. Hamilton.

[§] This interesting phenomenon has been central to the development of lasers.

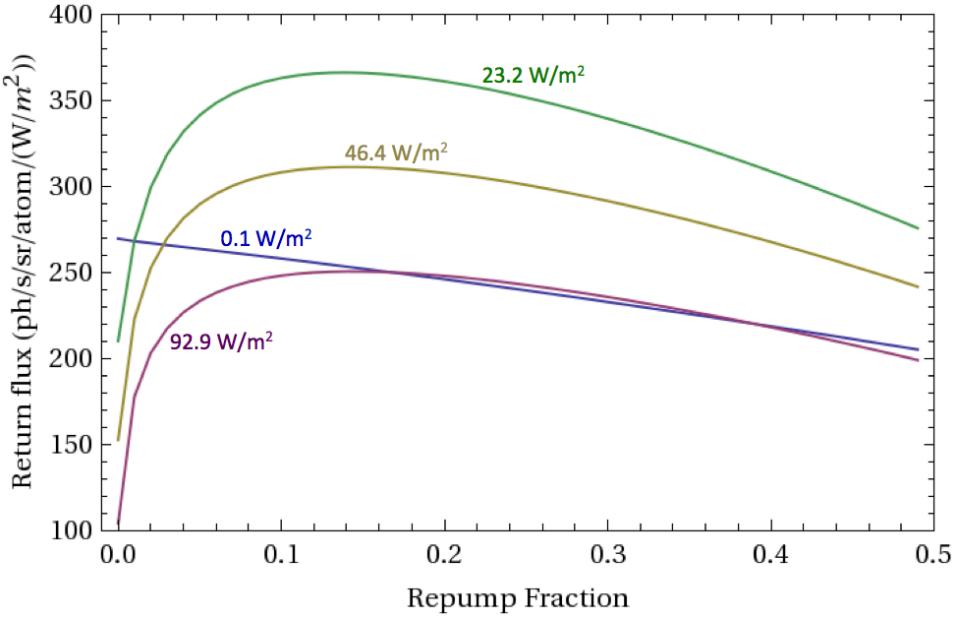

Figure 3.5: Predicted specific return in the mesosphere for irradiance levels ranging from 0.1 W/m^2 (blue) to 92.9 W/m^2 (purple). This confirms that indeed ~10% repumping is optimal.

Three main factors reduce the effectiveness of optical pumping: (1) Larmor precession due to the geomagnetic field, (2) collisions with other constituents of the upper atmosphere, and (3) transition saturation leading to stimulated emission (photons are emitted along the laser propagation direction instead of back towards the telescope). Also important to consider is the slight change in velocity incurred by an atom from absorption and spontaneous emission of a photon (equivalent to a Doppler shift of ~50 kHz, known as atomic recoil), and the transit of atoms in and out of the light beam. At the location of Mt. Hamilton, the strength of the geomagnetic field is 0.47 Gauss at a 90 km altitude, corresponding to a Larmor precession period of ~3.1 μs. The time between collisions is on the order of ~100 μs, and the atoms in the beam are exchanged on a timescale of several milliseconds. Thus, different factors will dominate depending on the duration of the laser pulse.

The quantity of returned photons also depends on the amount of atmospheric absorption, the column density of sodium atoms in the mesosphere, and varies as T_a^{2X}/X, where T_a is the one-way atmospheric transmission at 589 nm at zenith, and $X = 1/\cos(\zeta)$ is the airmass with the zenith angle ζ. The relative direction of the local geomagnetic field with respect to the laser beam has significant impact, and is maximal when the field lines and beam are perpendicular. Hence, highest returns are achieved when the laser propagates parallel to the magnetic field. There is also seasonal variation in the Na column density by a factor of ~3 at North American latitudes, with the high around November and low near May (Gumbel et al. 2007).

To calculate the observed fluorescence, the evolution of the atoms is modeled using the optical Bloch equations for the atomic density matrix, which describes the statistical state of the ensemble of atoms. The evolution of the density matrix, ρ, is given by a generalization of the Schrödinger equation:

$$\frac{d}{dt}\rho = \frac{1}{i\hbar}[H, \rho] + \Lambda(\rho) + \beta. \tag{3.1}$$

The atomic energy level structure and interaction with external fields are described by the total Hamiltonian $H = H_0 + H_E + H_B$, where H_0 is the Hamiltonian of the unperturbed atom, $H_E = -\boldsymbol{d} \cdot \boldsymbol{E}$ is the Hamiltonian of the interaction of the electric dipole of the atom, $\boldsymbol{d}$, with the electric field of the light, $\boldsymbol{E}$, and $H_B = -\boldsymbol{\mu} \cdot \boldsymbol{B}$ which is the Hamiltonian for the interaction of the magnetic moment of the atom, $\boldsymbol{\mu}$, with the local magnetic field, $\boldsymbol{B}$. The square brackets denote the commutator. $\Lambda(\rho)$ represents phenomenological terms added to account for relaxation processes not

described by the Hamiltonian. These include spontaneous decay (omitted from the Hamiltonian due to the semi-classical approximation where atoms are quantum mechanical but light fields are classical), collisional spin relaxation, and the exit of atoms from the light beam due to motion of the atoms and laser. There are also terms in $\Lambda(\rho)$ that describe changes in atomic velocity due to collisions and light-induced recoil, as well as an effective relaxation rate for optical coherences that simulates a laser spectrum with non-negligible bandwidth. Each relaxation process includes a corresponding repopulation process, so that the trace over the density matrix for all velocity groups is conserved, corresponding to conservation of the total number of atoms. These repopulation processes describing the entrance of atoms into the beam are independent of ρ, and so are written as the separate term β.

To account for atoms with different Doppler shifts, the velocity dependence of the density matrix is discretized to describe an appropriate number, $n_{v.g.}$, of velocity groups each with a fixed component of velocity along the laser beam propagation direction. Because coherences between atoms with different velocities can be neglected, the complete density matrix can be thought of as a collection of $n_{v.g.}$ separate, but coupled, density matrices, each of dimension 24 × 24, since there are a total of 24 magnetic substates in the D2 transition. In the online version of LGSBloch, the system is solved using methods built into Mathematica, and the fluorescent photon flux per solid angle emitted in a given direction is found from the steady-state solution as the expectation value of a fluorescence operator (Corney 2006, Holzlöhner et al. 2010a).

To account for a non-uniform irradiance pattern in the mesosphere, LGSBloch makes use of a Gaussian intensity distribution, with user defined FWHM and number of different irradiance levels to include. Based on computational experimentation, results do not change significantly when greater than 5 levels are modeled, so this number is used throughout this work. In calculating the return at the telescope, the fluorescing atoms are assumed to be at the median altitude of the Na layer near 92 km.

3.3 Optimization of pulse format

Pulsed sodium LGS are useful because they allow for Rayleigh blanking and fratricide avoidance in multiple LGS systems. The first ~30 km of atmosphere strongly scatter light back towards the telescope (this is known as Rayleigh scattering), disrupting measurement of the wavefront from the higher altitude sodium beacon. Rayleigh blanking involves blocking light from entering the WFS during the time the pulse is traveling through this region of air. Fratricide refers to the Rayleigh backscattered light from one LGS entering the WFS of another, in systems that contain multiple lasers, and can be reduced with similar time-gating schemes. These background and spot elongation mitigating techniques reduce the WFS measurement error, and thus result in increased AO system performance.

Until recently, the available laser technology at wavelengths of 589 nm relied heavily on the high peak power in short pulsed systems to achieve acceptable power conversion efficiency levels. As new technologies emerge with greater flexibility

available in the temporal format, understanding the costs and benefits of the different options becomes crucial.

My efforts to determine the optimal pulse duration began with examining how the number of spontaneously emitted photons varies as a function of time. Figure 3.6 shows results from two 100 μs simulations for zenith pointing at Mt. Hamilton, with the irradiance levels set to be equal to what is present for 10 W average launched power operating at a 20% duty cycle. On the left, all the light is on the D_2a transition, and the right plot is for ~10% of the light tuned to D_2b. For both cases there is an initial enhancement in the specific return (i.e. photons/s/sr/atom/(W/m^2) in the mesosphere, a measure of local return flux per laser irradiance[3]). However, in the case of no repumping, the decline begins sooner for all but the lowest irradiance levels, and the peaks are considerably lower. These results suggest that for 10 W average launched power and 20% duty cycle, the most efficient use of the sodium atoms will be with repumping and pulse durations between 10 – 30 μs. However, if partitioning of the laser light to include the D_2b line is not possible due to engineering constraints, somewhat shorter pulses will be better suited to take advantage of the initial return enhancement.

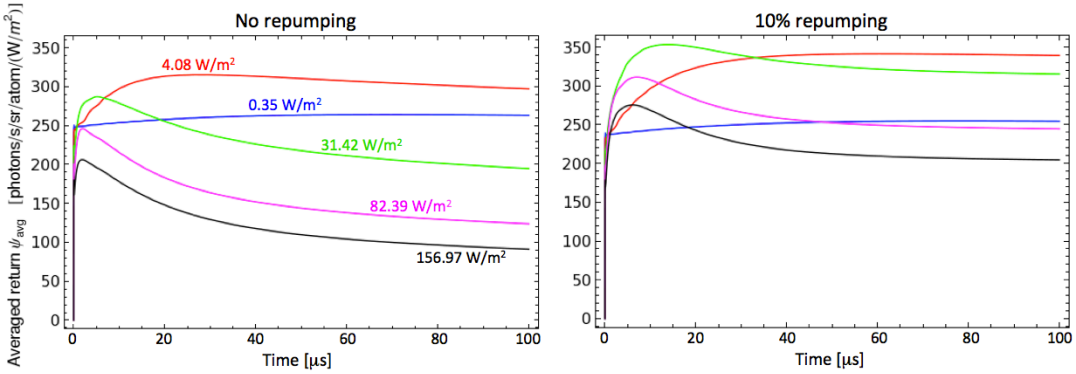

Figure 3.6: These 100 μs simulations show time evolution of specific return flux for the different levels of irradiance present for 10 Watts launched power with 20% duty cycle. When no light is resonant with the D_2b line (left plot), the return peaks and declines quickly. When 10% of the laser power is tuned to D_2b, the return peaks later, is higher, and decreases less rapidly (right plot). These graphs also indicate that certain values of irradiance excite the Na atoms more efficiently, as discussed in the previous section.

It was hypothesized that the decline after the peak was possibly in part due to the effects of Larmor precession, since this acts on timescales of a few microseconds. To test this, these simulations were repeated with zero magnetic field. The results showed a lessening in the severity of the decline, and the expected increase in return, but the peak remained prominent. This leads to the conclusion that other factors may be of greater importance than the Larmor precession, such as the rate of collisions between the sodium atoms and other constituents of the mesosphere. This will be investigated further in Section 5.3.

Another interesting observation from Figure 3.6 is that certain irradiance levels are more efficient at optical pumping than others. This is also observable in Figure 3.4, for the circular polarized CW case. In the right pane of Figure 3.6 (for 10% repumping) the green line corresponding to 31.42 W/m^2 achieves the highest specific return. The possibility of taking advantage of this circumstance by

controlling the irradiance profile using uplink correction will be discussed further in Section 3.5.

Beyond the considerations of how to most effectively excite the sparse Na atoms during a single pulse, is the question of what pulse formats allow for the benefits of optical pumping between consecutive pulses. Stated differently, what is the length of time necessary for atomic polarizations to return to thermal equilibrium? Based on results of various simulations I performed to test this, the time scale appears to be ~50 μs near the center of the sodium layer. Hence, a format with less than this amount of dark time between pulses should be modeled with multiple cycles of the laser, while pulses with larger spacing may be considered independent, i.e., modeling a single pulse will give a sufficiently accurate estimate.

Figure 3.7 shows a 10 pulse train for pulses of 500 ns, with 10% repumping and a 20% duty cycle. The pumping between pulses is evident, and notably the different irradiance levels (which are the same as in Figure 3.6) evolve differently as a function of time. The extremal levels (maximum and minimum) remain fairly constant from pulse to pulse, while the median irradiances (green and magenta) dominate after just a few cycles.

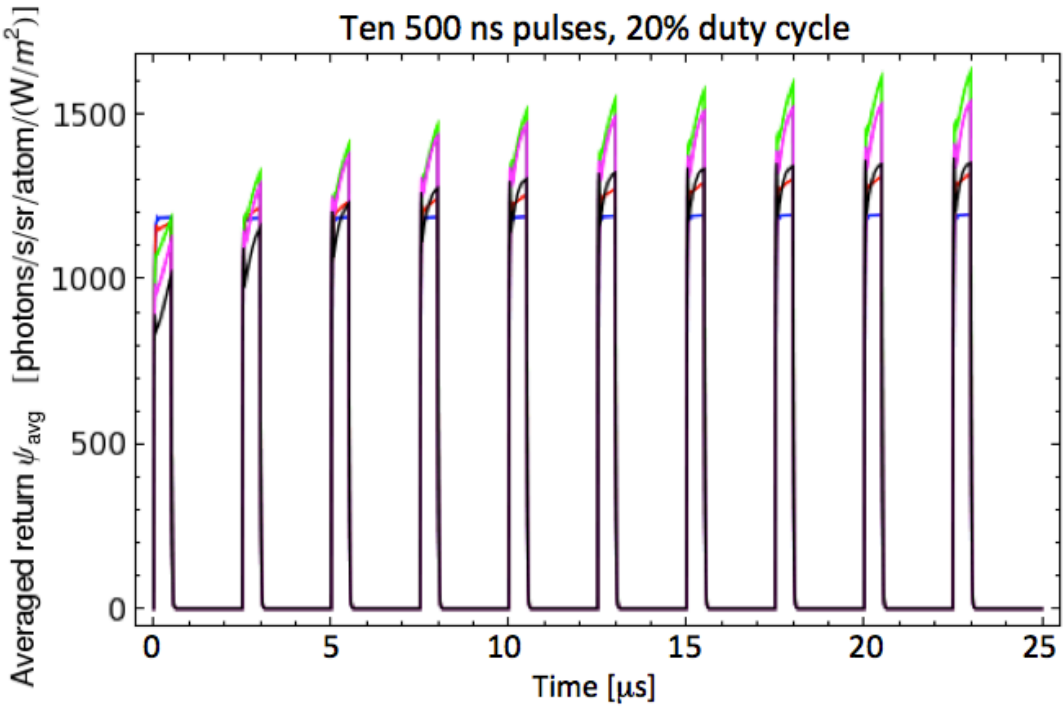

Figure 3.7: This intermediate pulse format shows the presence of optical pumping between pulses. The irradiance levels and colors are the same as in Figure 3.6. Again, some levels are more effective than others in this process.

To discover the optimal pulse duration, simulations were carried out for pulses ranging from 200 ns to 60 μs, with 10% repumping, both 10% and 20% duty cycles, for zenith pointing at Mt. Hamilton. In all cases, the 20% duty cycle gave higher return, and the maximum was for the 30 μs pulses. The predicted flux at the top of the telescope for this format is 12×10^6 photons/s/m^2, assuming a sodium column density of 4×10^{13} atoms/m^2 and 0.5 m FWHM mesospheric spot size. This value is based on simulation of 3 cycles of the laser, although it is the same value obtained for only one cycle. At a pulse length of 60 μs, and the same duty cycle, the time-averaged return flux declined to 11.3×10^6 photons/s/m^2. For the 200 ns, case (the LLNL fiber laser is currently operating with this pulse length but at 10% duty cycle)

the predicted return flux is 11.4×10^6 photons/s/m^2, based on a simulation of 50 cycles. This information is displayed in Table 3.1. For comparison, a 10 Watt CW laser with otherwise identical parameters (repump fraction, location and pointing) is expected to produce 13×10^6 photons/s/m^2.

Pulse length (μs)	Return at 10% duty cycle ($\times 10^6$ photons/s/m^2)	Return at 20% duty cycle ($\times 10^6$ photons/s/m^2)
0.2	9.5	11.4
30	10.5	12.0
60	10.2	11.3

Table 3.1: Comparison of the return flux from pulse lengths of 200 ns, 30 μs, and 60 μs, for both 10% and 20% duty cycles. This predicts the maximal return will be from the 30 μs pulses with 20% duty cycle format.

This investigation established the 30 μs pulses with 20% duty cycle as part of the goal format we intend to implement on the fiber laser, since it has the highest predicted return and will also facilitate Raleigh blanking. Figure 3.8 contains a time vs. altitude diagram showing how Raleigh blanking can be realized with this pulse format, while having two light pulses in the air at once. The 30 μs pulse length corresponds to a distance of 9 km in air, so it will essentially span the entire sodium layer. This blanking technique will reduce the amount of Raleigh backscattered light from the first ~20 km of atmosphere that enters the WFS, resulting in greater measurement signal-to-noise and increased overall performance of the AO system.

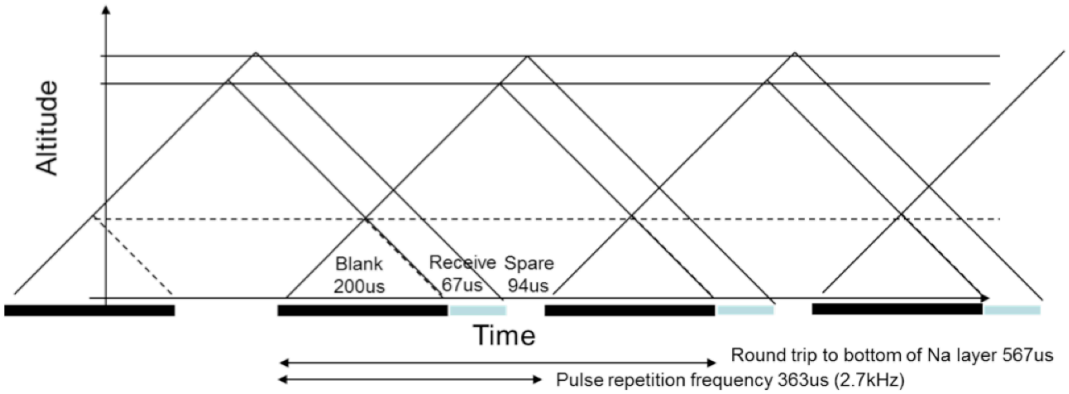

Figure 3.8: This time vs. altitude diagram demonstrates a Raleigh blanking scheme with two 30 μs pulses in the air simultaneously.

These simulation results indicate the optimal format for the new fiber laser should include both 10% repumping and extension of the duty cycle to 20%. If increasing the duty cycle proves infeasible because of engineering issues, then for 10% duty cycle and all other parameters the same the 200 ns pulses are predicted to return 9.5×10^6 photons/s/m^2, and the 30 μs pulses 10.1×10^6 photons/s/m^2. However, increasing the duty cycle is currently viewed as higher priority than extending the duration of the pulses, based on the greater photon returns predicted for even the 200 ns pulse case.

From 2006 to 2010, the average measured return flux from the current dye laser on the Shane telescope was 1.16×10^6 photons/s/m^2, for an average launched power of 9 Watts. Based on modeling the return of the new fiber laser, it seems reasonable to assume this system will achieve somewhere between 5 – 10 times the current LGS brightness.

3.4 Spectral format options: Narrow line, multimode, or broadband?

Thus far there has been no discussion of the spectral format options beyond simply addressing the two D_2 transitions. The return flux predictions in the previous section have been for narrow (<10 MHz) line widths. The spectrum of the LLNL fiber laser currently contains multiple lines (modes) spaced at 200 MHz intervals. This multimode format was implemented to mitigate stimulated Brillouin effects (SBS) in the fiber amplifiers. From the standpoint of effective coupling to the Na atoms, such a spectrum is generally less desirable than having the light confined within two lines that are tuned precisely to the D_2a and D_2b transitions. Also, the problem of accurately modeling a system with many discrete frequency components using Bloch equations becomes very complex. Hence, the numbers presented in the previous section should be considered optimistic upper limits on what will actually be achievable with this laser in real on-sky conditions.

There is some flexibility in the fiber laser system as to the number of modes and how far apart they are spaced, and the option exists to convert to a broadband format instead. Because the online version of LGSBloch does not have the capability to do multimode time domain calculations, a consulting contract was established with Rochester Scientific to investigate the effects of such changes on the return flux (along with topics discussed in the next chapter).

Rochester Scientific developed a proprietary extension of the LGSBloch simulation package, where solutions to the density matrix evolution equations are

generated with a code written in C that uses an open-source ODE solver (Rochester et al. 2012). This method addresses the stiffness of the system using implicit backward differentiation formulas (Hindmarsh et al. 2005), and significantly decreases the time required for convergence to a solution. Techniques to account for the atoms being subjected to a field with components oscillating at different frequencies have also been included. For the case of coherent modes, this is equivalent to a single field (with a frequency equal to that of the central mode), amplitude modulated with the modulation frequency equal to the mode separation. The width of each mode is accounted for by including additional relaxation terms in the atomic optical coherences.

The two plots in Figure 3.9 compare the number of emitted photons for the cases of a narrow single mode (red), a broadband spectrum with 500 MHz FWHM (blue), and three coherent modes separated by 150 MHz (orange). These simulations assumed no magnetic field (or equivalently, propagation parallel to it) and no repumping. Irradiance levels present in a Gaussian beam profile have been integrated over to produce the bottom graph. These graphs reveal that the optimal format is a function of the laser power, and the corresponding levels of light intensity produced in the mesosphere. A discussion of beam profiles and irradiance distributions can be found in Chapter 4.

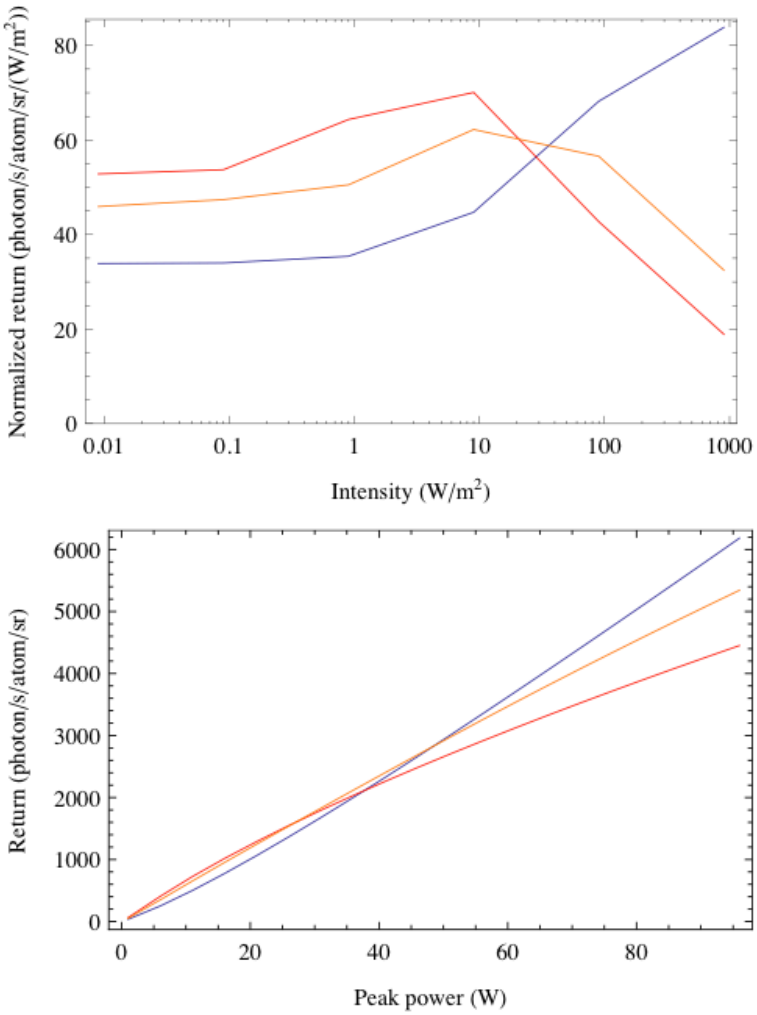

Figure 3.9: The top graph shows the specific return in the mesosphere as a function of the light intensity for a single narrow line (red), a broadband spectrum with 500 MHz FWHM (blue), and 3 narrow lines with 150 MHz spacing (orange). In the bottom plot, integration over the beam profile has been performed. This is for no repumping and no magnetic field. These graphs reveal that the optimal format depends on the laser power.

Hillman et al. (2006) hypothesized that 150 MHz would be the mode separation to give maximal returns, based on considerations of the fine-structure splitting of energy levels in the sodium atom. To investigate this, I requested that Rochester Scientific produce a simulation for a three-mode system, with the central frequency tuned to the center of the D_2a line and side bands with separations ranging

from 0 to 500 MHz. The parameters used were for a 10 W laser at Mt. Hamilton with 30 μs pulses, 20% duty cycle, and no repumping (i.e. the goal format for the LLNL fiber laser). The orange curves in Figure 3.10 show how the specific return in the mesosphere varies with mode separation, when propagating parallel (top) and perpendicular (bottom) to the geomagnetic field. The blue curves show the changes in return for a broadband laser spectrum, with line width ranging between 0 and 500 MHz.

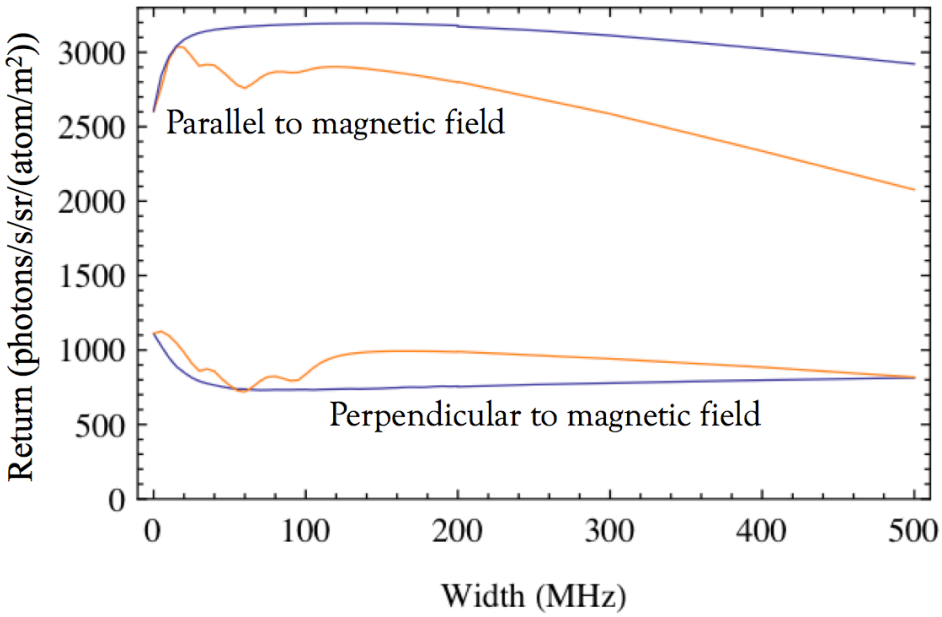

Figure 3.10: Return from a LGS that is multimode as a function of mode separation (orange) and broadband (blue) as a function of bandwidth, for parallel (top lines) and perpendicular (bottom) to the magnetic field. This indicates different formats may be optimal at different locations depending on the relative direction of the magnetic field during the majority of observations.

The structure observed in the multimode case can be understood in terms of the atomic physics of sodium. The local minimum at ~60 MHz is a consequence of the 59.8 MHz separation between the $F' = 2$ and $F' = 3$ excited states. Here, the central frequency of the laser is exciting the $F = 2$ to $F' = 3$ transition, but the side

bands are now tuned to the $F = 2$ to $F' = 2$ transition for the same velocity group. But atoms in the $F' = 2$ excited state can decay to the $F = 1$ ground state where they are no longer resonant with the light field. This is referred to as downpumping, where the loss of atoms available to be optically pumped naturally leads to fewer emitted photons.

The dips in return near ~30 and ~90 MHz can be understood similarly. When the sidebands are 30 MHz from the central frequency, atoms in a velocity group resonant with the $F = 2$ to $F' = 3$ transition for one sideband will have the other sideband encouraging the $F = 2$ to $F' = 2$ transition. At a 95.3 MHz separation of the modes, the sidebands can cause transitions from the $F = 2$ to $F' = 1$ excited state, which will also lead to increased downpumping. The decline in return at larger separations is attributed to the presence of fewer atoms available to interact with the light field near the edges of the Doppler broadened spectrum.

Figure 3.10 confirms that the ideal line separation in a multimode LGS is either small (less than ~20 MHz) or between about 120 to 150 MHz, depending on the orientation to Earth's magnetic field. This also holds implications for what will be the most effective use of laser power depending on the location of the observatory. Near the equator, a laser will spend the majority of time propagating perpendicular (or nearly so) to the geomagnetic field. In contrast, at more polar latitudes, zenith propagation will be much closer to parallel to the field lines. Figure 3.10 suggests that a broadband LGS (with FWHM between about 50 and 150 MHz) should be the

brightest for polar observatories, and an equatorial location may benefit most from a multimode spectrum (with mode separations of ~150 MHz).

3.5 Potential benefits of uplink correction

These simulations also enable investigation of the possible benefits of uplink control, a technique in which the laser light is reflected off a deformable mirror prior to projection into the atmosphere. This allows manipulation of the wavefront in order to compensate for imperfections in beam shape and projection optics, and aberrations induced by atmospheric turbulence. The potential benefits include obtaining a smaller spot to decrease WFS measurement error, and potentially regulating the pattern of irradiance in the mesosphere to maximize efficiency of optical pumping.

Wavefront error depends on guide star spot intensity distribution according to

$$\sigma_{SNR} = \chi d \frac{\iint f(x,y)dxdy}{2\int f(0,y)dy} \times \frac{1}{SNR} \tag{3.2}$$

where χ is a factor that accounts for AO control loop averaging, d is the Hartmann subaperture size, and SNR is the signal-to-noise ratio on the detector (Gavel et al. 1998). The function $f(x,y)$ is the distribution of light on the detector (with x and y given in units of angle on the sky) and the integration is from $-\infty$ to $+\infty$, so the ratio of integrals is a measure of the spot size. This shows that the measurement error depends linearly on the spot size factor and inversely on the guide star brightness, which is a determining factor in the signal-to-noise ratio (SNR).

In Figure 3.11, return flux at the top of the telescope is plotted against Fried's

parameter, r_0, which is equivalent to varying spot sizes in the mesosphere. These simulations are for a 10 Watt CW zenith pointing laser operating at Mt. Hamilton, with a launched beam of 20 cm diameter. Since the return is greater for larger spots (smaller r_0), the implication is that uplink control could be used to optimize between brightness and reducing WFS error, which declines as the square of the spot size (Gavel et al. 1998). For the range of parameters used in the figure, the main cause of increased brightness for a larger beam is the availability of more atoms, due to the spots larger area.

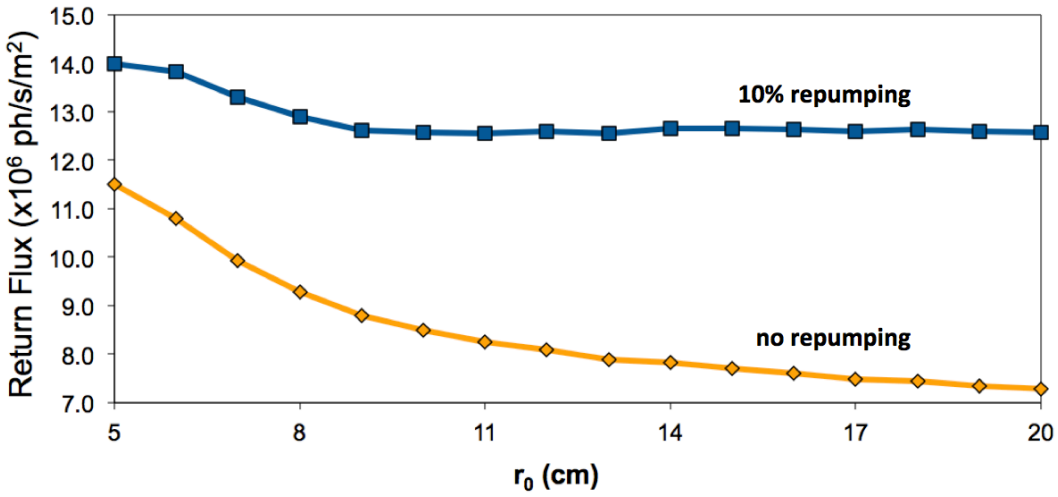

Figure 3.11: The return slightly increases in poor seeing conditions (i.e. small r_0) due to the larger spot size produced in the mesosphere, allowing more atoms to interact with the light. This effect is less substantial when using repumping. Uplink control could optimize between this enhancement and the reduction in WFS centroiding accuracy with a larger spot.

Further benefits of repumping are also seen in Figure 3.11, with the decline in return for smaller spots (larger r_0) leveling off. This is an indication that the atoms in the beam are being used efficiently, even as their number starts to decline and the light intensity levels increase. Without repumping, as the irradiance increases and atoms cycle more quickly between the ground and excited states the rate of

downpumping also increases, with the results that over time even fewer atoms are available to interact with the light field.

In consulting with Rochester Scientific, the issue of quantifying the benefits of uplink control was revisited. We investigated using these techniques to manipulate the irradiance profile as well as the spot size, in order to maximize the area in the mesosphere irradiated at levels that lead to the most efficient fluorescence (as mentioned in Sections 3.2 and 3.3). This involved modeling a beam profile with the shape of a top hat, and comparing it to the Gaussian profiles used for all modeling results thus far (how well these correspond to realistic beam profiles is discussed in Chapters 4 and 5).

In Figure 3.12, two curves compare the predicted return flux of both Gaussian and top hat shaped mesospheric illumination profiles. These were generated for a laser that produces 10 W average power, located at Mt. Hamilton, operating at 20% duty cycle with 30 μs pulses, 3 modes spaced by 150 MHz, 10% of the power in a sideband tuned to D_2b, and another 10% lost in the sideband on the far side of the spectrum (this is necessary as a consequence of laser engineering frequency modulation limitations). The obvious conclusion is that there is only a small enhancement over the Gaussian beam when the irradiance profile is made to approach a constant value. However, full interpretation of this graph requires understanding how the shape of the beam in the mesosphere gets translated into a spot size on the WFS detector. This is a topic discussed in Chapter 5.

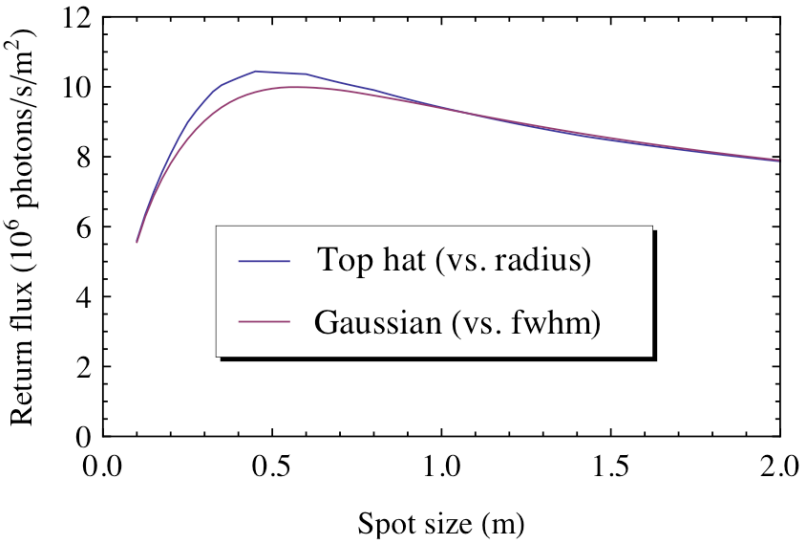

Figure 3.12: The return flux improves slightly with the top hat shaped irradiance profile. However, the largest benefits will come from the reduction in WFS measurement error associated with a smaller spot size.

The current estimate of the spot size of the LGS on the Shane telescope is ~2 arcseconds, which means it appears to be ~1 m diameter at the distance of the mesosphere (90 km). Assuming that there are approximately equal amounts of spot broadening from atmospheric turbulence as the light travels back to the telescope as for its trip upward, then the actual physical size of the laser beam in the mesosphere is ~0.6 m. If uplink control could be used to reduce this by a factor of two to a nearly diffraction limited spot, even with the decreased return as indicated in Figure 3.12, the WFS measurement error would be reduced by a factor of two. Such benefits seem worth the additional complexity of an uplink system, but more work needs to be done in order to make a complete assessment. Some specific areas that should be addressed are mentioned in Chapter 5.

3.6 Discussion

The current LGS in use on the Shane Telescope at Lick Observatory is a tuned dye laser that was constructed at LLNL and installed in 1995. The average measured output power between 2006 and 2010 was 9 Watts. The light is linearly polarized, and contains pulses of 150 ns in duration with a repetition frequency of 11 kHz. The beam is centered on the D_2a line and electro-optically phase modulated to broaden it to ~2 GHz line width. This broadening was implemented to address all atoms in the Doppler broadened absorption profile, and to reduce saturation effects due to the high peak power during the pulses. Measurements show this laser gives the equivalent of about a 10th magnitude natural guidestar, which is adequate to run the AO system with its present 43 cm diameter subapertures for $\lambda = 2.0$ μm science observing (Gavel et al. 1998).

Much has been learned since this laser was installed, both in terms of laser technology and understanding the coupling of laser light to the Na atoms in the mesosphere. In particular, demonstrations of narrow band CW sodium LGS have shown a much greater number of returned photons per watt than has ever been produced by the modulated dye lasers (Denman et al. 2006). Increasing the return signal will enable use of smaller subapertures, so AO correction can be applied at shorter science wavelengths.

Recently, LLNL has been involved in developing fiber laser technology for LGS. They have demonstrated a solid state 589 nm system with 10 Watts average output power in the laboratory (Dawson et al. 2006). The system uses non-linear

combining of two high-power infrared lasers at 938 nm and 1538 nm to produce the 589 nm line, and has tunable temporal and spectral characteristics. Table 3.2 gives the parameters of both lasers and shows the current laboratory tested versus target formats for the fiber laser system.

	Current dye laser	**New fiber laser**	
		Lab tested format	*Goal format*
Output power	9 W	10 W	10 W
Polarization	Linear	Circular	Circular
Spectral format	~2 GHz FWHM bandwidth	9 lines with 200 MHz spacing	Fewer lines and/or smaller spacing
Pulse duration	150 ns	200 ns	30 μs
Duty cycle	0.16 %	10 %	20 %
Fraction of light tuned to D2b	None	None	10%

Table 3.2: Comparison of parameters between the current LGS, the laboratory tested format of the new fiber laser, and the goal format.

The goal format presented in Table 3.2 takes into account the lessons learned from the inquiries discussed in this chapter. The best estimate of the number of returned photons expected with the stated parameters can be deduced from Figure 3.12. Assuming a roughly Gaussian spot that has ~0.6 m FWHM, approximately 10×10^6 photons/s/m^2 should reach the top of the telescope. This is somewhat less that the 12×10^6 photons/s/m^2 predicted in section 3.2, but the difference can be understood as a consequence of the more realistic spectral format used here. Given this improved estimate, it still appears reasonable to expect the fiber laser to produce 5 – 10 times the return seen from the current LGS.

Numerical models have made it possible to investigate the effects of different parameters involved in LGS creation. This allows optimization of the format and estimation of the photon return prior to installing a laser on a telescope. This tool has determined some important basic guidelines as to the most efficient way to couple the laser light to the sodium atoms. In general, the optimal format will include narrow bandwidth, circularly polarized light, with ~10% of the power tuned to the D_2b transition.

These simulations have also shown that photon returns close to those from CW lasers can be achieved with long pulse formats. Pulses enable Raleigh blacking and fratricide avoidance strategies to be implemented. The investigation thus far has focused on results for a 10 W laser operating with 10% and 20% duty cycles, and pulse durations ranging from 200 ns to 60 μs. For the case of 10% repumping, the 20% duty cycle pulses result in ~20% greater return and have a slight maximum at about 30 μs in duration. This maximal value is within 10% of what is expected from a 10 Watt CW laser operating in the same conditions.

Longer duty cycles were also investigated for this laser, keeping all other parameters equivalent to those presented in Section 3.3. Three pulse cycles were simulated for the cases of 50% and 75% duty cycles, resulting in predicted returns of 12.5 and 12.9 × 10^6 photons/s/m^2, respectively, which are clearly asymptoting to the predicted CW return value.

Optimization of the spectral format is found to be dependent upon both the instantaneous power levels present in the beam when it encounters the sodium atoms

(Figure 3.9), and what will be the most common orientation of the laser beam with respect to the geomagnetic field (Figure 3.10). Table 3.3 gives the latitudes, longitudes, magnetic field direction and strength at an altitude of 90 km, for some of the major observatories around the world. The range of these parameters makes it important to understand what effects will dominate at the different locations.

	Latitude (Degrees)	Longitude (Degrees)	Declination (Degrees)	Inclination (Degrees)	Total Field (Gauss)
Mt. Hamilton, Ca	37.30	-121.84	13.60 East	61.02 down	0.465
Starfire Optical Range, NM	34.96	-106.46	8.77 East	62.12 down	0.476
Mauna Kea, Hawaii	19.82	-155.47	9.70 East	36.27 down	0.334
Canary Islands, Spain	28.76	-17.88	-6.33 West	38.22 down	0.371
Paranal, Chile	-24.67	-70.42	-2.07 West	-22.58 up	0.225
Mt. Stromlo, Australia	-35.32	150.04	12.57 East	-65.77 up	0.555

Table 3.3: The strength and direction of Earth's magnetic field at an altitude of 90 km, for the locations of several large observatories. Data are from the IGRF 11 model, calculated by the National Geophysical Data Center website for February 2013. These changing environmental conditions necessitate understanding the behavior of LGS for a wide range of parameters.

Chapter 4

Modeling Current Laser Guide Stars at the Lick and Keck Observatories

4.1 Introduction

The LGSBloch simulation package has been shown to provide reasonable measurement predictions from CW LGS (Holzlohner et al. 2010b), but comparisons to pulsed systems have only been published within the past year (Holzlohner et al. 2012, Rampy et al. 2012). An early endeavor of my research on understanding LGS was to obtain measurement data from the LGS at Lick observatory and compare it to predictions of the model. When a discrepancy was found between the data and model, a more detailed assessment of how both values were calculated was pursued. As the issue persisted, I moved on to modeling the similar LGS systems at the Keck Observatory and compared the predictions with return flux measurements reported in the literature. A similar discrepancy was found for these cases. Holzlohner et al. (2012) reported an identical level of disparity for modeling of the LGS on the Gemini South telescope.

All of these systems have short pulse formats, small duty cycles, and broadened spectra. A parameter this bestows upon them in common is high instantaneous power levels during a pulse. This and several other factors are

investigated in this chapter as the underlying reason for the current discrepancy between predictions generated with LGSBloch and the actual measured return fluxes.

The next section describes my simulation of the number of photons expected to be incident at the top of the telescope for the 50 W Fasortronics laser at SOR, the 10 W dye laser on the Shane telescope, and the two ~15 W LGS at the Keck observatory. Section 4.3 discusses efforts to find the source of the discrepancy by incorporating a more realistic level of detail in the model. This included collaboration with Rochester Scientific on some topics, and physical optics modeling in IDL to better understand the effects of the turbulent atmosphere on the beam profile in the mesosphere. The final section summarizes what has been determined and motivates the discussion of where future efforts should focus, which will be presented in Chapter 5.

4.2 Simulation predictions overestimate return flux data from short pulse Laser Guide Stars

As stated in the previous section, the LGSBloch model is reported to predict return fluxes in good agreement with measurements for the case of the single frequency 50 W Fasortronics laser at SOR. This requires assuming slightly higher than average, but still reasonable, values for unknown quantities involved in the calculation, such as the mesospheric sodium column density, C_{Na}. Because the return flux at the telescope scales linearly with C_{Na}, this parameter is a useful gauge in determining how accurately a numerical model reproduces real systems. Results of Lidar measurements indicate the expected median annual density is $3 - 4 \times 10^{13}$

atoms/m^2, although sporadic layers may have concentrations up to 10 times greater (Xiong et al. 2003, Moussaoui et al. 2010).

To verify the agreement between the code and SOR data, I used measurements of the circular polarized beam reported by Denman et al. (2006), and adjusted the value of C_{Na} in the model until it matched the data. Figure 4.1 shows measurements taken at different times throughout the year, for both linear and circular polarized light (data points and black lines). The red dashed lines indicate the minimum and maximum values in the seasonal variation that I used for comparison to the model. The numbers on the far right show what C_{Na} had to be assumed to fit these measurements. Although these values are larger than the expected 3 – 4 × 10^{13} atoms/m^2 seasonal average, they are fairly consistent with what has been reported for this site (Drummond et al. 2007), and the values used in the comparison by Holzlohner et al. (2010b). As is discussed in many studies, the sodium layer is highly variable (Neichel et al. 2013).

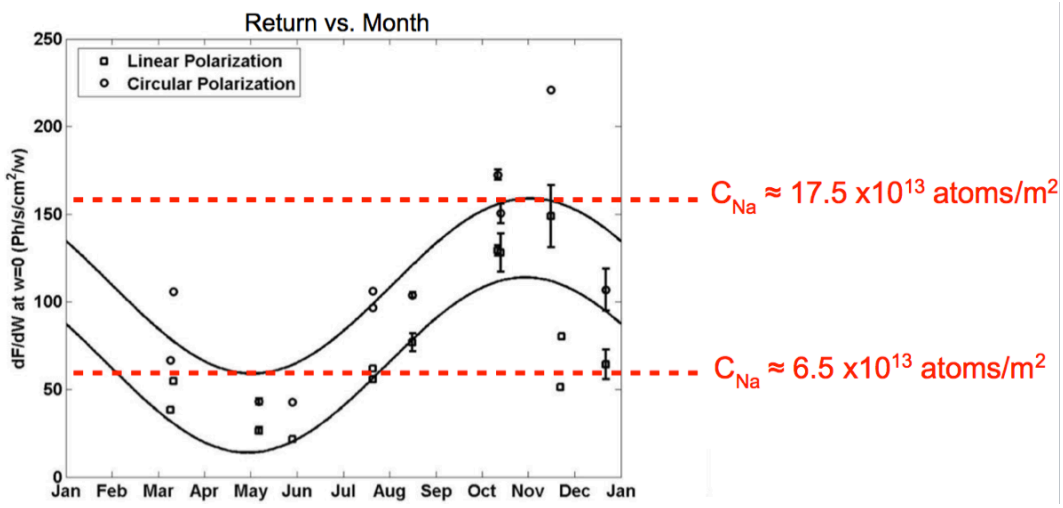

Figure 4.1: Fit to data from the 50 W Fasortronics laser at SOR (Denman et al. 2006), assuming zenith pointing and a 0.76 m FWHM spot. The inferred sodium abundance is somewhat higher than expected but still within an acceptable range.

The parameters of the current LGS on the Shane telescope at Mt. Hamilton are given in Chapter 3 in Table 3.1. Because of the long dark time between pulses (~91 μs), my modeling endeavors only included one cycle of the laser (this simulation still took several days to complete, running on the LAO's HP 24-core Intel® Xeon® Processor machine called Lightwave). My modeling assumed a Gaussian spot size of 0.6 m FWHM in the mesosphere, a Gaussian shaped spectrum with 2.2 GHz FWHM bandwidth, and a Gaussian pulse shape with 150 ns FWHM. Figure 4.2 shows a trace of the pulse profile from the instruments at Mt. Hamilton, and it is indeed very closely Gaussian.

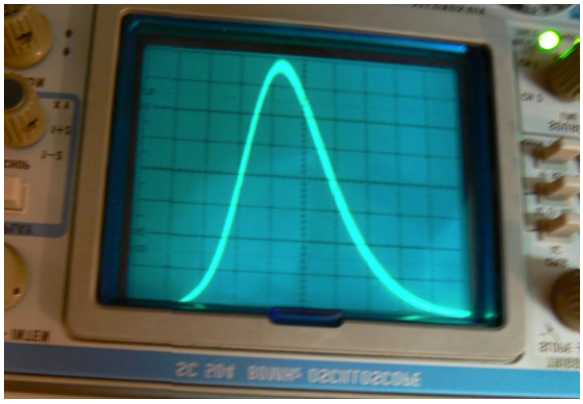

Figure 4.2: This trace shows the pulse shape of the dye laser currently operating on the Shane telescope at Mt. Hamilton. It is very close to a Gaussian with 150 ns FWHM.

In Figure 4.3, measurement data from this laser taken between 2006 and 2010 are plotted as a function of month. They show strong evidence for the seasonal variation of the sodium layer. I again used the C_{Na} as a gauge to how well the measurements were reproduced with LGSBloch. The right-hand axis exhibits the

implied amount of C_{Na} based on the present stage of modeling. For the seasonal average corresponding to a return flux of 1.16×10^6 photons/s/m^2 at the top of the telescope, the C_{Na} is found to be only 1.5×10^{13} atoms/m^2. This small value is interpreted as an indication that the simulations are over-predicting the measurements for this laser by at least a factor of two. Thus, the conclusion is that some physical, environmental, or observational parameters are not being accounted for adequately.

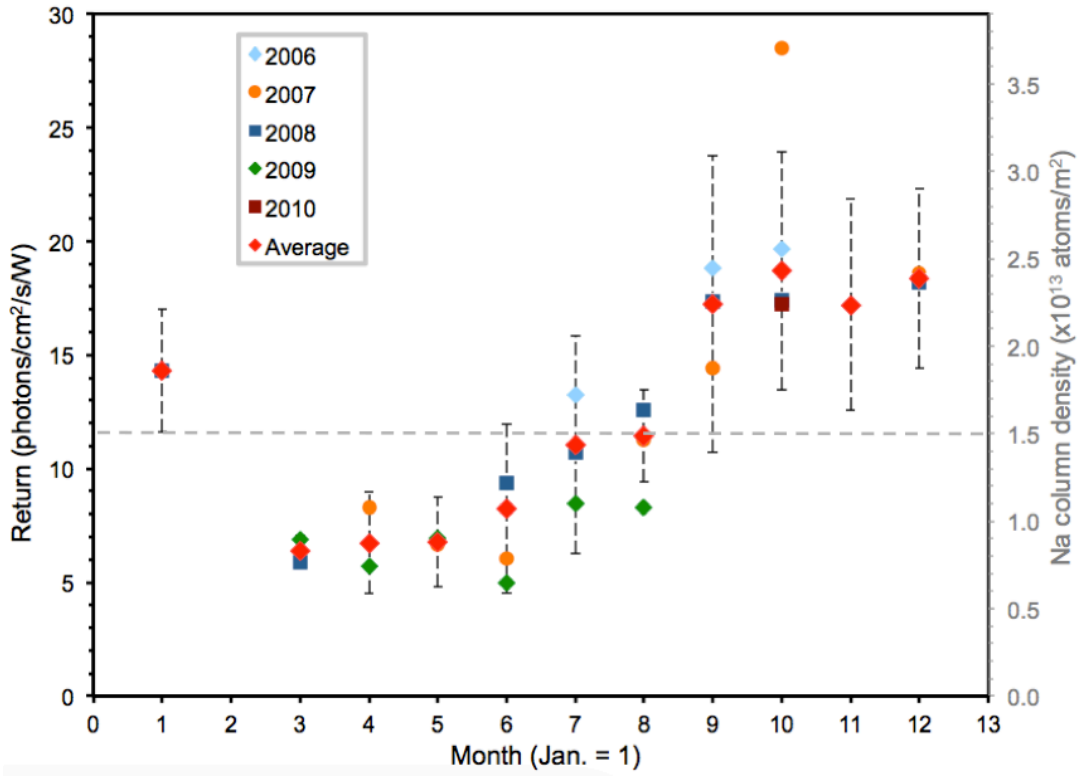

Figure 4.3: Data from the dye laser on the Shane telescope show the expected seasonal variability. The right axis shows the implied $\boldsymbol{C_{Na}}$ based on the present level of modeling with LGSBloch. The horizontal dashed line indicates the predicted average column density based on the measured average return of 11.6 photons/cm^2/s/W. These $\boldsymbol{C_{Na}}$ are considerably lower than expected, implying the need for simulation with greater detail.

The return flux measurements from the Shane LGS are based on data collected with the Shack-Hartman WFS, for zenith pointing observations. The intensity in the fully illuminated subapatures was averaged, and I corrected for 40%

throughput. The camera gain is reported to be ~1 electron/count. In 2004, Donald Gavel (private communication) used a handheld power meter with 633 nm wavelength light to measure throughput of the AO system from the primary focus of the telescope to the WFS, which he found to be 55%. In January 2012, observations of several Hayes spectrophotometric standard stars were taken by the observatory staff to re-asses this value. A sodium filter with 0.87 nm FWHM bandpass was used, and resulting flux measurements were corrected for atmospheric transmission and compared with online spectra[††]. This analysis returned an average throughput of 40%, which is consistent with the 2004 measurement when considering the amount of light lost to the primary and secondary mirror surfaces and optics internal to the WFS.

After these investigations to ensure the measurement data were being interpreted correctly, I varied some of the less precisely determinable simulation inputs to see how sensitive the predictions were to these assumptions. Making adjustments to parameters such as spot size, bandwidth, and atmospheric transmission, I was able to somewhat ameliorate the disagreement, but only marginally.

For example, the original estimate of return for the Shane laser was reduced 20% by changing the modeled spot size from 0.7 m to 0.6 m FWHM, and increasing the bandwidth from 1.5 GHz (the original target width for the spectrum) to 2.2 GHz FWHM (closer to the measured value). However, the same reduction also occurred

[††] http://www.eso.org/sci/observing/tools/standards/spectra/stanlis.html

when increasing the spot size to 1.0 m FWHM, setting the bandwidth to 2.2 GHz, and decreasing the atmospheric transmission to 85% (the default value is 89%). This is strong evidence for the need to better constrain such variables, as will be discussed further in the Chapter 5.

To help identify whether the source of the discrepancy was related to the measurement data or the model, I also simulated the two LGS at the Keck observatory. The Keck II system began science operations in 2004 (Wizinowich et al. 2006), and has been responsible for ~70% of the refereed science papers published worldwide through 2012 based on data collected with LGS AO systems. The success of this system led to the desire for similar capabilities on the Keck I telescope. This has been recently realized, with the Keck I LGS AO system having begun full science operations in the latter part of 2012 (Chin et al. 2012).

The laser on Keck II is the same technology as the dye laser at the Lick observatory and has essentially the same format, except that it operates with a repetition rate of 26 kHz (the Shane laser is at 11 kHz). The ~38 μs dark time between pulses in the Keck II laser is near the critical timescale where the sodium atom excitation levels accumulate from pulse to pulse, hence a single pulse and a train of 5 pulses were modeled and compared. The return from the 5 pulse simulation was only ~8% less than for the single. This small change reinforces the earlier conclusion that the rethermalization time is near 50 μs. A Gaussian spot size of 0.7 m FWHM in the mesosphere was assumed, and parameters based on location, such as

observatory altitude, magnetic field direction and strength, were included in the model.

Figure 4.4 shows the five pulse train modeled with LGSBloch, where the different colors correspond to the five different irradiance levels used (blue is the lowest, black the highest). Only a slight amount of evolution is evident between pulses in the specific return (in the mesosphere) for the different levels.

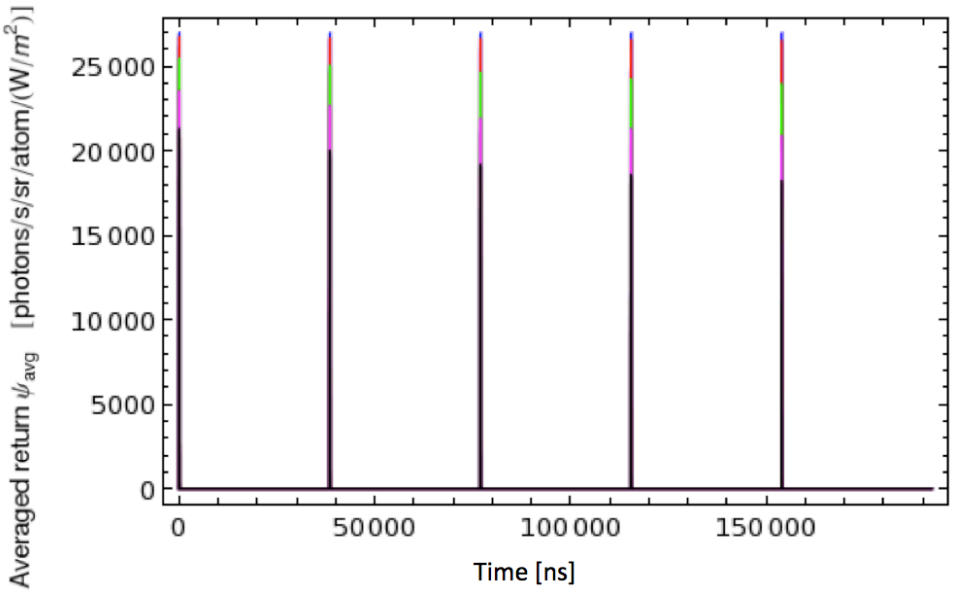

Figure 4.4: Simulation of 5 cycles of the laser for the Keck II LGS, showing return in the mesosphere as a function of time. The ~38 μs dark time between pulses results in very little pulse-to-pulse variability.

The plot in Figure 4.5 has the predicted return flux at the top of the telescope, as a function of launched power. For the ~12 W expected to be projected from the launch telescope, the simulations predict ~4.2×10^6 photons/s/m^2, for a sodium column density of 4×10^{13} atoms/m^2. However, measurements reported in the literature indicate between ~0.7 and 1.75×10^6 photons/s/m^2 are being received at the

telescope (Le Mignant et al. 2006). This again constitutes a factor of 2 – 3 discrepancy between data and simulation.

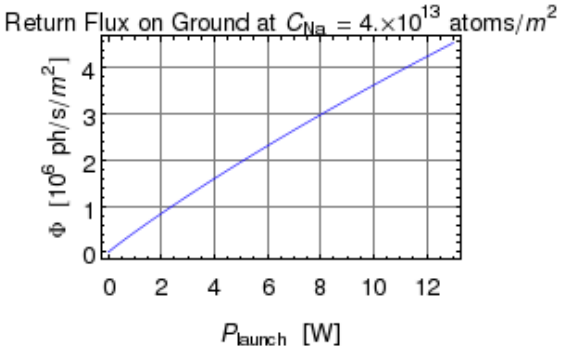

Figure 4.5: Predicted return flux as a function of launched laser power, based on simulation of 5 cycles of the Keck II LGS. The measured average return is ~1.2 × 10^6 photons/s/m^2 for ~12 Watts launched.

The Keck I system differs from Keck II primarily with regard to the laser and beam transport system. On Keck I, the laser projects from behind the telescope's secondary mirror, while the Keck II LGS is currently launched from the side of the primary mirror. The Keck I laser was developed by Lockheed Martin Coherent Technology (LMCT) and is a solid-state mode-locked CW laser, which uses sum frequency generation (SFG) of beams at 1064 nm and 1319 nm to achieve the 589 nm sodium wavelength (Sawruk et al. 2010). The efficiency of the SFG process increases nonlinearly with input light intensity, so to maximize this the laser is formatted as a train of short pulses to achieve high peak intensity. Though the average launched power is considerably higher for this laser (~ 20 Watts), the return from the sodium layer is on average nearly equal to, or only slightly higher, than what is seen from the Keck II LGS (Chin et al. 2012).

In Figure 4.6, a 100 pulse train of the Keck I laser is shown. Each pulse is 300 picoseconds FWHM and the repetition rate is 82 MHz. The beam is also modulated to have a 1.5 GHz FWHM spectrum. The simulation used square pulses with five levels of irradiance, and assumed a 0.6 m FWHM Gaussian spot. The time evolution in Figure 4.6 shows that the specific return reaches steady state within only the first ~100 ns of the laser being on.

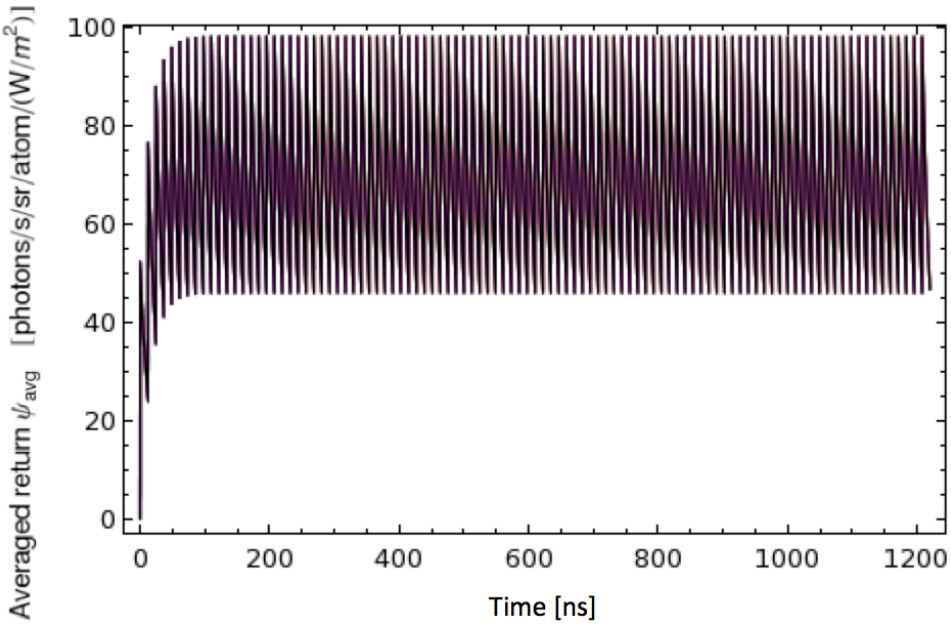

Figure 4.6: Simulation of 100 cycles of the laser for the Keck I LGS, showing return in the mesosphere as a function of time. This format reaches steady state within only 100 μs.

Figure 4.7 shows the expected return flux at the top of the telescope from the Keck I LGS, assuming a C_{Na} of 4×10^{13} atoms/m^2. Comparing this return as a function of launched power to the same graph for the Keck II laser in Figure 4.5 indicates that this format is less effective at exciting the sodium layer. For 10 Watts launched power from this laser only ~2.8×10^6 photons/s/m^2 are predicted, compared

to ~ 3.6×10^6 photons/s/m^2 for the dye laser. Again for this system, the measured return flux is a factor of 2 – 3 less than what is expected based on the simulations.

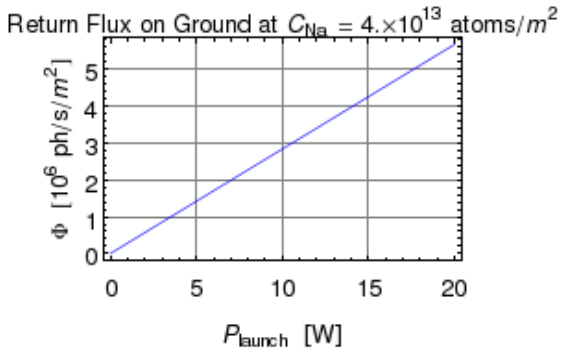

Figure 4.7: Predicted return flux as a function of launched laser power for the Keck I LGS. Based on the average reported measured return of ~1.5×10^6 photons/s/m^2, the simulations are over-predicting by a factor of 2 – 3 in this case as well.

A possibility that has been suggested is that some larger portion than expected of the laser power may be getting lost during beam transport and launch, leading to the observed discrepancy with model predictions. However, based on the plots in Figures 4.5 and 4.7, somewhere near 70% of the power would have to be diverted elsewhere (assuming the other parameters used are accurate), which is a situation that does not seem feasible.

This inconsistency between the model and actual measurements for these short pulse lasers likely signals a need for inclusion of greater detail in the simulations (this is discussed in the next section). The LGSBloch package, in its current form, gives acceptable predictions of the return measurements seen from narrow bandwidth CW LGS (i.e. the 50 W Fasortronics laser at the SOR), and reproduced the relative factor of ~3 reduction in return flux seen at the Shane

telescope when the spectrum broadening phase modulators were switched off (presumably this is caused by increased saturation of the sodium layer).

It seems plausible that the significantly higher peak powers during short pulses (~5000 W for the Shane LGS) make it necessary to account for a realistic speckled irradiance pattern in the mesosphere, instead of the simplified Gaussian profile, and similarly for the frequency spectrum. However, because the amount of the discrepancy is essentially constant for both the Lick and Keck observatories, all considerations must investigate the relevant influences pertinent at both locations.

4.3 A more detailed model yielded equivalent results

In consultation with Rochester Scientific, I addressed the discrepancy between the model predictions and measurements by inclusion of more realistic simulation parameters. These efforts focused on the LGS system on the Shane telescope. The increased speed of the proprietary code developed by Rochester Scientific allowed simulation of longer timespans (i.e. additional cycles of the laser, to ensure the return flux has settled to a constant value). We also investigated the effects of including an output spectrum designed to replicate the measured spectrum, and a more physically accurate irradiance profile.

The first round of simulations incorporated the following parameters: average laser power 9 Watts, pulse length 150 ns, repetition rate 11 kHz, linear polarization, light centered on the peak of the D_2a resonance with a 2 GHz FWHM Lorentzian laser spectrum. The environmental parameters assumed were a spin-randomizing collision time of 1 ms, a velocity-changing collision time of 70 μs (all previous work

used 245 μs and 35 μs, for these values, respectively), and magnetic field strength of 0.47 Gauss pointed at an angle of 151.6° with respect to the laser propagation direction (zenith). A length of time corresponding to 10 pulses was modeled, although only two pulses were required for the signal to settle to its steady value (the first cycle gives ~10% higher return). Calculations were completed for a range of light intensities, and the results were integrated over a Gaussian beam profile of 0.6 m FWHM, to find the flux in units of photons/s/sr/atom. Figure 4.8 shows these 10 pulses as a function of time.

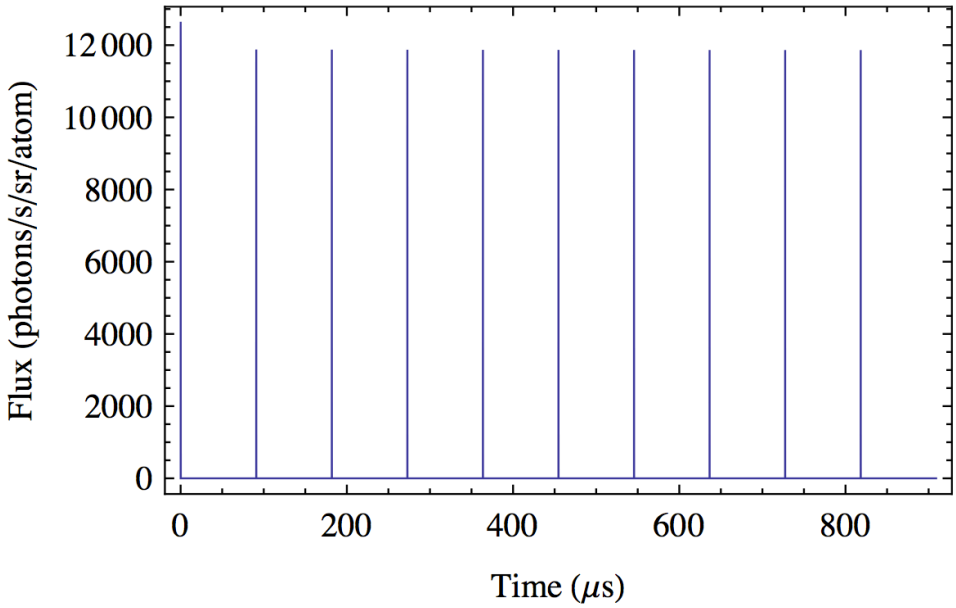

Figure 4.8: Return flux in the mesosphere for the Shane dye laser, for a 10 pulse train. The first pulse gave ~10% greater return than subsequent pulses. (Credit: Simon Rochester)

To predict the flux that would be observed at the top of the telescope, the integrated signal was multiplied by a column density of 4×10^{13} atom/m^2, divided by the square of the distance to the sodium layer, 92 km, multiplied by the square of the atmospheric transmission (assumed to be 85%), and multiplied by another factor of

0.96 to account for resonant absorption in the sodium layer. This calculation produced an expected flux of 1.94×10^6 photons/s/m^2, which is only slightly closer to the observed quantity than what was generated by previous estimates.

In Sections 4.1 – 4.3, my modeling of the Shane LGS involved approximating the spectrum as a Gaussian centered on the D_2a line, with FWHM values between 1.5 and 2.2 GHz. The actual spectrum was designed to fill the double-peaked sodium Doppler profile, as shown on the left side of Figure 4.9. On the right in this figure is an image of the measured spectrum from the Fabry-Perot interferometer at the telescope, which clearly shows the two peaks but with a somewhat different overall structure.

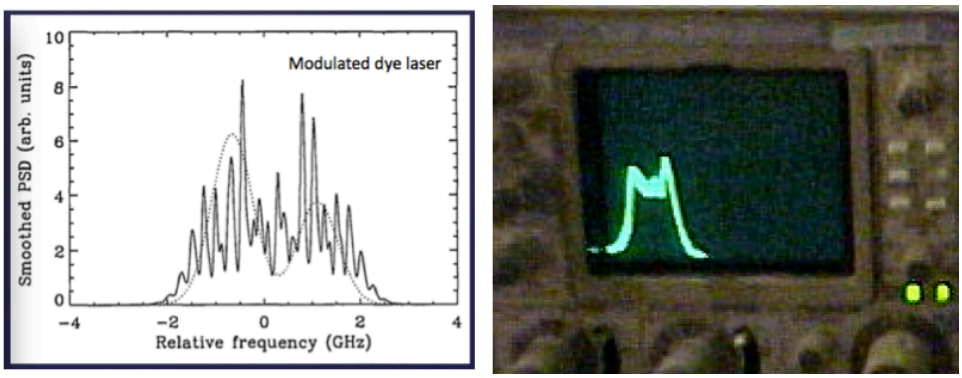

Figure 4.9: The left plot shows the target spectrum for modulation of the dye laser on the Shane telescope. The right image shows a photograph of the measured spectrum.

To explore the effect of changing the laser spectrum to better approximate what is observed, a sample spectral function was constructed out of a sum of Lorentzians by eyeballing the measured spectrum. This is shown in Figure 4.10. Using this more realistic spectrum, the calculated return flux was slightly higher (2.04×10^6 photons/s/m^2), hence there was no improved agreement with return flux data.

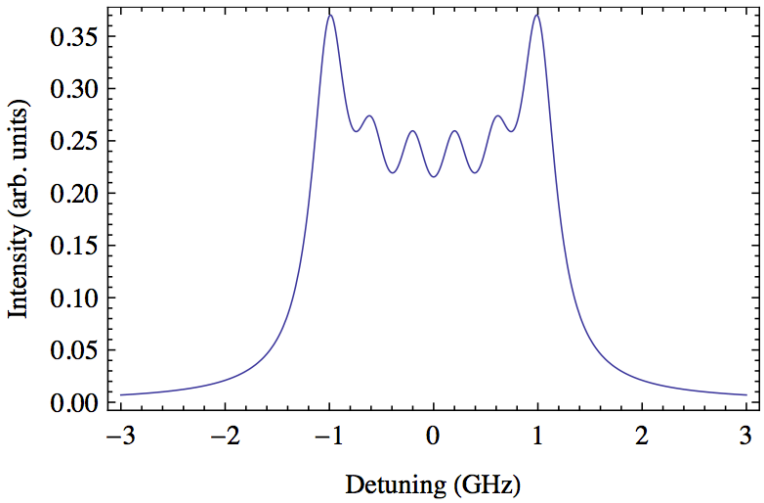

Figure 4.10: This approximate spectral function was constructed out of a sum of Lorentzians by eyeballing the measured spectrum. Using this into the model increased the predicted return, exacerbating the discrepancy. (Credit: Simon Rochester)

To address the effects of atmospheric turbulence on the mesospheric irradiance distribution, I used physical optics modeling in IDL. This code uses methods developed by Fresnel and Fourier (Goodman 2004) to propagate a Gaussian or top hat shaped wavefront, with user specified beam size and quality, from the launch telescope to the mesosphere. Ground layer turbulence is modeled by adding phase aberrations generated with the same simulation program used in Chapter 2 for validation of the phase plates. The mesosphere is treated as a two-dimensional surface at 95 km. To investigate the distribution of light intensity on this surface, the array is binned into a histogram with irradiance (units of W/m^2) on the x-axis, and the amount of area illuminated at this level on the y-axis (units of m^2).

For Mt. Hamilton, I used a 20 cm diameter beam, launched with 3.3 radians peak-to-valley astigmatism on the otherwise top hat shaped wavefront, to replicate the observed beam quality ($M^2 \approx 2$, Gavel et al. 1998). The simulated atmosphere was set

to have r_0 = 10 cm, and histograms from propagation with 100 different realizations of atmosphere (i.e. different seed values in the turbulence generator) were averaged. This average histogram was then compared to a histogram generated for a Gaussian beam profile of comparable size. Each histogram had 1000 equal sized bins, where the bin size was set from the peak-to-valley of the irradiance distribution (the average in the case of the averaged histogram).

Figure 4.11 displays the appearance of an intensity distribution for a typical speckle pattern, and a Gaussian mesospheric beam profile of comparable size, where both have the same spatial scale and total power. To associate the size of the speckled profile with the FWHM of a Gaussian, I used the area within which half the power was contained, corresponding to the highest irradiance levels (i.e. the half-power area). This method was verified to give the FWHM of a Gaussian, and is not the same as the area at half the maximal irradiance for the aberrated profiles. The right plots in Figure 4.11 show these equal areas as white centers in the two-dimensional irradiance profiles (the Gaussian has FWHM of 0.5 m). A discussion of the appropriateness of this comparison, and how the beam profile affects the spot size in a Shack-Hartmann WFS, will be presented in Chapter 5, Section 3.

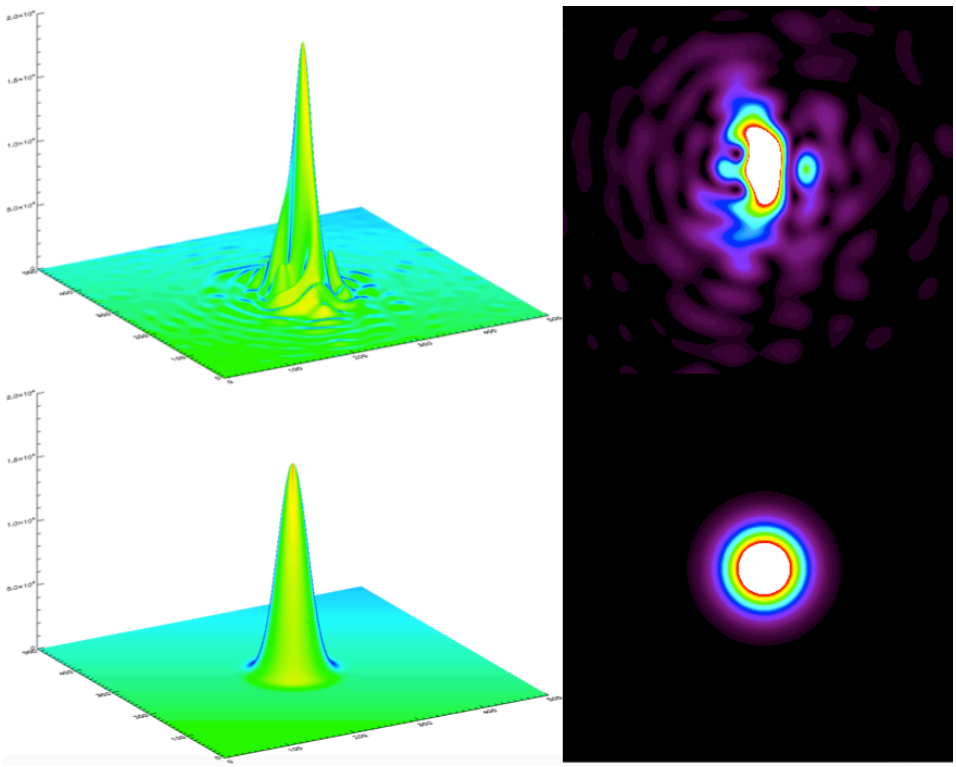

Figure 4.11: Irradiance profiles for propagation through turbulence (top) versus a Gaussian of comparable size (bottom), plotted with the same spatial scales. The representative sizes are calculated by integrating over the region containing half the power and corresponding to the highest irradiance levels.

Figure 4.12 shows comparisons of the histogram from the Gaussian beam profile (purple) compared to the average of 100 histograms for beams propagated through turbulence (blue). This average of histograms is not the same as the histogram of the average of the speckle patterns, since in that case intensity distribution information is lost as the spatial variations are smoothed. The top plot in Figure 4.12 shows the histogram of the area in the mesosphere illuminated with a particular light intensity (W/m^2). The lower graph gives the percentage of the total power contained at each irradiance level (i.e. in each histogram bin). For the Gaussian beam profile (purple), there is a roughly equal amount of power at each

level. Because the histogram contains 1000 bins, this results in ~0.1% of the total power in each bin. The average of histograms with turbulence (blue) has a maximum irradiance of 2.06×10^4 W/m^2, which is higher than in the Gaussian profile (with maximum 1.76×10^4 W/m^2), giving quantitative evidence of the hot spots created by the turbulence.

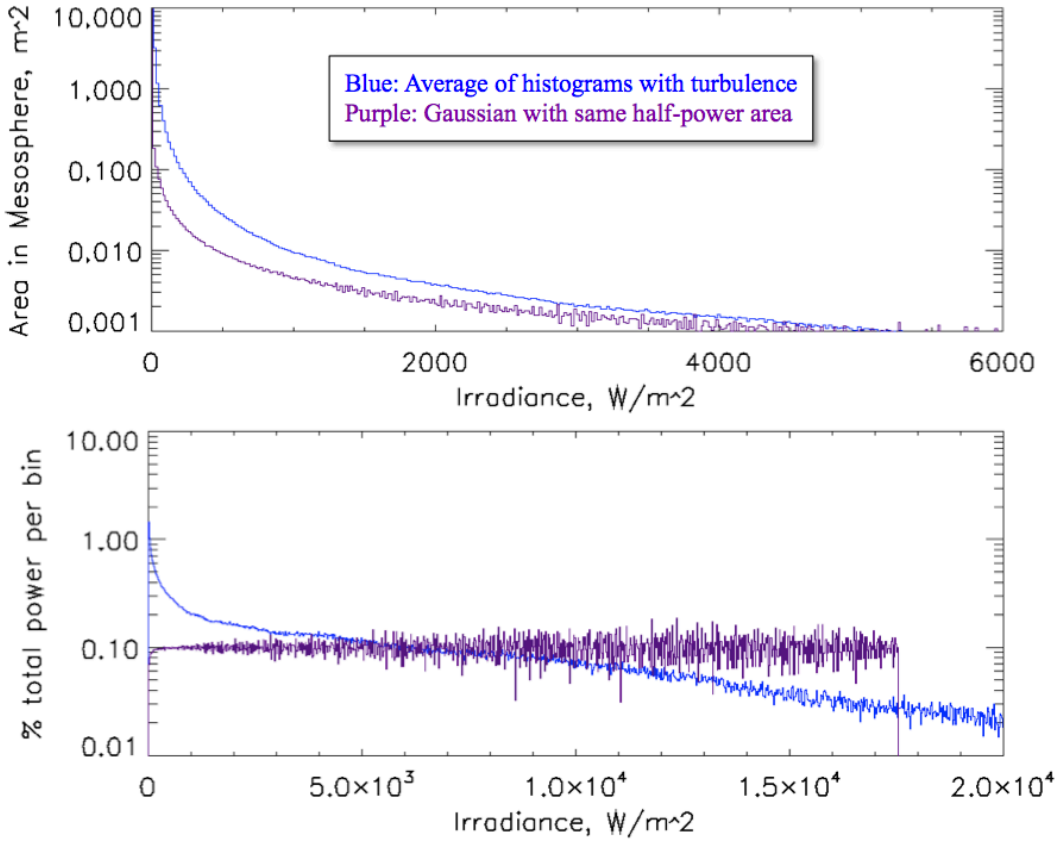

Figure 4.12: Average histogram of irradiance distributions from propagation through 100 different realizations of computer generated turbulence screens (blue) versus a Gaussian profile with 0.5 m FWHM (purple). Although differences between the two are observable, use of the realistic profile did not lead to significant change in the simulation predictions.

What can be learned from Figure 4.12 is that atmospheric turbulence results in an excess of area illuminated at low energy levels, and has a higher fraction of the total power contained at these levels. Although the peak intensity is slightly higher

than for the Gaussian distribution, only tiny fractions of the total power and area are contained in these hot spots.

Intriguingly, the differences between the two profiles did not significantly alter the predictions of return flux when the average of the speckle histograms replaced the Gaussian profile used previously in the LGS simulation code. Evidently, the greater area (and more sodium atoms) illuminated at lower levels in the aberrated profiles balanced with the higher fractions of total power at higher irradiance levels in the Gaussian.

The endeavors discussed in this section aimed to reduce the factor of 2 – 3 discrepancy between the measured return flux and what is predicted by atomic density matrix calculations for short pulse LGS (and specifically the dye laser currently on the Shane telescope). Instead, it was confirmed that assuming a Gaussian beam profile is acceptable in the case of a 20 cm diameter launched beam, even with high instantaneous power levels (~5000 W during the pulse). It was also found that accounting for a realistic laser spectrum did not improve the comparison of data and theory. Future avenues to explore this topic will be discussed in the next chapter.

4.4 Discussion

Predicted return fluxes from the LGSBloch simulation package have been shown to be reasonably accurate for the case of CW LGS, but to overestimate the return of short pulse systems by about a factor of ~2 – 3. The single case of a CW

LGS has been the 50 Watt Fasortronics laser at SOR. For the short pulse systems, I modeled the LGS at the Lick and Keck Observatories, and findings of a similar discrepancy were reported for comparison with the system at the Gemini South Observatory (Holzlohner et al. 2012).

First efforts to address the discrepancy encompassed double-checking the parameters related to how the measurements of return flux were made, such as quantum efficiency of the detector and throughput of the system. At Mt. Hamilton, the throughput of the AO system to the WFS had most recently been assessed in 2004, so there existed a level of uncertainty in what the exact value was. This was addressed by measuring the brightness of spectrophotometric standard stars through a sodium filter. The results agreed well with the previous measurements, so this did not yield improved agreement between the simulations and data.

The second direction pursued involved including a greater level of detail in the modeling parameters. Because the main differences between the CW and pulsed lasers are the instantaneous power levels (much higher for pulses) and the frequency spectrum, these parameters were used as the starting point. I created realistic irradiance distribution histograms using a light propagation code with atmospheric distortions. The average of 100 histograms for different realizations of turbulence showed some difference from a Gaussian profile of comparable size (Figure 4.12). However, this more realistic distribution of light levels did not result in significant changes to the predicted return. Similarly, inclusion of a laser spectrum based on

measurements by the Fabory-Perot at Mt. Hamilton also did not yield more congruent results.

One conclusion that comes from this investigation is that since making the assumption of a Gaussian spot only leads to minor changes, it can be considered an acceptable approximation, at least for small launch telescopes.

It has been suggested that the problem could be some unknown fraction of the light getting lost, or diverted to non-interacting frequencies, between the diagnostic power measurements and laser launch. The likeliness of this can be ascertained from plots such as Figures 4.5 and 4.7, which show return at the telescope as a function of launched power. From these graphs, it is clear that somewhere near 70% of the power would have to be lost (assuming the other parameters used are reasonably accurate), a situation that does not seem feasible. Nonetheless, it is likely still a worthwhile endeavor to identify any currently unmeasured processes within the laser launch system that could cause power loss or spectral changes.

It is hoped that the recently commissioned European Southern Observatory Wendelstein transportable 20 Watt LGS unit (Bonaccini Calia et al. 2010) will soon provide further experimental tests and confirmation of LGSBloch simulations. This system is designed to do systematic field studies of LGS return flux versus laser parameters. Its capabilities include adjustment of the output polarization state, variable line width between ~5–25 MHz, adjustable repumping up to 30%, and pulse modes with amplitude modulation frequencies between 1 and 700 kHz.

Given the overall complexity of the LGS systems and the large number of not well-determined parameters, currently having a factor of 2 – 3 difference between reality and simulation constitutes a non-negligible level of success. The third section in Chapter 5 is dedicated to other possibilities that should be investigated, and suggests experiments (with current and future systems) that could further probe the nature of the present issues.

Chapter 5

Future Directions and Open Problems

5.1 Introduction

In this thesis, I presented results from two projects that address current deficiencies within the extremely successful and rapidly evolving field of Adaptive Optics (AO). The first project provided a lightweight, robust, and economical means of simulating atmospheric turbulence for laboratory testbed experiments, on-sky instrument calibration systems, and with the telescope simulators used for integration and testing. The second project undertook a detailed examination of the atomic physics behind the generation of sodium laser guide stars, and provided quantitative guidelines for optimizing the efficiency of these costly but invaluable additions to AO technology.

I have shown that inexpensive materials can be used to create effective atmospheric simulation devices. As discussed in Chapter 2, the cost and complexity of AO systems make it necessary to have a good understanding of their behavior under known and controllable conditions before they are subjected to the observatory environment. The plates produced by this method are shown to follow Kolmogorov statistics closely, and can be manufactured with a variety of turbulence strengths.

The LGSBloch simulation package has permitted new insights into how laser light interacts with mesospheric sodium. Guidelines for current and future system designers were identified in Chapter 3. Issues linger with accurately reproducing measurements from all types of LGS (the subject of Chapter 4), however, this code remains a vital tool in understanding the atomic physics of sodium excitation. It has offered unique insights into the evolution of the energy level populations, in addition to other physical effects such as Larmor precession, atomic recoil, and collisions with other constituents of the upper atmosphere.

The next section describes the anticipated future of phase plate manufacturing at the Laboratory for Adaptive Optics at UC Santa Cruz. This includes description of the current hindrances to efficient production, and proposals for ameliorating these concerns. Section 5.3 addresses potential avenues to improving the simulation of LGS return, and better understanding of LGS behavior. Suggestion of experiments that will help identify the source of the current discrepancy are also put forward. In Section 5.4, an innovative idea proposed at the 2012 Center for Adaptive Optics (CfAO) Laser Workshop by Paul Hillman, of Fasortronics, is discussed. He has suggested a possible means of achieving greater than CW return from a pulsed laser system under certain circumstances, which I have briefly investigated for the locations of Mt. Hamilton and Mauna Kea. Section 5.5 gives a brief overview the current state of the two projects discussed in this thesis, reviews the accomplishments, and mentions a few other areas of research that could prove beneficial to future considerations.

5.2 The future of phase plate manufacturing at the Laboratory for Adaptive Optics

There are two main obstacles to achieving an expedited manufacturing process: (1) dust, and (2) the spray paint ejection rate is not always consistent from the spray cans currently used. Steps are being taken by LAO researchers to address these issues, with the hope of improving this technology and ensuring its availability in the future. Establishing a consistent framework for plate distribution and technology transfer is also underway. Lastly, I have observed some peculiar statistical properties of certain phase measurements, of which a more detailed analysis could lead to insights into the nature of phase aberrations.

The machine is currently operating within a fume hood in a room where the ventilation system does not have adequate filters. Filters cannot simply be installed over the ceiling vents, because this will reduce the amount of airflow into the room, resulting in a vacuum (since the fume hoods remove air at a constant rate). This vacuum could be dangerous for people entering and exiting the room. A new laboratory space has recently been identified as a potential solution to this problem. This is an unused fume hood located in the Lick Observatory CCD laboratory, which is a cleaner environment and offers more flexibility to future improvements in environmental control.

To address the variable paint ejection rate from the currently used spray cans, we have proposed to replace this part of the apparatus with an airbrush system. This should allow a much greater level of control over the amount of paint deposited, and

will negate the issue of cans sputtering or running out of paint mid-fabrication. Upgrading the system in this manner will result in the need to recalibrate the process, but will potentially result in a significant increase to the useful device production rate, and expand the range of achievable parameters.

For not entirely well understood reasons, some locations on the handmade plates show a discrepancy between the power spectrum and structure function. Thus far, two main types of peculiarities have been noticed. In some cases, the power spectrum agrees well with Kolmogorov statistics and has a well-defined value of r_0. However, the slope of the structure function is significantly less than the expected 5/3, making r_0 not clearly determinable, as shown in Figure 5.1. The second oddity is that occasionally the structure function fits precisely but the power spectrum has a non-linear shape. An example is given in Figure 5.2.

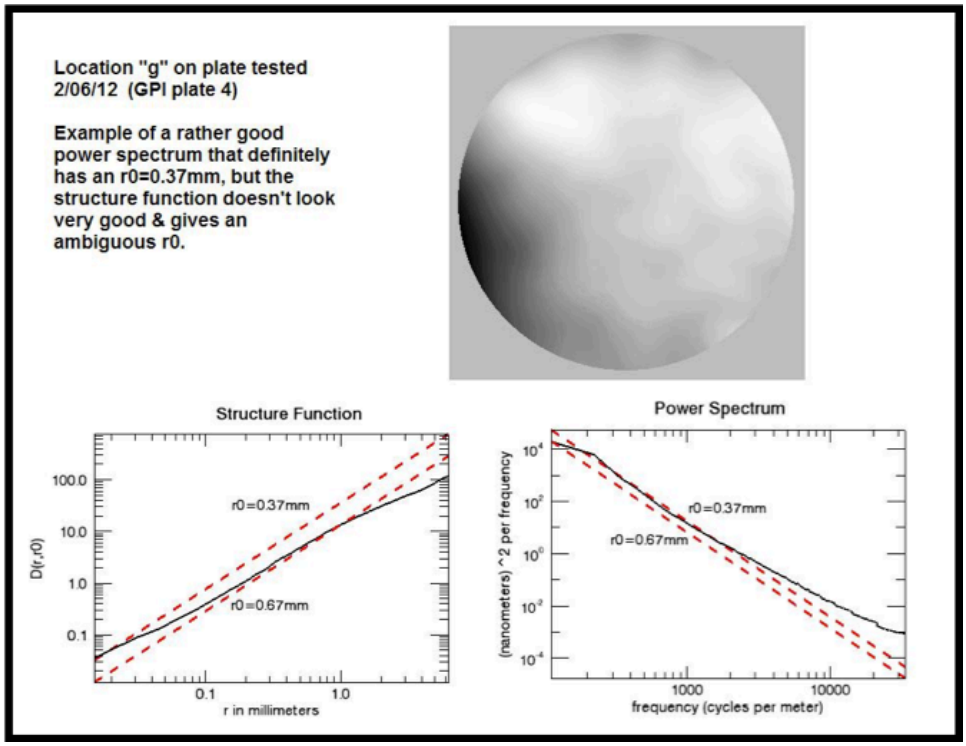

Figure 5.1: Peculiar phase, case 1: The power spectrum agrees well with Kolmogorov statistics and has a well-defined value of r_0. However, the slope of the structure function is significantly less than the expected 5/3, thus r_0 is not clearly determinable.

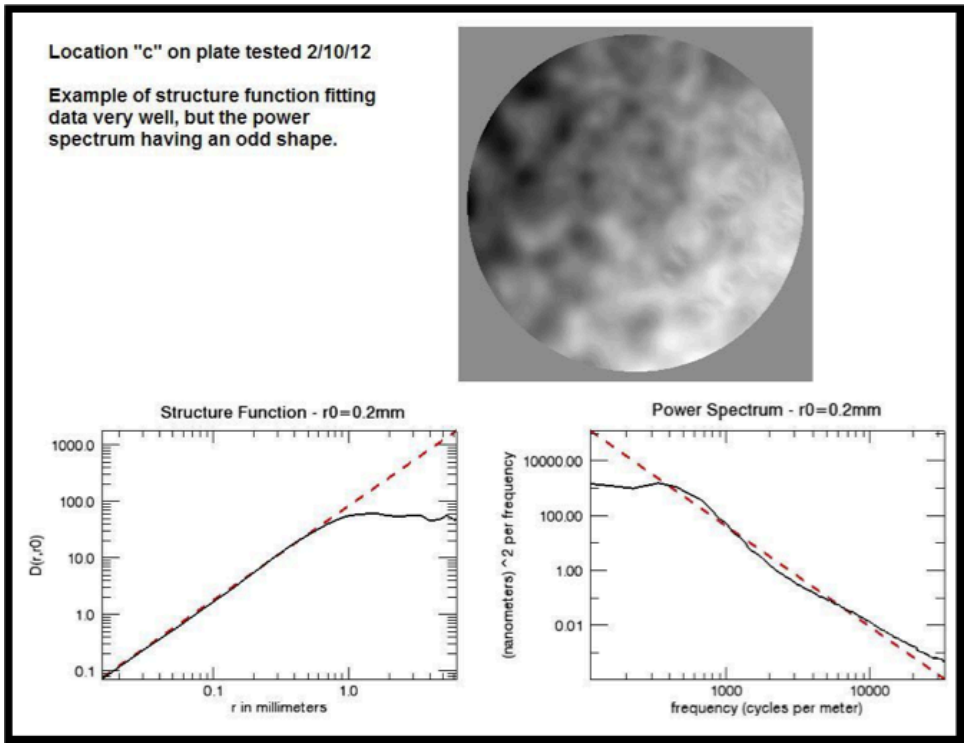

Figure 5.2: Peculiar phase, case 2: The structure function fits precisely, but the power spectrum has a non-linear shape.

Such issues are generally only seen in a small number of measurements (if at all) on an otherwise good plate, and give no indication of abnormality in the appearance of the reconstructed phases. Clearly, these occurrences signal a fluctuation of the statistics from Kolmogorov theory, perhaps not dissimilarly to the real atmosphere. Identifying the underlying mathematical origin of such behavior may lead to insights into the general nature of turbulence and phase aberrations. Despite this occasional variability, these plates are still considered highly valuable for scientific use.

5.3 Towards improved modeling and a better understanding of Laser Guide Stars

An important step in improving the understanding of sodium-light interactions is accumulating additional experimental information. This can be facilitated by increased data collection and analysis with currently operating LGS, measurements from systems that will begin operation in the near future, and potentially with sodium cell investigations in the laboratory. This section proffers guidelines for obtaining experimental validation of behaviors suggested by theoretical considerations, and directions to pursue for fully optimizing LGS AO performance.

Thus far, assessment of the ability of the LGSBloch model to reproduce measurements from the short pulse lasers at the Lick and Keck Observatories has only pertained to full power operations with full frequency modulation and zenith pointing. However, interesting information will be gained by comparison to simulation predictions at a range of power levels. Experiments on changing the modulation have been performed with the aim of optimizing return, but the results have not been tabulated in a manner that permits quantitative analysis. Dedicated tests to evaluate the effect of changing the power and spectrum of the laser will help illuminate the specific areas of our understanding that require improvement.

Systems such as the Wendelstein transportable laser (mentioned in Section 4.4) and the LLNL fiber laser will be able to probe the parameter space of longer pulse lengths and higher duty cycles. Because these formats will be capable of

optical pumping with circular polarized light, their return should be characterized for a variety of angles of propagation with respect to Earth's magnetic field.

Due to the variability of seeing conditions and mesospheric sodium abundance, the most useful on-sky tests should be averaged over as long a timeframe as possible, and repeated on different dates throughout the year and at different locations. An ideal scenario would be to dedicate a Lidar system to take measurements of the sodium column density, removing this unknown from the equation.

Appropriately devised tests with pulsed lasers may be capable of returning information about other parameters that are required for a complete understanding of the sodium-light system. Collisions between sodium and N_2 and O_2 have a significant effect on the population of the atomic states, so knowing the timescales involved is an important factor in accurately calculating LGS return flux. However, since the sodium abundance, layer thickness, and altitude are highly variable, and the profile often deviates significantly from Gaussian, it is difficult to obtain high accuracy in these parameters. Some preliminary investigation of how different collision rates produce different return flux vs. time behavior suggests they are responsible for the initial enhancement seen in Figure 3.6. This higher than steady state return when the laser is first turned on is responsible for the predicted return flux from long pulse lasers (with ~10 – 30 μs illumination) not simply being the CW return multiplied by the duty cycle.

In Figure 5.3, graphs similar to those in Figure 3.6, but with differing collision rates, demonstrate the effects on the number of photons returned as a function of time. These simulations are for 10% repumping, in the absence of a magnetic field. The default collision times in LGSBloch are 245 μs for spin-randomizing, and 35 μs for velocity-changing. In the left plot, I multiplied them by 2, making the new values 490 μs for spin-randomizing, and 70 μs for velocity-changing. The initial peaks are now slightly higher than with the default values, and the decline has become more extended, and does not level off during the 100 μs simulation time. In the right graph, the collision times were divided by 10, resulting in 24.5 μs for spin-randomizing, and 3.5 μs for velocity-changing. The plot of return vs. time now looks very different, with the initial peak no longer present.

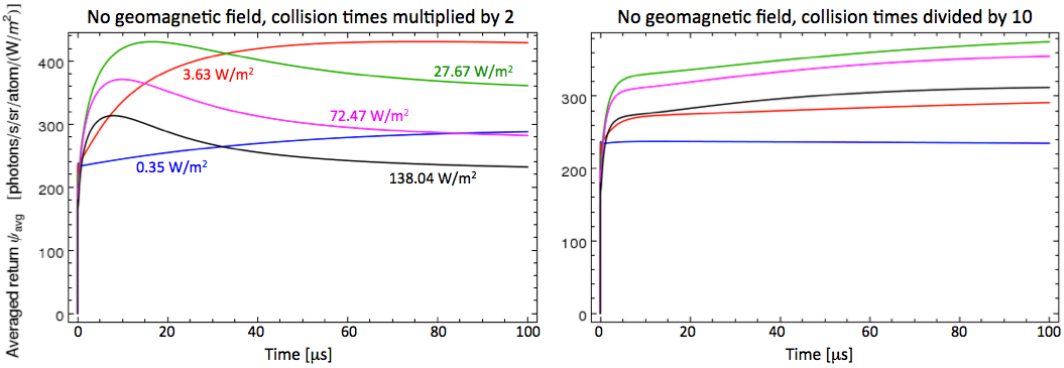

Figure 5.3: Changes in the return flux as a function of time are quite significant for different collision times. In the left plot, I multiplied the default values by 2, and for the right graph, they were divided by 10. The differences in the initial behavior of the return may allow pulsed laser to be used to better determine collision rates.

The right plot in Figure 5.3 suggests that when the time between collisions is short, optical pumping is significantly reduced (mostly by the velocity-changing variety). What is more mysterious is that the return from all but the lowest irradiance level continues to increase during the 100 μs simulation. This is understood as due to

the collisions mitigating spectral hole burning from atomic recoil (Holzlohner et al. 2010).

The total CW return flux changes little between the two cases in Figure 5.3, but since the return flux from long pulse systems depends on the average return during the first few microseconds of illumination, experimentation with such systems may yield a clearer understanding of these variables.

Experiments with sodium cells may also provide a useful means of advancing our understanding of sodium-light interactions. It is difficult to reproduce the low pressure and temperature conditions of the upper atmosphere in a laboratory setting, but in theory the LGSBloch code is capable of simulating a range of system parameters, including those of standard sodium cells. The measurement of changes in fluorescence on very short time scales (less than collision times) at the onset of laser irradiance could examine the phenomenon of optical pumping and how it relates to other processes present in the system (such as Larmor precession and downpumping). Additionally, a validation of the current understanding of saturation and stimulated emission would be beneficial, since this is an important factor in understanding the high peak power of pulsed laser systems.

As part of the attempt to mend the disagreement between theoretical predictions and measured returns (during collaboration with Rochester Scientific), it was determined that using a more realistic laser spectrum and irradiance profile did not significantly alter the results for the case of a 20 cm launched beam. This

validates the use of a Gaussian beam profile as a reasonable approximation, at least for small launch telescopes.

For larger launch telescopes, the light distribution in the mesosphere becomes more speckled, and it no longer seems appropriate to use this metric to determine an equivalent size Gaussian beam profile. In Figure 5.4, the progression is shown from a diffraction limited Airy pattern to a speckled irradiance profile, for beacons launched with diameters of 0.2 m, 0.5 m. and 1 m. The single turbulence screen used here gives a histogram with statistics that closely matches the properties of the histogram of the average of 100 phase screens (as discussed in Section 4.3). The dimensions of each thumbnail correspond to ~1.9 m (per side) in the mesosphere, and the color scale is based on the peak-to-valley of the intensity distribution.

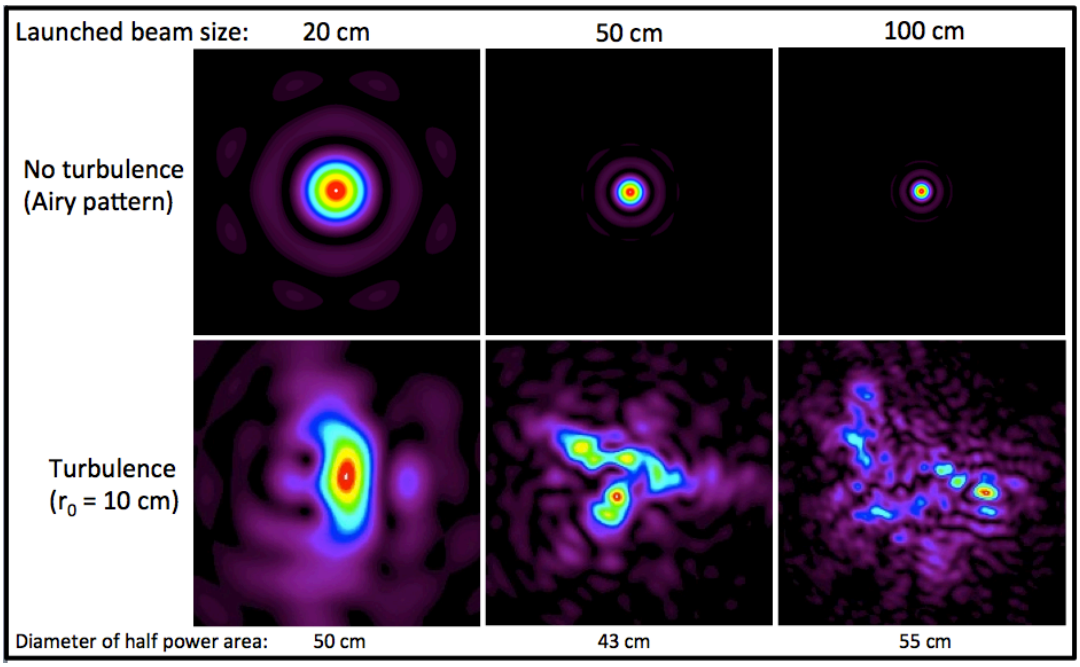

Figure 5.4: The diameter of the laser beam when exiting the launch telescope changes the distribution of light in the mesosphere. Above, irradiance profiles are shown for propagation without turbulence (top row) and with an average turbulence screen (bottom

row) for 0.2 m, 0.5 m, and 1 m diameter beams. There is obvious broadening of the distribution that is not revealed by the diameter of the half power area.

Figure 5.5 compares the histograms from a 0.5 m diameter launch telescope (same as Figure 4.12, which shows the 0.2 m case). The Gaussian beam profile (purple) has the same half power area as the average of 100 histograms for beams propagated through turbulence with r_0 = 10 cm (blue). Comparing this to Figure 4.12 shows an even greater difference between the two types of profiles with the larger beam, meaning an increased likelihood that their use in estimating return flux will yield different results. This suggests it may be important to take into account the realistic light distribution profile when modeling systems with larger launch telescopes.

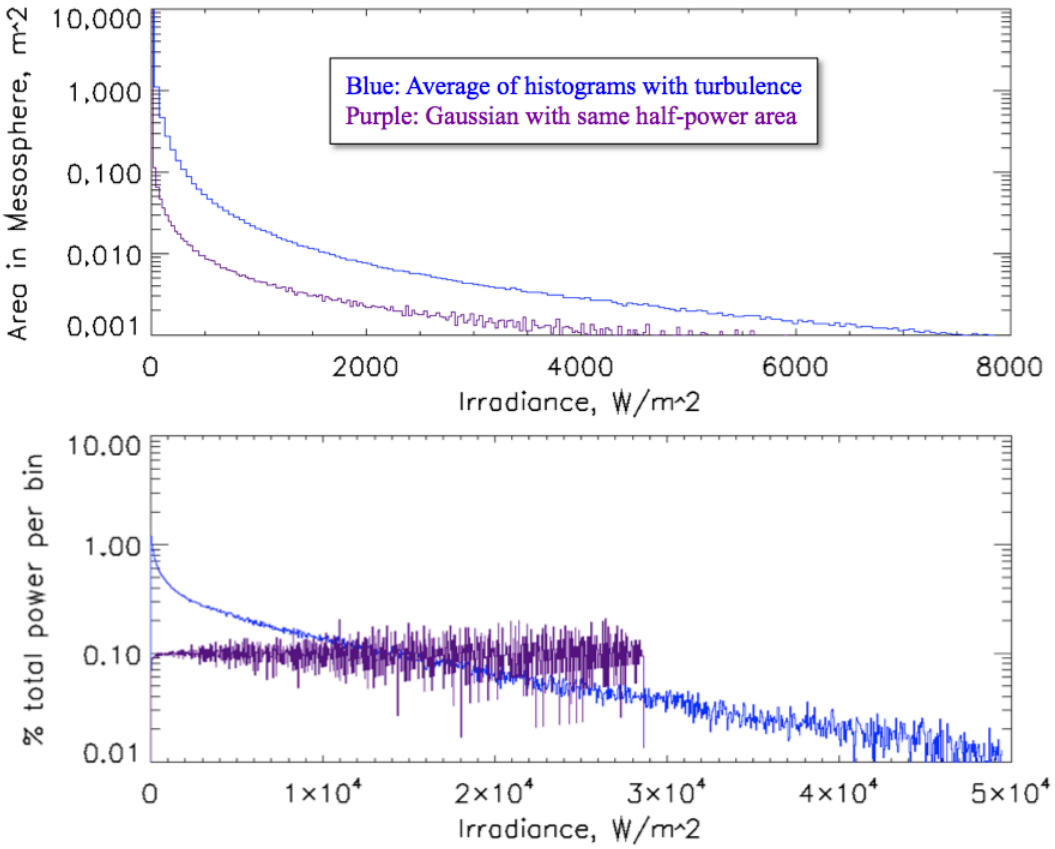

Figure 5.5: Average of histograms for irradiance profiles of a beam launched with 0.5 m diameter (blue), compared to a Gaussian with same half power area (purple). The differences here are more pronounced than for a 0.2 m launch telescope (Figure 4.12), making it likely that use of a Gaussian in the model will give a different result than the realistic profile.

An important topic for LGS AO system performance is how the beam profile in the mesosphere translates to a spot size on a Shack-Hartmann wavefront sensor. This could be assessed by propagating the speckle pattern back to the ground, with angle-of-arrival information, and superimposing it onto a Hartmann grid. Such an analysis would allow characterization of the effects of changing the size and shape of the beam, which can be used to define both optimal launch telescope size and the amount of improvement gained from uplink correction. A similar study for enhancing system performance would quantify the improvements in signal-to-noise ratios for Raleigh blanking and pulse tracking formats. This will allow full cost-benefit assessment of the various options.

5.4 Can pulsed lasers produce brighter guide stars than CW?

The question of whether pulsed LGS can produce beacons that are brighter (or as bright) as those from CW lasers arose when, after investigating the time dependent behavior of sodium excitation, an enhancement in the number of spontaneously emitted photons was observed during the first few microseconds of initial laser irradiance.

In Figure 5.6, the return as a function of time is shown for a 500 μs simulation of a 100 W/m^2 irradiance level, with 10% repumping for zenith pointing at Mt. Hamilton. During the first 10 μs, the average return is 287 photons/s/sr/atom/(W/m^2);

at the end of 500 μs it has declined to 200 photons/s/sr/atom/(W/m^2). Because of this reduction as the laser remains on (as discussed in Chapter 3), a long pulse (30 μs), high duty cycle (20%) system is predicted to achieve within 10% of the brightness of a CW beam.

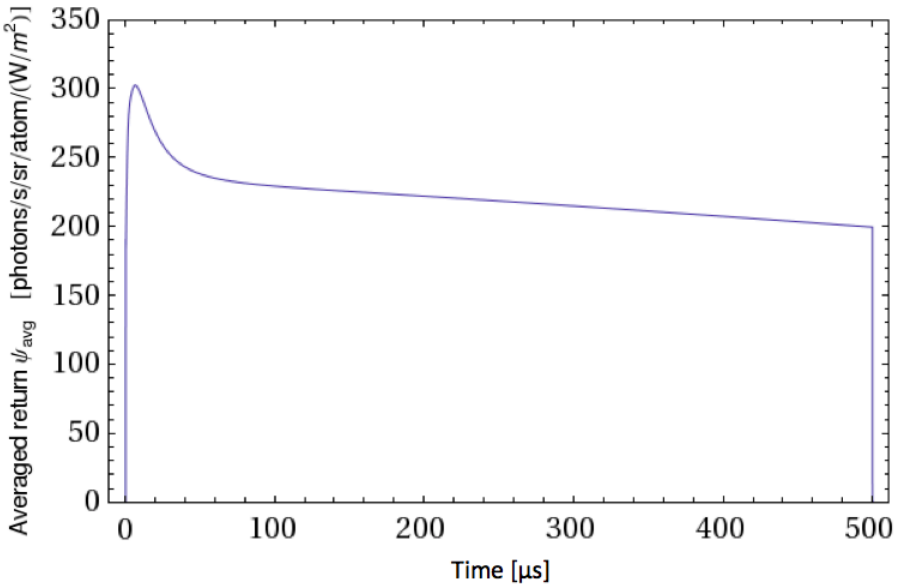

Figure 5.6: This 500 μs simulation, for a 100 W/m^2 irradiance and 10% repumping, shows the initial enhancement in spontaneously emitted photons when the laser light is first incident on the sodium atoms. It suggests the possibility of certain pulsed formats being able to produce equal or greater returns than a CW laser.

The cause of this peak in return during the first few microseconds of laser irradiance (discussed in Chapter 3) can be understood as a result of the processes that thwart optical pumping acting on different timescales. These processes include Larmor precession from the geomagnetic field, downpumping (atoms falling into the F=1 ground state), and collisions with other mesosphere constituents (such as N_2 and O_2).

Paul Hillman's recent suggestion is that pulsing the laser at the Larmor frequency may be able to avoid the detrimental effects of atomic states changing their

magnetic quantum number as they precess. This is similar to an idea in the field of Magnetometry to use modulated lasers to measure the strength of Earth's magnetic field at different locations (Budker et al. 2007). Figure 5.7 (created by Paul Hillman) suggests that such a scheme could produce 80% higher returns than a CW laser with the same average power, when propagating perpendicular to the magnetic field. This possibility is especially enticing for observatories located near the equator, where LGS spend the majority of time oriented at or near perpendicular to the magnetic field.

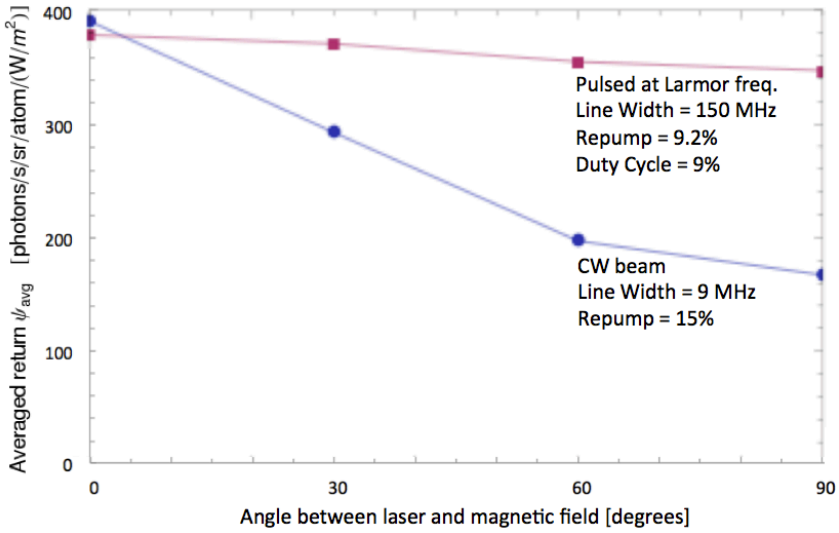

Figure 5.7: Graph by Paul Hillman suggests that pulsing at the Larmor frequency can result in 80% higher specific return than a CW laser with the same average power, when propagating perpendicular to Earth's magnetic field.

To understand the physical processes present in the Larmor frequency pulsing scenario, I created plots similar to Figure 3.6, but for propagation parallel and perpendicular to the magnetic field. The two graphs in Figure 5.8 show the time evolution of the return flux in the mesosphere for the 5 irradiance levels present in a 10 Watt, 20% duty cycle, 10% repumping format located at Mt. Hamilton. In the

perpendicular case (right), the emission from two of the irradiance levels (red and green) is seen to oscillate strongly at the Larmor frequency (~3 μs). Interestingly, the other levels do not show similar behavior. This suggests that certain levels of irradiance feel the effect of the magnetic field induced precession more strongly than others.

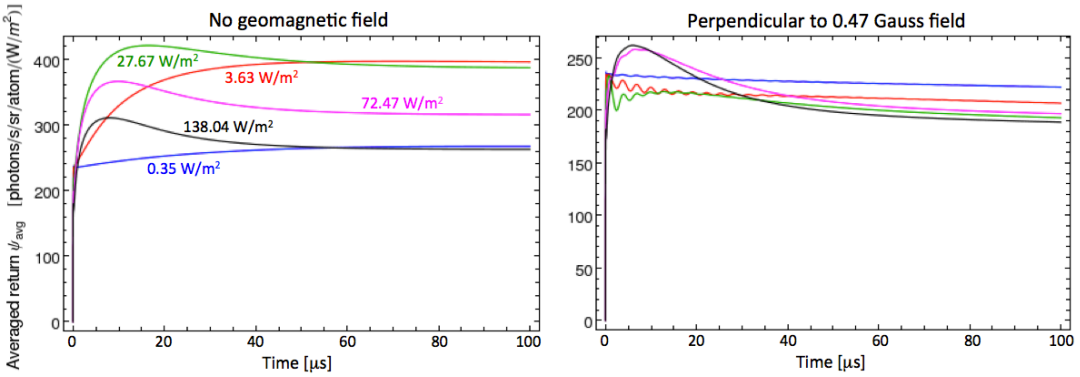

Figure 5.8: Evolution of return flux in the mesosphere as a function of time for the 5 irradiance levels present in a 10 Watt, 20% duty cycle, 10% repumping format at Mt. Hamilton. The left plot is for a laser propagation direction parallel to Earth's magnetic field lines, and the right graph shows the same for the perpendicular case. The strong effect of Larmor precession is evident in the right plot, especially for the median brightness levels.

The Larmor precession period is given by

$$\tau_L = \frac{h}{\mu_B |g_F| B} \tag{5.1}$$

where μ_B is the Bohr magneton and g_F is the Landé factor which depends on F ($g_F = \mp 1/2$ for the $F = 1, 2$ sodium ground states, respectively). The strength of the magnetic field at the altitude of the sodium layer is B, and h is Planck's constant. For Mt. Hamilton where $B = 0.47\ G, \tau_L \approx 3.1$ μs (326 kHz), and at Mauna Kea $B = 0.33\ G$ and $\tau_L \approx 4.4$ μs (231 kHz).

Figure 5.9 shows the evolution of pulses for a laser propagating perpendicular to the magnetic field with 10 W average power, 10% duty cycle, 10% repumping, and repetition rate equal to the Larmor frequency, at Mt. Hamilton. Again, it is apparent that the different irradiance levels behave differently, with the green line (≈31 W/m^2) being the most effective after a few cycles.

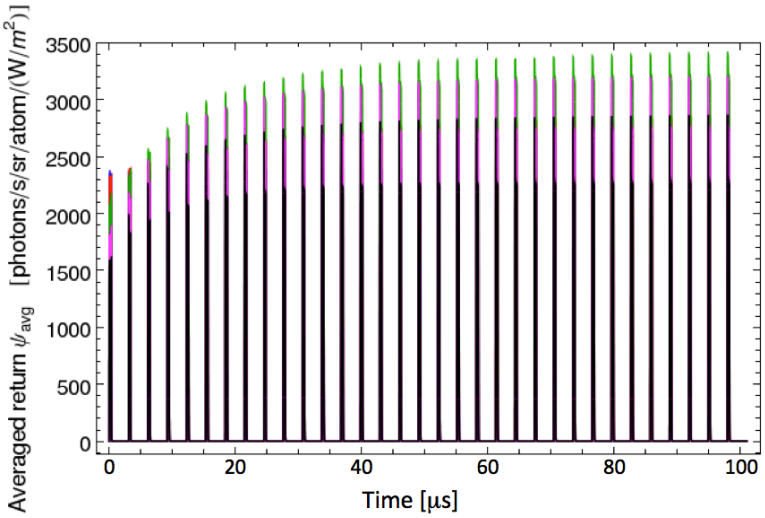

Figure 5.9: Return flux in the mesosphere as a function of time for a pulse format in which the repetition rate is equal to the Larmor frequency, for a 10 Watt LGS at Mt. Hamilton, with 10% duty cycle, circular polarized light, and 10% repumping, propagating perpendicular to the magnetic field. The different levels of irradiance are observed to evolve on different timescales, with steady state being approached during the ~100 μs simulation.

I ran similar simulations for a laser pulsed at the Larmor frequency with 20 W average power on Mauna Kea, but otherwise equivalent parameters. At both locations these were completed for the laser beam pointing parallel and perpendicular to the magnetic field, and to zenith. The return flux at the top of the telescope was calculated and compared to CW formats with the same average power, and also to the goal format in the case of Mt. Hamilton. The results are shown in Figure 5.10. The largest enhancement is seen for the case of propagation perpendicular to the magnetic

field at Mt. Hamilton, where the Larmor frequency pulses produce ~40% higher than a CW laser with the same average power. At Mauna Kea there is only a 7% increase over CW, likely because the strength of the geomagnetic field is less at this location.

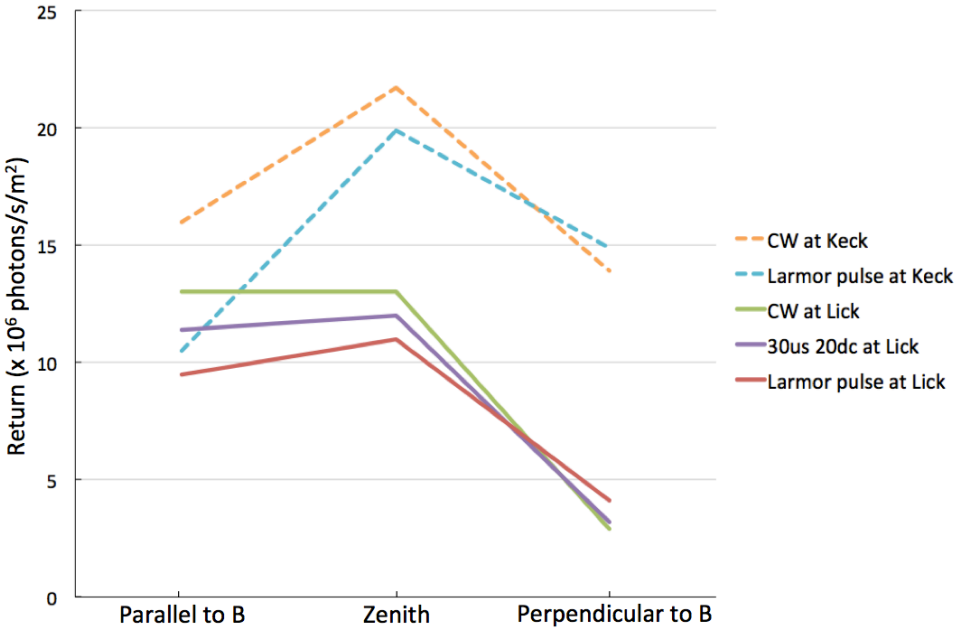

Figure 5.10: Comparison of return flux at the top of the telescope for: (1) the Larmor pulse format in Figure 5.5, (2) a CW format, and (3) the proposed goal format for the LLNL fiber laser at Mt. Hamilton. Simulations were carried out for the laser pointing parallel and perpendicular to the magnetic field, and to zenith, with 10 W average power at Mt. Hamilton and 20 W average power at Mauna Kea.

Figure 5.10 shows less enhancement then was expected based on the predictions of Figure 5.7, where the Larmor frequency pulse format produces ~80% higher than CW return when perpendicular to the magnetic field. However, Figure 5.7 is presenting the number of spontaneously emitted photons in the mesosphere (per second, per steradian, per atom, per W/m^2) for a magnetic field strength of 0.5 Gauss, and a single irradiance level of 47 W/m^2. The differences between Figures 5.7 and 5.10 are likely due to the inclusion in the latter of five irradiance levels, integrated

over a Gaussian beam profile in the mesosphere, and propagated back through the atmosphere to the telescope.

At Lick Observatory, the laser must be pointed 61° off zenith to point perpendicular to the geomagnetic field. The atmospheric attenuation of the light varies as T_a^{2X}/X, where T_a is the one-way atmospheric transmission at 589 nm at zenith, and $X = 1/\cos(\zeta)$ is the airmass with zenith angle ζ. Thus a large zenith angle will significantly reduce the number of returned photons from any format LGS. The Keck Observatory is much closer to the equator (Latitude 19.8°), and so the laser points perpendicular to the magnetic field at only 36.3° off zenith. But because the field strength is weaker here (0.33 Gauss, compared to 0.47 Gauss at Mt. Hamilton), the disruption due to Larmor precession is less than at the Lick Observatory, so there is reduced benefit from the pulsed format.

To ensure the repetition frequency used was indeed at the peak of the resonance, I simulated several slightly different rates. Figure 5.11 shows return flux from four repetition rates close to the Larmor frequency for Mt. Hamilton. This graph illustrates that the peak is narrow (only a few kilohertz wide), meaning experimental investigation of this phenomenon will require the ability to precisely tune the repetition rate of the laser.

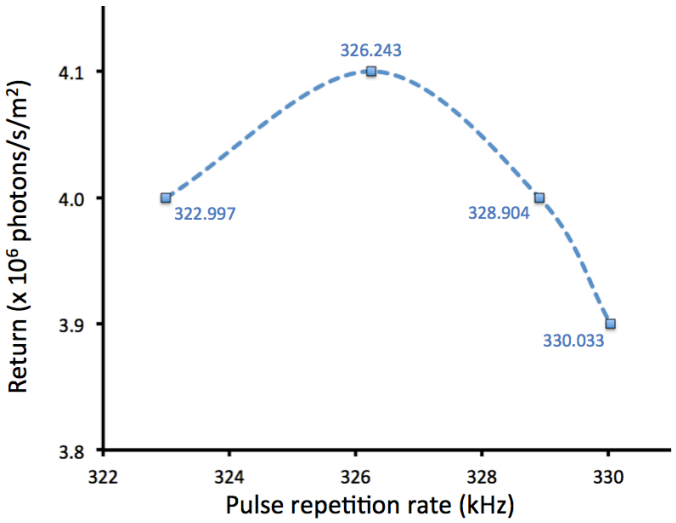

Figure 5.10: Simulations of the Larmor frequency pulsing scheme for slightly different repetition rates indicate the resonance peak is only a few kilohertz wide.

My investigation into this topic is only a preliminary analysis and should be validated by future study. It is an exciting possibility that pulsed system could have greater than CW return, because this could be used to significantly enhance the performance of LGS AO systems by allowing for background reduction tools such as Rayleigh blanking and fratricide avoidance strategies. In addition, it is also possible that inclusion of uplink correction could alter the irradiance distributions in such a way that pulsing at the Larmor frequency could indeed overcome limitations in the optical pumping efficiency of CW or other types of pulse formats.

5.5 Discussion

The methods presented in Chapter 2 for creating realistic atmospheric turbulence simulation devices provide the AO community an inexpensive means to verify the behavior and capabilities of both laboratory and on-sky systems. Upgrades to the spraying system are expected to improve the control of statistics and

replicability of the plate manufacture process. Additionally, a dedicated Shack-Hartmann WFS for measuring the plates could be used to reduce the time needed for characterization of their statistics.

Use of the ViLLaGEs instrument to compare the plates and sky in Section 2.6 showed that the sky data closely follows Kolmogorov theory one third of the time, while the characteristics of the plate remained fairly constant over time. It is possible that dome turbulence and/or the presence of the Jet Stream overhead could account for this divergence of the sky from the anticipated statistics. However, more studies of the statistical properties of real atmosphere should be carried out to quantify non-Kolmogorov behavior and its impact on AO system performance.

Recently, laser guide stars (LGS) have emerged as an important tool for advancing ground-based astronomy. The significant cost of these lasers necessitates maximizing efficiency, which is an effort that is still in progress. My work on this topic was motivated by the need to find the optimal format for a fiber laser built by Lawrence Livermore National Laboratory (LLNL). A goal format has been established, and the expected return compared between this, CW, and other formats.

This project yielded a deeper understanding of sodium-light interactions. It was observed that optical pumping is most effective in the first few microseconds of the laser light encountering the sodium atoms, after which time a variety of factors begin to diminish the return to the steady state value. It appears to take ~100 μs for the atoms to rethermalize once the laser is off and reproduce the initial enhancement phenomenon with the next light pulse. Also, certain irradiance levels couple to the

sodium more efficiently than others, as demonstrated in Figures 3.6, 3.7, 5.7 and 5.8. Furthermore, the optimal format for a LGS may depend on the location of the observatory on the surface of Earth, mainly due to the variations in the direction and strength of the geomagnetic field.

The benefits of uplink correcting the laser were considered in the final section of Chapter 3. Inclusion of such technology may have the capability to increase the overall performance of LGS AO systems. Some aspects of the impact of uplink technology have begun to be quantified, but more work is needed on this topic before conclusive statements can be made.

In Chapter 4, I presented comparisons between measurements of LGS brightness and the predictions of the LGSBloch model. For the short pulse lasers at the Lick, Keck, and Gemini South Observatories, the simulations over-estimate the data by a factor of 2 – 3. This discrepancy cannot be accounted for by modifying pulse shape and spectrum, using a more realistic irradiance profile, or assuming lower than expected power is reaching the mesosphere. LGSBloch also gives an under-prediction of return flux from the CW LGS at SOR when median sodium column density is assumed. Because of the high variability of the amount of mesospheric sodium, and other not well-defined factors, both discrepancies could signify inadequately understood physics and/or measurement parameters.

However, no inconsistency is seen when using simpler models of light-sodium interactions, such as what was developed by Milonni (Morris 1994, Milonni 1998, Neyman 2006). It may be that either the earlier and/or contemporary models

incorporate oversimplifications in some as-yet undetermined way, but the existence of this phenomenon certainly warrants future investigation.

There is also room for continued research in regard to the dynamics of the sodium layer. It has long been known that the sodium layer has variations that are seasonal, rather than annual, with a winter abundance maximum in both the northern and southern hemispheres. This winter maximum appears to be the effect of the seasonal temperature variation in the reactions that recycle sodium compounds back to free sodium (Plane et al. 1999). Perhaps due to the varying intensity of seasonal temperature changes, the strength of variability of sodium abundance is a function of latitude, with more extreme changes at larger latitudes (Gumbel et al. 2007, Roberts et al. 2007).

As the technology required for compensating atmospheric turbulence evolves, large ground based telescopes will become more capable of enabling groundbreaking scientific discoveries. History has already shown what a valuable endeavor it is to continually improve the capabilities of these systems. Every significant AO improvement has triggered new discoveries, from the structure of the rings of Uranus, to dynamical masses of the coolest brown dwarf stars, to direct imaging and spectroscopy of young extrasolar planets, to the size and nature of the environment around our Galaxy's central black hole, to the morphology and kinematics of high-redshift galaxies. Development of astronomical instrumentation is vital to achieving a more complete understanding of the incredible universe that contains us, and continued exploration of our ultimate beginnings.

References

Ammons, S. M., Johnson, L., Laag, E. A., Kupke, R., Gavel, D. T., Bauman, B. J., and Max, C. E., "Integrated Laboratory Demonstrations of Multi-Object Adaptive Optics on a Simulated 10-Meter Telescope at Visible Wavelengths", PASP, (2009).

Azucena, O., Crest, J., Cao, J., Sullivan, W., Kner, P., Gavel, D., Dillon, D., Olivier, S., and Kubby, J., "Wavefront aberration measurements and corrections through thick tissue using fluorescent microsphere reference beacons", Optics Express, Vol. 18, Issue 16, pp. 17521-17532 (2010).

Babcock, H. W., "The possibility of compensating astronomical seeing," Pub. Astr. Soc. Pac. 65, 229-236 (1953).

Baker, K. L., Stappaerts, E. A., Wilks, S. C., Young, P. E., Gavel, D., Tucker, J., Silva, D. A., and Olivier, S. S., "Open- and closed-loop aberration correction using a quadrature interfero- metric wave-front sensor," Opt. Lett. 29, 47–49 (2004).

Beckers J. M., "Adaptive optics for astronomy - Principles, performance, and applications," Annual review of astronomy and astrophysics. Vol. 31, p. 13-62 (1993).

Biswas, A., Wright, M., Sanii, B., and Page, N., "45 Km Optical Link Experiment," Proc. SPIE Free-Space Laser Communication Technologies XIII, Volume 4272, p. 60-71 (2001).

Boccas, M., Rigaut, F., Bec, M., Irarrazaval, B., James, E., Ebbers, A., d'Orgeville, C., Grace, K., Arriagada, G., Karewicz, S., Sheehan, M., White, J., and Chan, S., "Laser guide star upgrade of Altair at Gemini North," in Advances in Adaptive Optics II, eds Ellerbroek, B. L., Bonaccini Calia, D., Proc. SPIE, 6272, 62723L (2006).

Bonaccini Calia, D., Allaert, E., Alvarez, J. L., Araujo Hauck, C., Avila, G., Bendek, E., Buzzoni, B., Comin, M., Cullum, M., Davies, R., Dimmler, M., Guidolin, I., Hackenberg, W., Hippler, S., Kellner, S., van Kesteren, A., Koch, F., Neumann, U., Ott, T., Popovic, D., Pedichini, F., Quattri, M., Quentin, J., Rabien, S., Silber, A., and Tapia, M., "First light of the ESO Laser Guide Star Facility," in Advances in Adaptive Optics II, eds Ellerbroek, B., Bonaccini Calia, D., Proc. SPIE, 6272, 627207 (2006).

Bonaccini Calia, D., Holzlöhner, R., Guidolin, I., Pedichini, F., Centrone, M., Kasper, T., Lombardi, G., Forth, W., Lewis, S., Pfrommer, T., and Hackenberg, W., "ELT LGS-AO: Optimizing the LGS Return Flux," Proc. AO4ELT2 (2010).

Born, M., and Wolf, E., "Principles of Optics," Oxford: Pergamon Press, (1997).

Budker, D., and Romalis, M. V., "Optical Magnetometry," Nature Physics 3, 227 - 234 (2007).

Butler, D. J., Hippler, S., Egner, S., Xu, W., and Bähr, J., "Broadband, static wave-front generation: Na-Ag ion-exchange phase screens and telescope emulation," Appl. Opt. 43, 2813–2823 (2004).

Chin, J. C. Y., Wizinowich, P., Campbell, R., Chock, L., Cooper, A., James, E., Lyke, J., Mastromarino, J., Martin, O., Medeiros, D., Morrison, D., Neyman, C., Panteleev, S., Stalcup, T., Tucker, P., Wetherell, E., and van Dam, M., "Keck I Laser Guide Star Adaptive Optics System," Proc. of SPIE Vol. 8447 84474F, (2012).

Corney, A., in "Atomic and Laser Spectroscopy," Clarendon, Oxford, (2006).

Cox, A. N., in "Allen's Astrophysical Quantities," Springer New York, (2001).

Davis, C. C., Zhang, Y., Plett, M. L., Polak-Kingles, P., Barbier, P. R., and Rush, D. W., "Characterization of a liquid-filled turbulence simulator," Proc. SPIE 3432, 0227-786X (1998).

Dawson, J., Drobshoff, A., Beach, R., Messerly, M., Payne, S., Brown, A., Pennington, D., Bamford, D., Sharpe, S., and Cook, D., "Multi-watt 589nm fiber laser source," Proc. SPIE 6102 (2006).

de Pater, I., Wonga, M. H., Marcus, P., Luszcz-Cook, S., Ádámkovics, M., Conrad, A. , Asay-Davis, X., and Go, C., "Persistent rings in and around Jupiter's anticyclones – Observations and theory," Icarus, 210, 742 (2010).

Denman, C., Drummond, J., Eickhoff, M., Fugate, R., Hillman, P., Novotny, S., and Telle, J., "Characteristics of sodium guidestars created by the 50-watt FASOR and first closed-loop AO results at the Starfire Optical Range," Proc. SPIE 6272 (2006).

Drummond, J., Novotny, S., Denman, C., Hillman, P., and Telle, J., "The Sodium LGS Brightness Model over the SOR," AMOS 2007 Conference, pp. E67 (2007).

Eckart, A., Hippler, S., Glindemann, A., Hackenberg, W., Quirrenbach, A., Kalas, P., Kasper, M., Davies, R., Ott, T., Rabien, S., Butler, D., Holstenberg, H.-C., Looze, D., Rohloff, R.-R., Wagner, K., Wilnhammer, N., Hamilton, D., Beckwith, S., Appenzeller, I., and Genzel, R., "ALFA: The MPIA/MPE Laser Guide Star AO System," Experimental Astronomy, 10, 1 (2000).

Foy, R., and Labeyrie, A., “Feasibility of adaptive telescope with laser probe,” A&A 152, L29 (1985).

Fried, D. L., “Statistics of a Geometric Representation of Wavefront Distortion,” Opt. Soc. of Am. Journal 55 (11): 1427–1435 (1965).

Fugate, R.Q. in “Progress in Telescope and Instrumentation Technologies,” ESO Conference and Workshop Proceedings edited by Marie-Helene Ulrich (1992).

Gavel, D., and Friedman, H., “Measurements of the Lick Observatory sodium laser guide star,” Proc. SPIE 3353, 0277-786, (1998).

Genzel, R., Newman, S., Jones, T., F¨orster Schreiber, N. M., Shapiro, K., Genel, S., Lilly, S. J., Renzini, A., Tacconi, L. J., Bouch´e, N., Burkert, A., Cresci, G., Buschkamp, P., Carollo, C. M., Ceverino, D., Davies, R., Dekel, A., Eisenhauer, F., Hicks, E., Kurk, J., Lutz, D., Mancini, C., Naab, T., Peng, Y., Sternberg, A., Vergani, D., and Zamorani, G., “The SINS Survey of z ~ 2 Galaxy Kinematics: Properties of the Giant Star-Forming Clumps,” ApJ, 733, 101 (2011).

Ghez, A. M., Salim, S., Hornstein, S. D., Tanner, A., Lu, J. R., Morris, M., Becklin, E. E., and Duchene, G., “Stellar Orbits around the Galactic Center Black Hole,” ApJ 620 744 doi:10.1086/427175 (2005).

Ghez, A. M., Salim, S., Weinberg, N. N., Lu, J. R., Do, T., Dunn, J. K., Matthews, K., Morris, M. R., Yelda, S., Becklin, E. E., Kremenek, T., Milosavljevic, M., and Naiman, J., “Measuring Distance and Properties of the Milky Way's Central Supermassive Black Hole with Stellar Orbits,” ApJ, 689, 1044 (2008).

Goode P., Yurchyshyn, V., Cao, W., Abramenko, V., Andic, A., Ahn, K., and Chae, J., “Highest resolution observations of the quiescent Sun,” ApJ 714, L31 (2010).

Goodman, J., “Introduction to Fourier Optics,” Roberts and Company Publishers (2004).

Grigsby, B., Lockwood, C., Baumann, B., Gavel, D., Johnson, J., Ammons, S. M., Dillon, D., Morzinski, K., Reinig, M., Palmer, D., Serverson, S., and Gates, E., “ViLLaGEs: Opto-Mechanical Design of an on-sky visible-light MEMS-based AO system,” Proc. of SPIE Vol. 7018 701841-2 (2008).

Gumbel, J., Fan, Z. Y., Waldemarsson, T., Stegman, J., Witt, G., Llewellyn, E. J., She, C. –Y., and Plane, J. M. C., “Retrieval of global mesospheric sodium densities from the Odin satellite,” Geophysical Research Letters, Vol. 34, L04813 (2007).

Happer, W., MacDonald, G. J., Max, C. E., and Dyson, F. J., "Atmospheric-turbulence compensation by resonant optical backscattering from the sodium layer in the upper atmosphere," J. Opt. Soc. Am. A 11, 263–276 (1994).

Hardy, J. W., "Adaptive optics for astronomical telescopes," Oxford University Press. (1998).

Hayano, Y., Takami, H., Oya, S., Hattori, M., Saito, Y., Watanabe, M., Guyon, O., Minowa, Y., Egner, S. E., Ito, M., Garrel, V., Colley, S., Golota, T., and Iye, M., "Commissioning status of Subaru laser guide star adaptive optics system," Proc. SPIE, 7736, 77360N (2010).

Hillman et al. "Sodium guidestar return from broad CW sources," CfAO Laser Workshop (2006).

Hindmarsh, A. C., Brown, P. N., Grant, K. E., Lee, S. L., Serban, R., Shumaker, D. E., and Woodward, C. S., "SUNDIALS: Suite of nonlinear and differential/algebraic equation solvers," ACM Transactions on Mathematical Software 31, 363–396 (2005).

Hippler, S., Hormuth, F., Butler, D. J., Brandner, W., and Henning, T., "Atmosphere-like turbulence generation with surface-etched phase screens," Opt. Express 14, 10139–10148 (2006).

Holman, M. J., and Kepler Team, "Confirming and Constraining Kepler Planets via Transit Timing Variations," American Astronomical Society Meeting 220, 306.06 (2012).

Holzlöhner, R., Rochester, S. M., Calia, D. B., Budker, D., Pfrommer, T., and Higbie, J. M., "Simulations of pulsed sodium laser guide stars: an overview," Proc. SPIE 8774, Adaptive Optics Systems III, 84470H (2012).

Holzlöhner, R., Rochester, S. M., Calia, D. B., Budker, D., Higbie, J. M., and Hackenberg, W., "Optimization of cw sodium laser guide star efficiency," Astron. Astrophys. 510, A20+ (2010).

Holzlöhner, R., Rochester, S. M., Pfrommer, T., Calia, D. B., Budker, D., Higbie, J. M., and Hackenberg, W., "Laser guide star return flux simulations based on observed sodium density profiles," Proc. SPIE 7736, Adaptive Optics Systems II, 77360V (2010b).

Jeys, T. H., “Development of a mesospheric sodium laser beacon for atmospheric adaptive optics,” Lincoln Laboratory Journal 4, 133–150 (1991).

Johansson, E., and Gavel, D., “Simulation of stellar speckle imaging,” Proc. SPIE 2000, 372 (1994).

Keskin, O., Jolissaint, L., and Bradley, C., “Hot-air optical turbulence generator for the testing of adaptive optics systems: principles and characterization,” Appl. Opt. 45, 4888-4897 (2006).

Kolmogorov, A. N., “Dissipation of energy in locally isotropic turbulence,” Doklady Adak. Nauk SSSR 32, 16 (1941).

Kolmogorov, A. N., “The local structure of turbulence in incompressible viscous fluids at very large Reynolds numbers,” Dokl. Akad. Nauk. SSSR 30, 301–305 (1941).

Kupke, R., Gavel, D., Roskosi, C., Cabak, G., Cowley, D., Dillon, D., Gates, E. L., McGurk, R., Norton, A., Peck, M., Ratliff, C., and Reinig, M., "ShaneAO: an enhanced adaptive optics and IR imaging system for the Lick Observatory 3-meter telescope," Proc. SPIE 8447, Adaptive Optics Systems III, 84473G (September 13, 2012).

Lagrange, A.-M., Bonnefoy, M., Chauvin, G., Apai, D., Ehrenreich, D., Boccaletti, A., Gratadour, D., Rouan, D., Mouillet, D., Lacour, S., and Kasper, M., “A Giant Planet Imaged in the Disk of the Young Star ß Pictoris,” Science, 329, 57 (2010).

Le Mignant, D., Campbell, R., Boucheza, A., Chin, J., Chock, E., Conrad, A., van Dam, M., Doyle, S., Goodrich, R., Johansson, E., Lafon, R., Lyke, J., Melcher, C., Mouser, R., Summers, D., Wilburn, C., and Wizinowich, P., “LGS AO operations at the W. M. Keck Observatory,” Proc. SPIE 6270 (2006).

Macintosh, B., Graham, J., Palmer, D., Doyon, R., Gavel, D., Larkin, J., Oppenheimer, B., Saddlemyer, L., Wallace, K., Bauman, B., Evans, J., Erikson, D., Morzinski, K., Phillion, D., Poyneer, L., Sivaramakrishnan, A., Soummer, R., Thibault, S., and Veran, J., “The Gemini Planet Imager,” Proc. SPIE 6272, 18 (2006).

Marchis, F., Kaasalainen, M., Hom, E. F., Berthier, J., Enriquez, J., Hestroffer, D., Le Mignant, D., and de Pater, I., “Shape, size and multiplicity of main-belt asteroids I. Keck Adaptive Optics survey,” Icarus, 185, 39 (2006).

Marois, C., Macintosh, B., Barman, T., Zuckerman, B., Song, I., Patience, J., Lafreniere, D., and Doyon, R., "Direct Imaging of Multiple Planets Orbiting the Star HR 8799," Science, 322, 1348 (2008).

Max, C. E., "Lecture 5: The optical effects of atmospheric turbulence," Astronomy 289. University of California, Santa Cruz (2010).

Max, C. E., Olivier, S. S., Friedman, H. W., An, J., Avicola, K., Beeman, B. V., Bissinger, H. D., Brase, J. M., Erbert, G. V., Gavel, D. T., Kanz, K., Liu, M. C., Macintosh, B., Neeb, K. P., Patience, J., and Waltjen, K.E., "Image Improvement from a Sodium-Layer Laser Guide Star Adaptive Optics System," Science, 277, 1649 (1997).

Melbourne, J., Peng, C. Y., Soifer, B. T., Urrutia, T., Desai, V., Armus, L., Bussmann, R. S., Dey, A., and Matthews, K., "The Black Hole Masses and Star Formation Rates of z>1 Dust Obscured Galaxies: Results from Keck OSIRIS Integral Field Spectroscopy," The Astronomical Journal 141 (2011).

Milonni, P. W., Fugate, R. Q., and Telle, J. M., "Analysis of measured photon returns from sodium beacons," J. Opt. Soc. Am. A 15, 217–233 (1998).

Morris, J. R., "Efficient excitation of a mesospheric sodium laser guide star by intermediate-duration pulses," JOSA A, Vol. 11, Issue 2, pp. 832-845 (1994).

Morzinski, K., Johnson, L. C., Gavel, D. T., Grigsby, B., Dillon, D., Reinig, M., and Macintosh, B. A., "Performance of MEMS-based visible-light adaptive optics at Lick Observatory: Closed- and open-loop control," Proc. SPIE 7736, 77361O (2010).

Moussaoui, N., Clemesha, B.R., Holzlöhner, R., Simonich, D. M., Calia, D. B., Hackenberg, W., and Batista, P. P., "Statistics of the sodium layer parameters and its impact on AO sodium LGS characteristics," Astron. Astrophys. 511, A31 (2010).

Neichel, B., D'Orgeville, C., Callingham, J., Rigaut, F., Winge, C., and Trancho, G., "Characterization of the sodium layer at Cerro Pachón, and impact on laser guide star performance," Mon. Not. R. Astron. Soc. 000, 1–11 (2013).

Neyman, C. R., "Estimating the Atmospheric Sodium Density from Keck Laser Guide Star Photometry," Keck Adaptive Optics Note 416 (2006).

Noll, R. J., "Zernike polynomials and atmospheric turbulence," J. Opt. Soc. Am. 66, pp. 207-211 (1976).

Nowak N., Thomas, J., Erwin, P., Saglia, R. P., Bender, R., and Davies, R. I., "Do

black hole masses scale with classical bulge luminosities only? The case of the two composite pseudo-bulge galaxies NGC 3368 and NGC 3489," MNRAS, 403, pp. 646-672 (2010).

Phillips, J. D., Goda, M. E., and Schmidt, J., "Atmospheric turbulence simulation using liquid-crystal spatial light modulators," Proc. SPIE 5894, 589406-1–589406-11 (2005).

Plane, J. M. C., Gardner, C. S., Yu, J. R., She, C. Y., Garcia, R. R., and Pumphrey, H. C., "Mesospheric Na layer at 40°N: Modeling and observations," J. Geophys. Res., 104, 3773 (1999).

Porter, J., Queener, H., Lin, L., Karen, T., and Awwal, A., "Adaptive Optics for Vision Science," John Wiley & Sons, Inc. (2006).

Rampy, R., Gavel, D., Rochester, S. M., and Holzlöhner, R., "Investigations of long pulse sodium laser guide stars," Proc. SPIE 8447, Adaptive Optics Systems III, 84474L (2012).

Rhoadarmer, T. A., and Angel, R. P., "Low-cost, broadband static phase plate for generating atmospheric-like turbulence," Appl. Opt. 40, 2946-1955 (2001).

Roberts, L. C., Jr., Bradford, L. W., Neyman, C. R., and Liu, A. Z., "Measurements of Mesospheric Sodium Abundance above the Hawaiian Islands," Publications of the Astronomical Society of the Pacific, Vol. 119, No. 857, pp. 787-792 (2007).

Rochester, S. M., Otarola, A., Boyer, C., Budker, D., Ellerbroek, B., Holzlöhner, R., and Wang, L., "Modeling of pulsed-laser guide stars for the Thirty Meter Telescope project," JOSA B, Vol. 29, Issue 8, pp. 2176-2188 (2012).

Sawruk, N. W., Lee, I., Jalali, M. P., Prezkuta, Z., Groff, K. W., Roush, J., Rogers, N., Tiemann, B., Hannon, S. M., Alford, W. J., d'Orgeville, C., Fesquet, V., Oram, R., Adkins, S. M., and Grace, K., "System overview of 30 W and 60 W 589 nm guidestar laser systems," SPIE Proc. 7736, 77361Y-77361Y-8. (2010).

Taylor, G. I., "The spectrum of turbulence," Proc Roy Soc Lond 164:476–490 (1938).

Thomas, S., "A simple turbulence simulator for adaptive optics," Proc. SPIE 5490, 0277-786X (2004).

Weinberg, N. N., Milosavljevic, M., and Ghez, A. M., "Stellar Dynamics at the Galactic Center with an Extremely Large Telescope," The Astrophysical Journal 622, 878 (2005).

Wilson, K. E., Kovalik, J., Biswas, A., and Roberts, W., "Development of laser beam transmission strategies for future ground-to-space optical communications," Proceedings of the SPIE, Volume 6551, pp. 65510B (2007).

Wizinowich, P. L., Le Mignant, D., Bouchez, A. H., Campbell, R. D., Chin, J. C. Y., Contos, A. R., van Dam, M. A., Hartman, S. K., Johansson, E. M., Lafon, R. E., Lewis, H., Stomski, P. J., and Summers, D. M., "The W. M. Keck Observatory Laser Guide Star Adaptive Optics System: Overview," PASP, 118, 297-309 (2006).

Xiong, H., Gardner, C.S., and Liu, A.Z., "Seasonal and nocturnal variations of the mesospheric sodium layer at Starfire Optical Range, New Mexico", Chin. J. of Geophys. 46, pp. 432–437 (2003).

Zhang, Y., Cense, B., Rha, J., Jonnal, R. S., Gao, W., Zawadzki, R. J., Werner, J. S., Jones, S., Olivier, S., and Miller, D. T., "High-speed volumetric imaging of cone photoreceptors with adaptive optics spectral-domain optical coherence tomography," Optics Express, Vol. 14, Issue 10, pp. 4380-4394 (2006).